

**AVSCOM TR-87-C-35
ME-TSPC-TR-87-13
December 1987**

**The Effect of Prewirl on the
Internal Aerodynamics and
Performance of a Mixed Flow
Research Centrifugal Compressor**

William B. Bryan and Sanford Fleeter

**Prepared For
U.S. ARMY AVIATION
SYSTEMS COMMAND**

**NATIONAL AERONAUTICS AND SPACE
ADMINISTRATION
NASA LEWIS RESEARCH CENTER
Grant NSG-3285**

**Thermal Sciences and Propulsion Center
School of Mechanical Engineering
Purdue University
West Lafayette, Indiana 47907**

N89-15503

Unclass
0188548

G3/34

(NASA-CR-184756) THE EFFECT OF PREWHIRL ON
THE INTERNAL AERODYNAMICS AND PERFORMANCE OF
A MIXED FLOW RESEARCH CENTRIFUGAL COMPRESSOR
(Purdue Univ.) 159 P
CSCL 20D

AVSCOM TR-87-C-35
ME-TSPC-TR-87-13

**THE EFFECT OF PREWHIRL ON THE
INTERNAL AERODYNAMICS AND PERFORMANCE OF
A MIXED FLOW RESEARCH CENTRIFUGAL COMPRESSOR**

William B. Bryan and Sanford Fleeter

December 1987

**Thermal Sciences and Propulsion Center
School of Mechanical Engineering
Purdue University
West Lafayette, Indiana 47907**

Prepared For

**U.S. ARMY AVIATION SYSTEMS COMMAND
NATIONAL AERONAUTICS AND SPACE ADMINISTRATION
NASA LEWIS RESEARCH CENTER
GRANT NSG - 3285**

ABSTRACT

The Purdue Research Centrifugal Compressor Facility is a low speed, large scale machine designed to facilitate the investigation of flow properties in the inlet, impeller and diffuser. The facility is extensively instrumented with pressure taps and probes throughout the flow channels which enable static pressure distribution measurements to be made on the rotating impeller blades, the diffuser vanes, and all of the flow channels. Pressures are measured with transducers and rotating scanners interfaced through a computer based data acquisition system.

Compressor performance was investigated at various inlet guide vane angles from -15° to 45° . Varying the inlet guide vane angle had a significant effect on compressor performance. Increasing the inlet guide vane angle increased the maximum facility pressure rise up to an angle of 30° . The flow rate at which this maximum pressure rise occurred also increased with increasing inlet guide vane angle. The efficiency versus inlet guide vane behavior was similar to that of the pressure rise. The maximum efficiency occurred at a flow rate equal to or greater than that of the maximum pressure rise and the maximum efficiency decreased with increasing inlet guide vane angle.

The static pressure distributions on the impeller blades were similar for all inlet guide vane settings at flow rates near stalling. As the flow rate was increased, low inlet guide vane settings caused decreased incidence angles on the impeller blades leading to pressure surface stalling at high flow rates. Most of the change in

pressure distribution occurred at the blade tips for low inlet guide vane angles. For larger inlet guide vane angles, positive incidence on the blades and large accelerations around the blade leading edges occurred at higher flow rates. The changes in pressure distribution tended to occur more evenly over the blade surface than at low inlet guide vane angles. Varying the inlet guide vane angle had little impact on the diffuser pressure and velocity distributions since the relative flow angle leaving the impeller was determined primarily by the flow rate.

TABLE OF CONTENTS

LIST OF TABLES	iii
LIST OF FIGURES	v
LIST OF SYMBOLS	xii
CHAPTER 1 - INTRODUCTION	1
CHAPTER 2 - THE PURDUE RESEARCH CENTRIFUGAL COMPRESSOR	6
Impeller and Drive Assembly	11
Inlet	17
Diffuser	25
Plenum	32
Exhaust Piping	32
Summary	37
CHAPTER 3 - RESEARCH CENTRIFUGAL COMPRESSOR	
INSTRUMENTATION	39
Stationary Pressure Measurement	39
Rotating Pressure Measurement System	42
Temperature Measurement	46

Computer Data Acquisition System	46
CHAPTER 4 - DATA ACQUISITION AND ANALYSIS	49
Stationary Pressure Measurement	49
Rotating Pressure Measurement	52
Temperature Measurement	55
Compressor Performance	55
Pressures and Velocities	57
CHAPTER 5 - RESULTS	59
Overall Compressor Performance	59
Impeller Static Pressure Distribution	72
Diffuser Flow Field	99
CHAPTER 6 - SUMMARY AND CONCLUSIONS	117
LIST OF REFERENCES	120
APPENDICES	
Appendix A	122
Appendix B	132

LIST OF TABLES

5.1 Research Compressor Facility Parameters	60
5.2 Inlet Swirl Angle Versus Inlet Guide Vane Angle.....	69

Appendix

Table

A1. Impeller Coordinates	123
A2. Inlet Channel Wall Coordinates	124
A3. Diffuser Channel Wall Coordinates.....	125
A4. Coordinates for NACA 0015 Airfoil Section	126
A5. Coordinates for NACA 4312 Airfoil Section	126
A6. Inlet Hub Streamline Pressure Tap Coordinates	127
A7. Inlet Tip Streamline Pressure Tap Coordinates	127
A8. Diffuser Hub Streamline Pressure Tap Coordinates	128
A9. Diffuser Tip Streamline Pressure Tap Coordinates.....	129

A10. Impeller Pressure Tap Coordinates.....	130
A11. Diffuser Vane Pressure Tap Coordinates	131
B1. Impeller Inlet Incidence Angles ($\alpha_{igv} = -15^\circ$).....	134
B2. Impeller Inlet Incidence Angles ($\alpha_{igv} = 0^\circ$)	135
B3. Impeller Inlet Incidence Angles ($\alpha_{igv} = 15^\circ$).....	135
B4. Impeller Inlet Incidence Angles ($\alpha_{igv} = 30^\circ$).....	136
B5. Impeller Inlet Incidence Angles ($\alpha_{igv} = 45^\circ$).....	136
B6. Diffuser Incidence Angles ($\alpha_{igv} = -15^\circ$)	137
B7. Diffuser Incidence Angles ($\alpha_{igv} = 0^\circ$).....	137
B8. Diffuser Incidence Angles ($\alpha_{igv} = 15^\circ$).....	138
B9. Diffuser Incidence Angles ($\alpha_{igv} = 30^\circ$).....	138
B10. Diffuser Incidence Angles ($\alpha_{igv} = 45^\circ$).....	139

LIST OF FIGURES

1.1 Flow Phenomena in a Centrifugal Compressor	3
2.1 Front View of Compressor Test Facility	7
2.2 Rear View of Compressor Test Facility	8
2.3 Cutaway of Compressor Test Facility	9
2.4 Inlet, Impeller, and Diffuser Flow Channel.....	10
2.5 Impeller and Drive Assembly	12
2.6 Side View of Impeller	14
2.7 Front View of Impeller.....	15
2.8 Impeller Pressure Tap Locations	16
2.9 View of Inner Side of Inlet.....	18
2.10 Inlet Guide Vane Profile	19
2.11 Pressure Taps on Inlet Hub Streamline	20
2.12 Pressure Taps on Inlet Tip Streamline	21

2.13 Pressure Probe Locations	22
2.14 Pressure Probes	23
2.15 Probe Mounted in Holder	24
2.16 Rear of Diffuser Section	26
2.17 Front of Diffuser Section	27
2.18 Diffuser Guide Vane Profile	28
2.19 Pressure Taps on Diffuser Hub Streamline	29
2.20 Pressure Taps on Diffuser Tip Streamline	30
2.21 Diffuser Vane Static Pressure Taps	31
2.22 Facility Under Construction Showing Plenum	33
2.23 Overhead Schematic of Test Facility	34
2.24 Exhaust Piping	35
2.25 Exhaust Piping Showing Orifice Location and Pressure Taps	36
2.26 Computer Controlled Throttle Plate	38
3.1 Reference Pressure System and Manometer	41

3.2 Scanivalve Valve Switching Assembly	43
3.3 Rotating Scanivalve (36TR).....	44
3.4 Assembled Rotating Pressure Measurement System.....	47
4.1 Rotating Fluid Element Kinetic Diagram.....	53
5.1 Pressure Rise Coefficient Versus Flow Coefficient	61
5.2 Pressure Ratio Versus Corrected Mass Flow	62
5.3 Efficiency Versus Flow Coefficient	63
5.4 Power Coefficient Versus Flow Coefficient.....	64
5.5 Impeller Velocity Relations.....	66
5.6 Impeller Blade Static Pressure Distribution (IGV Angle = -15° , $\phi = 0.132$).....	73
5.7 Impeller Blade Static Pressure Distribution (IGV Angle = 0° , $\phi = 0.122$).....	74
5.8 Impeller Blade Static Pressure Distribution (IGV Angle = 15° , $\phi = 0.125$).....	75

5.9 Impeller Blade Static Pressure Distribution	
(IGV Angle = 30° , $\phi = 0.127$).....	76
5.10 Impeller Blade Static Pressure Distribution	
(IGV Angle = 45° , $\phi = 0.126$).....	77
5.11 Impeller Blade Static Pressure Distribution	
(IGV Angle = -15° , $\phi = 0.204$).....	78
5.12 Impeller Blade Static Pressure Distribution	
(IGV Angle = 0° , $\phi = 0.193$)	79
5.13 Impeller Blade Static Pressure Distribution	
(IGV Angle = 15° , $\phi = 0.197$).....	80
5.14 Impeller Blade Static Pressure Distribution	
(IGV Angle = 30° , $\phi = 0.196$).....	81
5.15 Impeller Blade Static Pressure Distribution	
(IGV Angle = 45° , $\phi = 0.197$).....	82
5.16 Impeller Blade Static Pressure Distribution	
(IGV Angle = -15° , $\phi = 0.258$).....	83
5.17 Impeller Blade Static Pressure Distribution	
(IGV Angle = 0° , $\phi = 0.261$)	84

5.18 Impeller Blade Static Pressure Distribution	
(IGV Angle = 15° , $\phi = 0.270$).....	85
5.19 Impeller Blade Static Pressure Distribution	
(IGV Angle = 30° , $\phi = 0.263$).....	86
5.20 Impeller Blade Static Pressure Distribution	
(IGV Angle = 45° , $\phi = 0.266$).....	87
5.21 Impeller Blade Static Pressure Distribution	
(IGV Angle = -15° , $\phi = 0.313$).....	88
5.22 Impeller Blade Static Pressure Distribution	
(IGV Angle = 0° , $\phi = 0.313$)	89
5.23 Impeller Blade Static Pressure Distribution	
(IGV Angle = 15° , $\phi = 0.325$).....	90
5.24 Impeller Blade Static Pressure Distribution	
(IGV Angle = 30° , $\phi = 0.318$).....	91
5.25 Impeller Blade Static Pressure Distribution	
(IGV Angle = 45° , $\phi = 0.325$).....	92
5.26 Diffuser Vane Static Pressure Distribution	
(IGV Angle = -15° , $\phi = 0.310$).....	100

5.27 Diffuser Vane Static Pressure Distribution

(IGV Angle = 0° , $\phi = 0.319$)101

5.28 Diffuser Vane Static Pressure Distribution

(IGV Angle = 15° , $\phi = 0.324$).....102

5.29 Diffuser Vane Static Pressure Distribution

(IGV Angle = 30° , $\phi = 0.327$).....103

5.30 Diffuser Vane Static Pressure Distribution

(IGV Angle = 45° , $\phi = 0.327$).....104

5.31 Diffuser Vane Static Pressure Distribution

(IGV Angle = 0° , $\phi = 0.285$)106

5.32 Diffuser Vane Static Pressure Distribution

(IGV Angle = 0° , $\phi = 0.251$)107

5.33 Diffuser Exit Velocity Profile

(IGV Angle = -15° , $\phi = 0.315$).....109

5.34 Diffuser Exit Velocity Profile

(IGV Angle = 0° , $\phi = 0.318$)110

5.35 Diffuser Exit Velocity Profile

(IGV Angle = 15° , $\phi = 0.319$).....111

5.36 Diffuser Exit Velocity Profile

(IGV Angle = 30° , $\phi = 0.313$).....112

5.37 Diffuser Exit Velocity Profile

(IGV Angle = 45° , $\phi = 0.320$).....113

5.38 Diffuser Exit Velocity Profile

(IGV Angle = 0° , $\phi = 0.282$)114

5.39 Diffuser Exit Velocity Profile

(IGV Angle = 0° , $\phi = 0.245$)115

LIST OF SYMBOLS

<i>Symbol</i>	<i>Description</i>
A	Area
c	Absolute Velocity
c_p	Constant Pressure Specific Heat
C_p	Pressure Coefficient
d	Diameter
e	Uncertainty
f	Function
m	Mass
\dot{m}	Mass Flow Rate
n	Number of Samples
P	Pressure
P_0	Total Pressure
ϕ	Power Coefficient
r	Radius
R	Gas Constant, Air

s	Standard Deviation
t	Student's t-Factor
T	Temperature
T₀	Total Temperature
U	Wheel Speed
v	Voltage
V	Velocity
w	Relative Velocity
α	Absolute Flow Angle
β	Relative Flow Angle
γ	Specific Heat Ratio
Δ	Difference
η	Efficiency
θ	Angle
μ	True Mean
ξ	Yawmeter Sensitivity
ρ	Density
σ	Slip Factor

ϕ	Flow Coefficient
Ψ	Pressure Rise Coefficient
ω	Angular Velocity

Subscripts

1	Impeller Inlet
2	Impeller Exit
amb	Ambient Condition
axis	Impeller Axis
cal	Calibration
igv	Inlet Guide Vane
L	Left
P	Pressure
r	radial
ref	Reference
R	Right
tap	Impeller Tap
x	Axial

θ

Tangential

Superscripts

—

Average

'

Value Based on Blade Angle

→

Vector Valued

CHAPTER 1 - INTRODUCTION

Centrifugal compressors are an integral part of small gas turbine engines utilized for both industrial and aircraft applications. Applications include pumping sets, peak load electricity generation, helicopters, turboprops and business jets, ship power and electricity generation, and in the future, power for trucks and perhaps automobiles. Centrifugal compressors are also a major component in refrigeration and air conditioning units, in automotive and truck internal combustion and diesel engine turbochargers, and in highly supercharged turbo-compound diesels. Thus it can be seen that the centrifugal compressor is the key to important technical advances, many of which have significant defense and ecological impact. To achieve these advances, it is necessary to significantly improve the performance of the centrifugal compressor [1,2].

A centrifugal compressor is a rotating device which increases the stagnation enthalpy of a fluid through the action of its rotating blades, with the flow mainly in a plane that is perpendicular to the axis of rotation. In contrast, the flow through an axial compressor has almost no radial velocity component. The main purpose of a centrifugal compressor is to increase the pressure of the working fluid. This pressure rise is the result of two separate effects. The first is due to the fluid flowing along a radial path in a rotating channel, with a centrifugal pressure rise imparted to the fluid as it increases in radius. The second is due to the decrease in velocity in the diffusing section of the compressor.

The actual flow through a centrifugal compressor is highly complex, as depicted schematically in Figure 1.1. Highly three-dimensional flow fields exist in the

passages of the impeller due to secondary flows, separated regions and boundary layers. In addition, the flow varies with time due to the interaction of the impeller blades and diffuser vanes. Because of these complex and interacting flow phenomena, detailed analyses and experiments are necessary to quantify the phenomena occurring and to gain a better understanding of the flow through centrifugal compressors.

Typically, centrifugal compressor studies have focused on overall flow phenomena. For example, Qinghuan [3] considered the design of a prototype centrifugal compressor for marine turbocharger applications. The prototype had a design speed of 25000 rpm. Flow phenomena such as choking, surge, impeller diffuser matching, and the locations of highest efficiency were discussed.

Inoue and Cumpsty [4] investigated the interaction between a centrifugal impeller and a vaned diffuser. Their investigation used an impeller with a design speed of 31,500 rpm rotating at 3000 rpm. Three diffusers were used with 10, 20 and 30 vanes set at radius ratios of 1.04, 1.1 and 1.2. It was noted that the distorted flow from the impeller was attenuated very rapidly in the diffuser entrance but the effect of the diffuser vanes on the impeller was evident, with reversal of the flow back into the impeller at low flow rates and radius ratios.

Two studies have focused on the effects of varying the inlet and diffuser flow fields to improve centrifugal compressor performance. Simon, Wallmann, and Monk [5] investigated the effects of simultaneous adjustment of inlet guide vanes and diffuser vanes of single-stage and multistage centrifugal compressors. They found that the efficiency over the entire operating range could be increased by

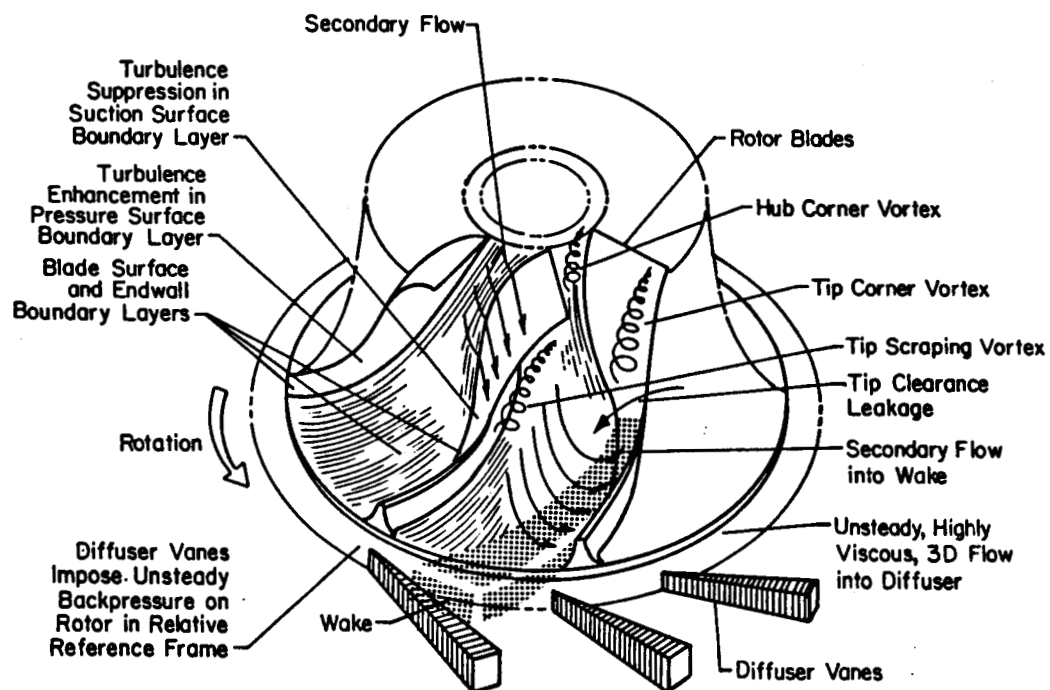


Figure 1.1 Flow Phenomena in a Centrifugal Compressor

optimum adjustment of the inlet guide vanes and diffuser vanes.

Kyrtatos and Watson [6] studied the effect of aerodynamically induced prewhirl on a small turbocharger compressor. An arrangement of air jets at the inlet of the compressor was used to impart prewhirl. The effect of aerodynamically induced prewhirl was found to be similar to that produced by inlet guide vanes.

Among the most basic and challenging of the physical phenomena inherent to the centrifugal compressor are those relating to the internal three-dimensional steady and time-varying flow through the diffusing elements, including the rotating blade passages. In this regard, NASA-Lewis has embarked on a research program focused on obtaining benchmark experimental data for application to centrifugal compressors. Wood, Adam, and Buggele [7] considered the design of the NASA large scale, low speed, centrifugal compressor facility to be used for internal flow code verification and modeling. This facility will have a maximum speed of 2400 rpm and be equipped with an altitude exhaust system. The impeller and diffuser will be extensively equipped with static and dynamic pressure instrumentation. An LDV system will also be used to measure velocities in the rotating impeller.

In support of the overall NASA research program on centrifugal compressors, the Department of the Navy has made an indefinite loan to Purdue University of a moderate scale, subsonic, mixed flow research centrifugal compressor facility [8]. The outstanding feature of this facility is its relatively large size and the ability to extensively instrument the flow path, including the impeller and the exit vaned radial diffuser. This relatively large scale assures the accuracy of the experimental measurements by minimizing instrumentation interference effects, and enables

reasonable Reynolds numbers to be achieved at moderate air velocities and rotational speeds. Thus, internal flow conditions, both steady and time-variant, can be measured in considerable detail throughout the entire research compressor and radial diffuser for various operating conditions. This not only provides a means of studying the detailed nature of the internal flow under different practical operating conditions, but also provides for assessment of predictions obtained from mathematical models.

CHAPTER 2 - THE PURDUE RESEARCH CENTRIFUGAL COMPRESSOR

The Purdue Research Centrifugal Compressor Facility is shown in Figures 2.1 and 2.2. The general operation of the machine can be described by considering the flow path, shown in Figures 2.3 and 2.4. The compressor is driven by a jack shaft and pulley arrangement. The current rotational speed is 1790 rpm with a 1:1 pulley ratio. However, a speed of 2400 rpm can be achieved by changing pulleys.

Air is drawn radially into the machine uniformly along the circumference of the inlet section. The inlet passage curves smoothly such that the air is gradually turned from a radial direction to a direction parallel to the axis of the machine. A set of annular guide vanes control the flow direction into the impeller. Nominally, these guide vanes are radially oriented. Prewhirl in either direction can be imparted to the impeller inlet flow field by adjusting the angular position of these inlet guide vanes.

The flow then enters the mixed flow impeller which changes the axial inlet flow to a nearly radial flow at the outlet and also imparts a peripheral component of velocity to the air. The center of the rotor is hollow, permitting the installation of instrumentation to transmit pressure data from the surfaces of the rotating blades to the data acquisition and analysis system located outside of the machine in the stationary frame of reference.

On leaving the impeller, the air passes outward through an annular passage whose walls are smoothly curved such that the air is gradually redirected into a

ORIGINAL PAGE IS
OF POOR QUALITY

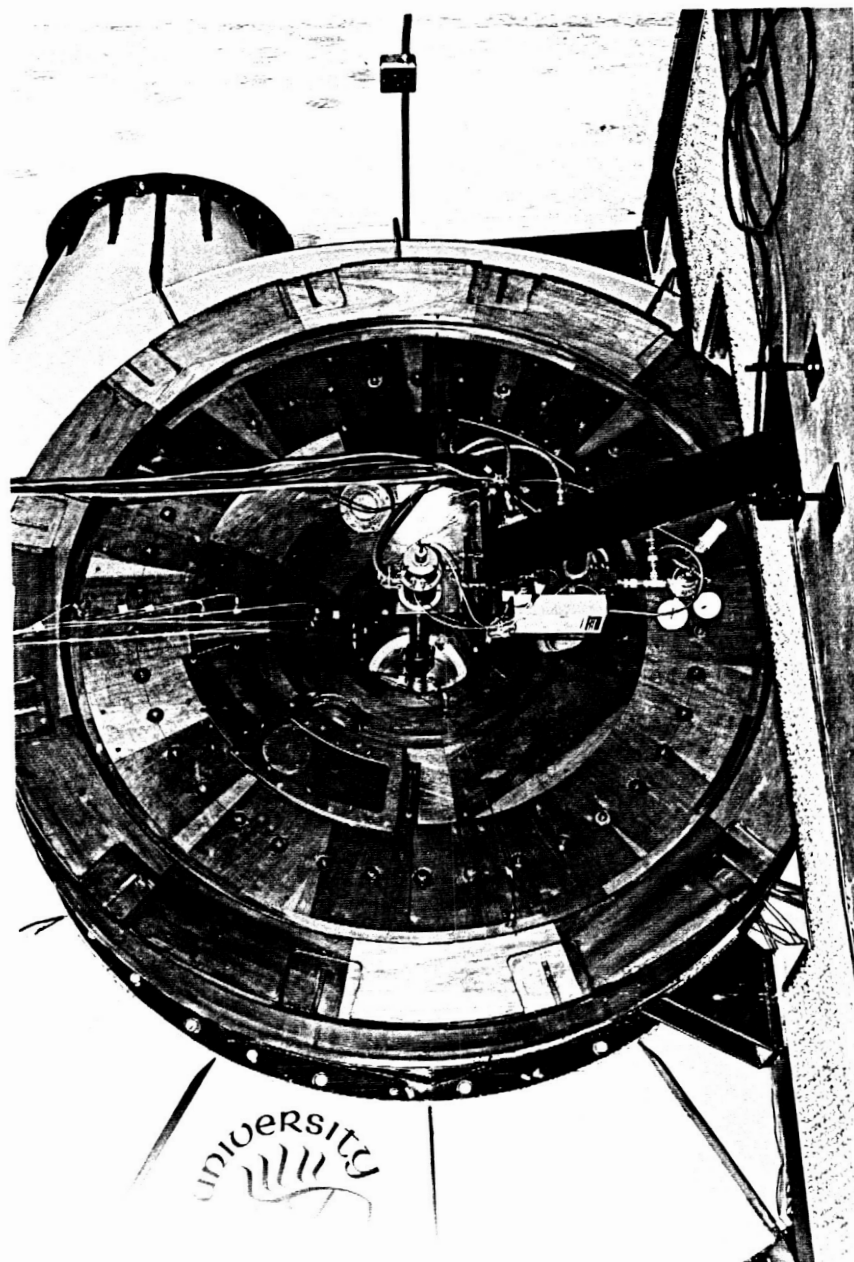


Figure 2.1 Front View of Compressor Test Facility

ORIGINAL PAGE IS
OF POOR QUALITY

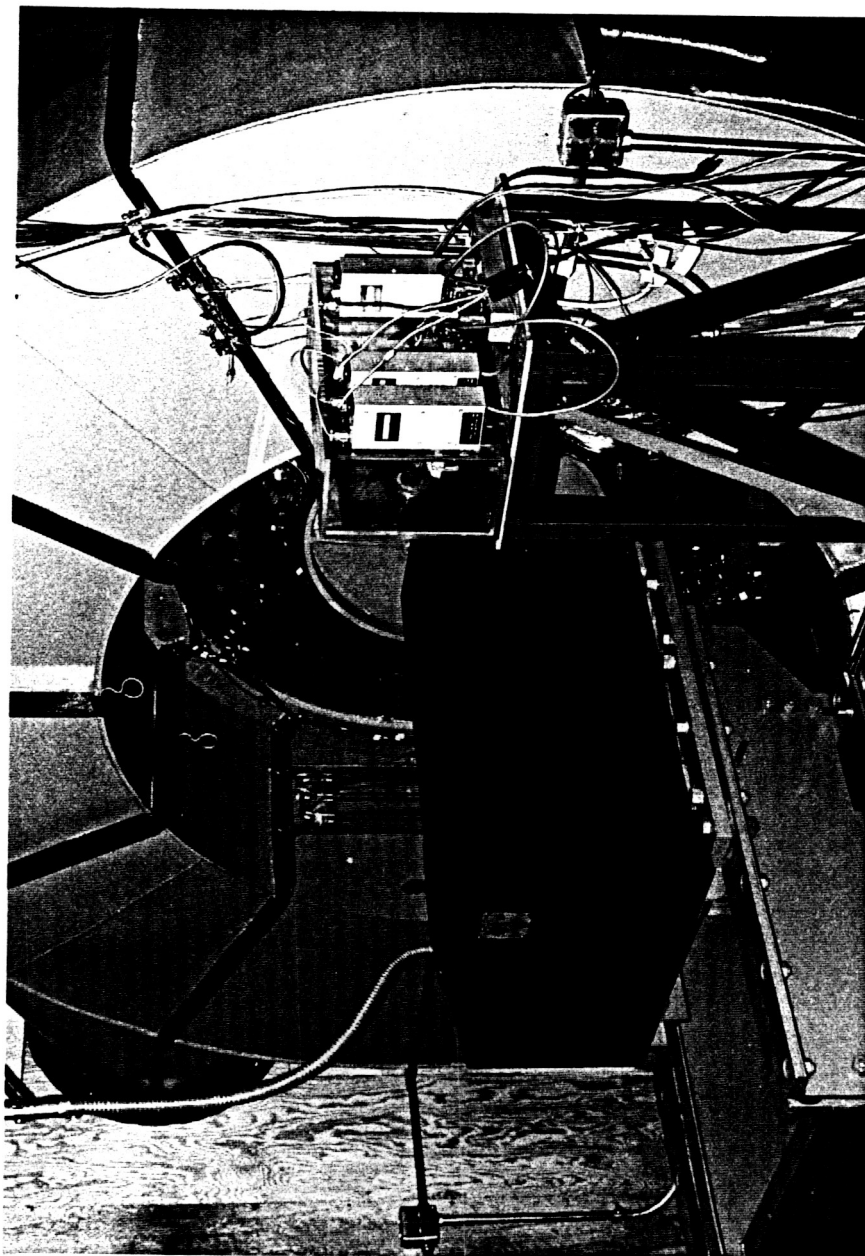


Figure 2.2 Rear View of Compressor Test Facility

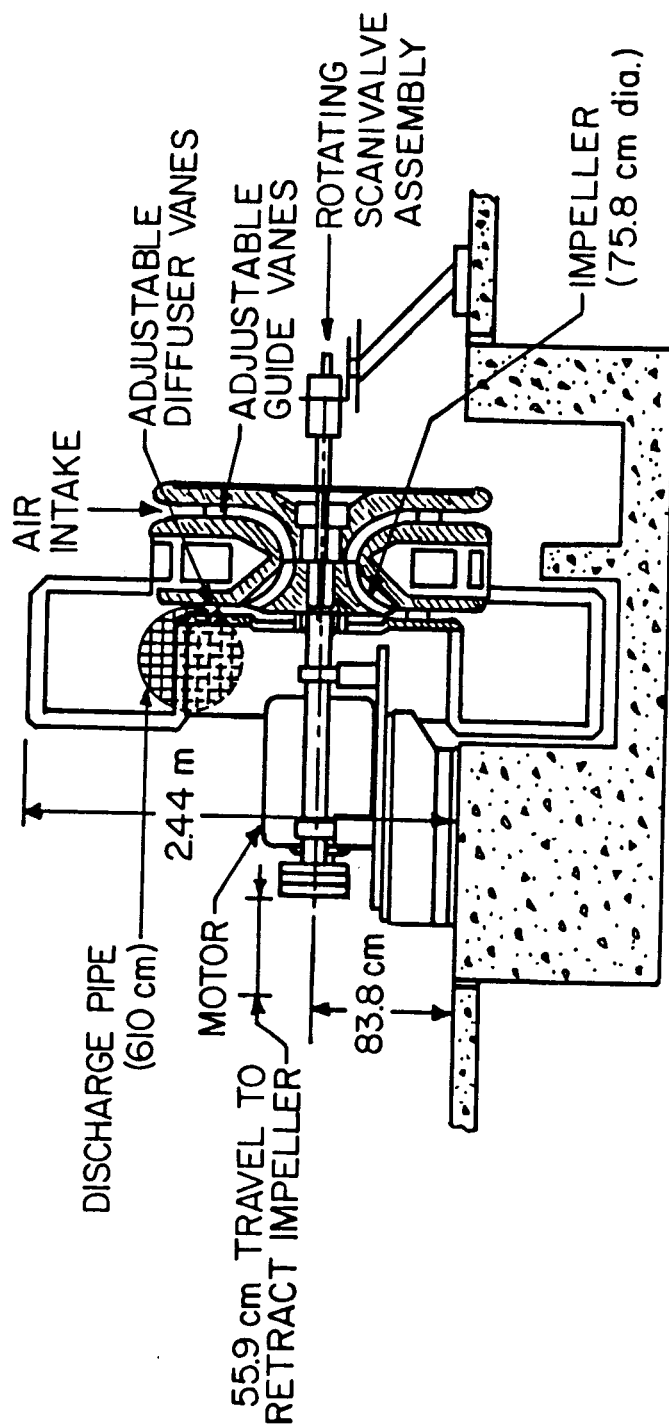


Figure 2.3 Cutaway of Compressor Test Facility

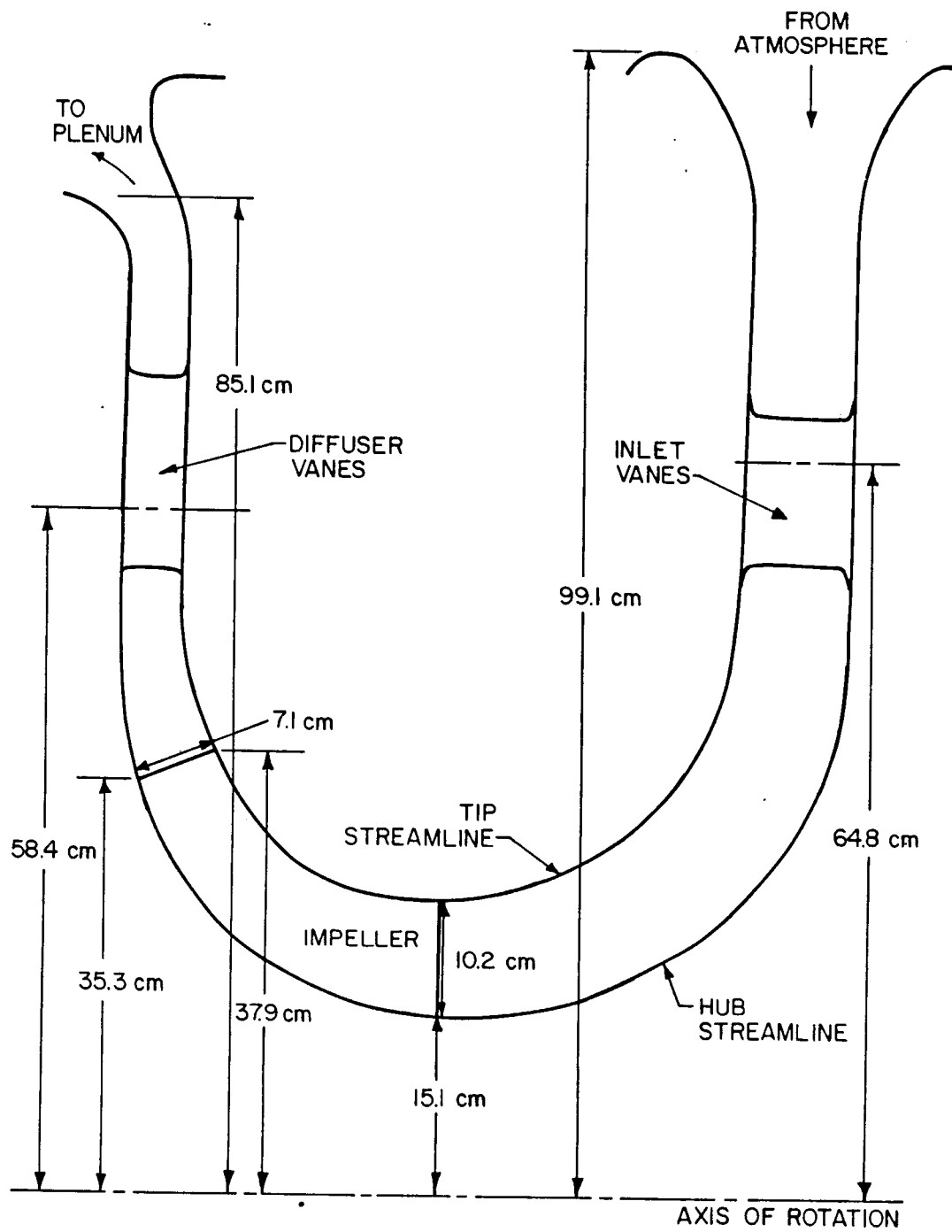


Figure 2.4 Inlet, Impeller, and Diffuser Flow Channel

plane perpendicular to the axis of the machine. The air then passes through a row of stationary diffuser vanes oriented so as to reduce the tangential component of the air velocity.

The air is then discharged into a large annular plenum chamber. From this plenum, the air passes into a straight discharge pipe which contains a sharp edged orifice for flow rate measurement and a throttle valve to regulate the flow rate.

Impeller and Drive Assembly

The impeller and drive assembly are shown in Figure 2.5. The impeller consists of 23 aluminum blades cast integrally with the hub. The tip is covered with a steel shroud for aerodynamic purposes. The impeller has front and rear labyrinth seals with approximately 0.38 mm (0.015 in.) clearance. The impeller inlet hub and tip diameters are 30.2 cm (11.9 in.) and 50.5 cm (19.9 in.) respectively. The exit hub and tip diameters are 70.6 cm (27.8 in.) and 75.7 cm (29.8 in.) respectively.

A mixed-flow impeller configuration is used with a deloaded blade shape. In a mixed-flow impeller, the flow channels never turn to a completely radial direction. Therefore, the flow maintains an appreciable component of velocity in the axial direction during its entire passage through the impeller. With an impeller of this type, the blade need not lie in a purely meridional plane, but may follow a spiral path along the hub from inlet to exit. The use of a spiral type of flow path introduces a great deal of flexibility into the aerodynamic design and permits use of a deloaded blade design. In a general way, this is an impeller blade on which the pressure side is concave over the first part of its length and essentially convex over

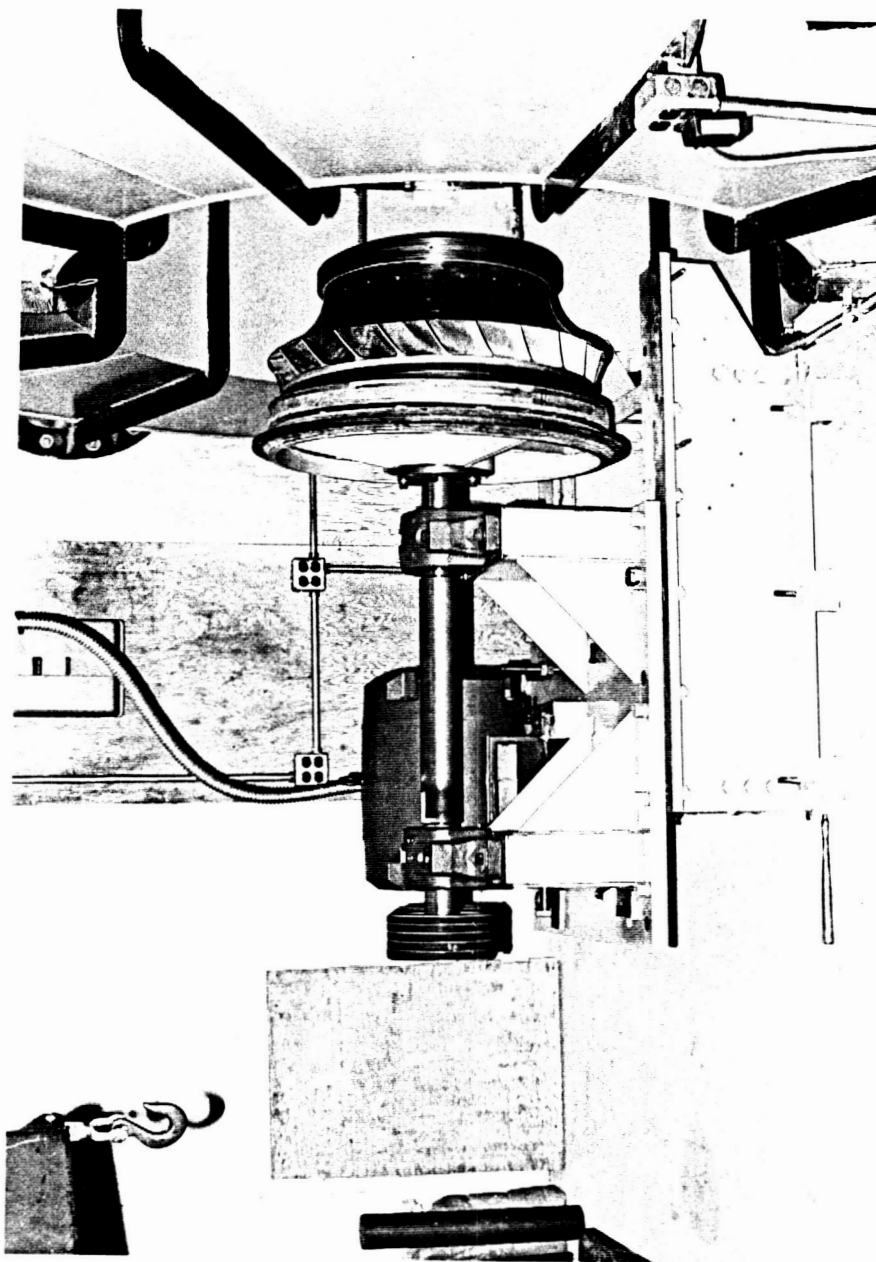


Figure 2.5 Impeller and Drive Assembly

the last part. This reversal of curvature tends to reduce the aerodynamic loading near the blade exit and increase the loading over the central portion of the blade. Figures 2.6 and 2.7 give a side and front view of the impeller. The shroud and front labyrinth seal can be seen as well as the blade configuration.

The pressure distributions in the impeller blade passages are measured with static pressure taps on the blade surfaces. There are 32 such taps, with two redundant pairs, located along three streamlines at five normal locations. These are shown in Figure 2.8. The pressures on the impeller are measured using a rotating pressure multiplexer, described in Chapter 3.

The impeller is driven by a 7.6 cm (3 in.) diameter shaft supported by two tapered roller bearing and pillow block assemblies. The shaft is belt driven by a three phase 29.8 kW (40 hp) induction motor with a 1:1 pulley ratio at a rotational speed of 1795 rpm. In the present configuration, the compressor draws a maximum of 18.7 kW (25 hp). The pulleys can be changed to achieve a rotational speed of approximately 2400 rpm with the present installation.

The shaft and motor are mounted on a steel base which rolls along a track. Thus, the entire impeller-drive assembly can be retracted to perform any service necessary. When the impeller assembly is retracted, it rides on cam mounted wheels so that the entire assembly can be raised and lowered. When the impeller is in place, the wheels are raised allowing the base to rest in a v-groove in the track. The base and impeller drive assembly are then bolted to the track. The impeller is fixed in the stationary passages by a metal seal which bolts onto the rear passage of the diffuser section downstream of the impeller. The inner part of this seal

ORIGINAL PAGE IS
OF POOR QUALITY

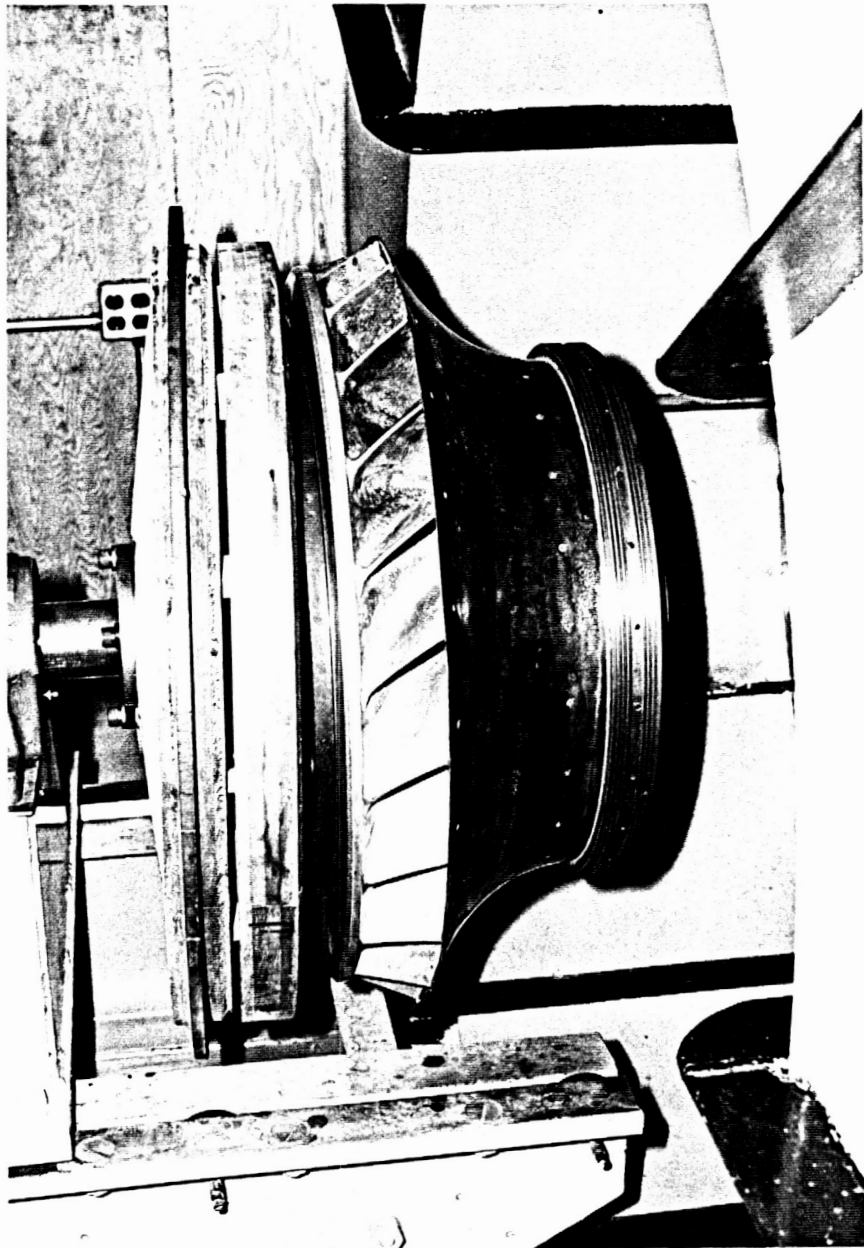


Figure 2.6 Side View of Impeller

ORIGINAL PAGE IS
OF POOR QUALITY

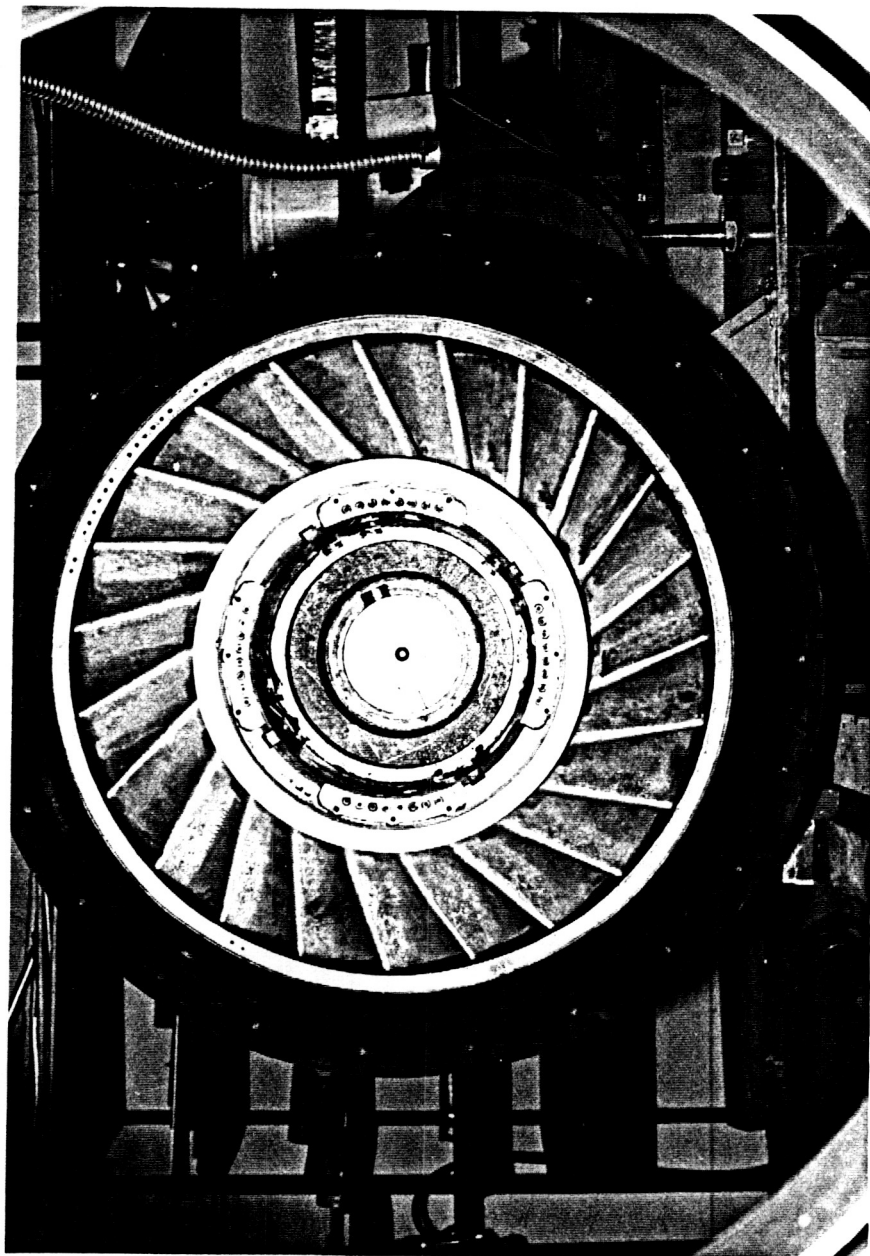


Figure 2.7 Front View of Impeller

ORIGINAL PAGE IS
OF POOR QUALITY

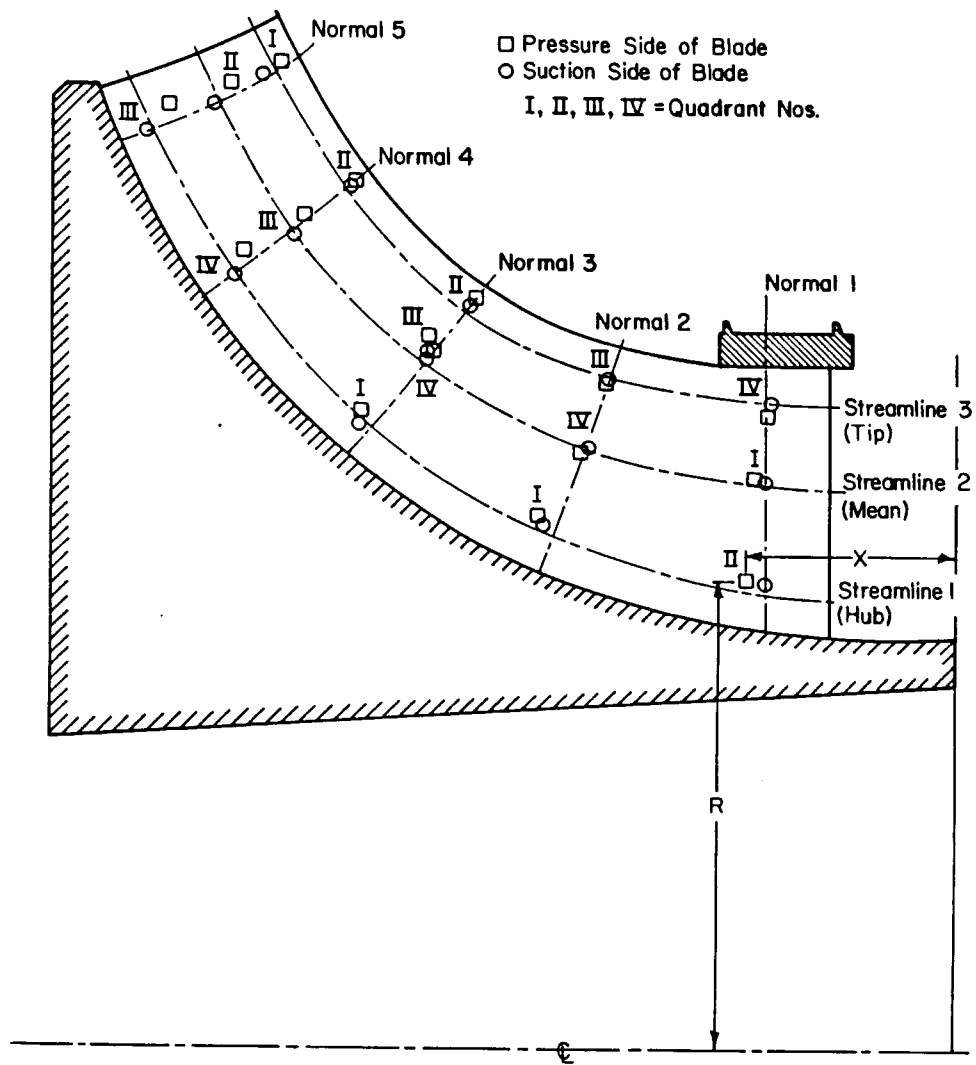


Figure 2.8 Impeller Pressure Tap Locations

contains the rear labyrinth seal. These components are shown in Figure 2.5.

Inlet

The inner side of the inlet as well as a profile of the inlet guide vanes are shown in Figures 2.9 and 2.10. The inlet channel sections are made of wood and contain 38 aluminum guide vanes. These guide vanes are NACA 0015 airfoil sections with a chord length of 12.7 cm (5.0 in.). The guide vanes are nominally oriented radially. Prewhirl in either direction can be imparted to the impeller inlet flow field by adjusting the vane angular position to -15° , 0° , 15° , 30° , or 45° .

Eighteen static pressure taps are located on the walls of the inlet section to allow measurement of the static pressure distribution. Their distribution is shown in Figures 2.11 and 2.12. Three probes are also positioned at the exit of the inlet section, equally spaced circumferentially, to measure the impeller inlet total pressure, temperature, and flow angle. Their location shown in Figure 2.13. Each inlet probe has 5 total pressure taps, a two-tube yawmeter probe, and a thermocouple, as shown in Figure 2.14. The probes are mounted in holders which have an angular vernier with coarse and fine adjustments to measure the probe setting angle, Figure 2.15.

The probes were calibrated using the calibration jet facility developed by Bergsten [9]. The sensitivity of the yawmeter is given by Equation 2.1 [10],

$$\xi = \frac{p_L - p_R}{1/2 \rho V^2 \theta} \quad (2.1)$$

where p_L and p_R are the left and right yawmeter pressures, ρ is the fluid density, V

ORIGINAL PAGE IS
OF POOR QUALITY

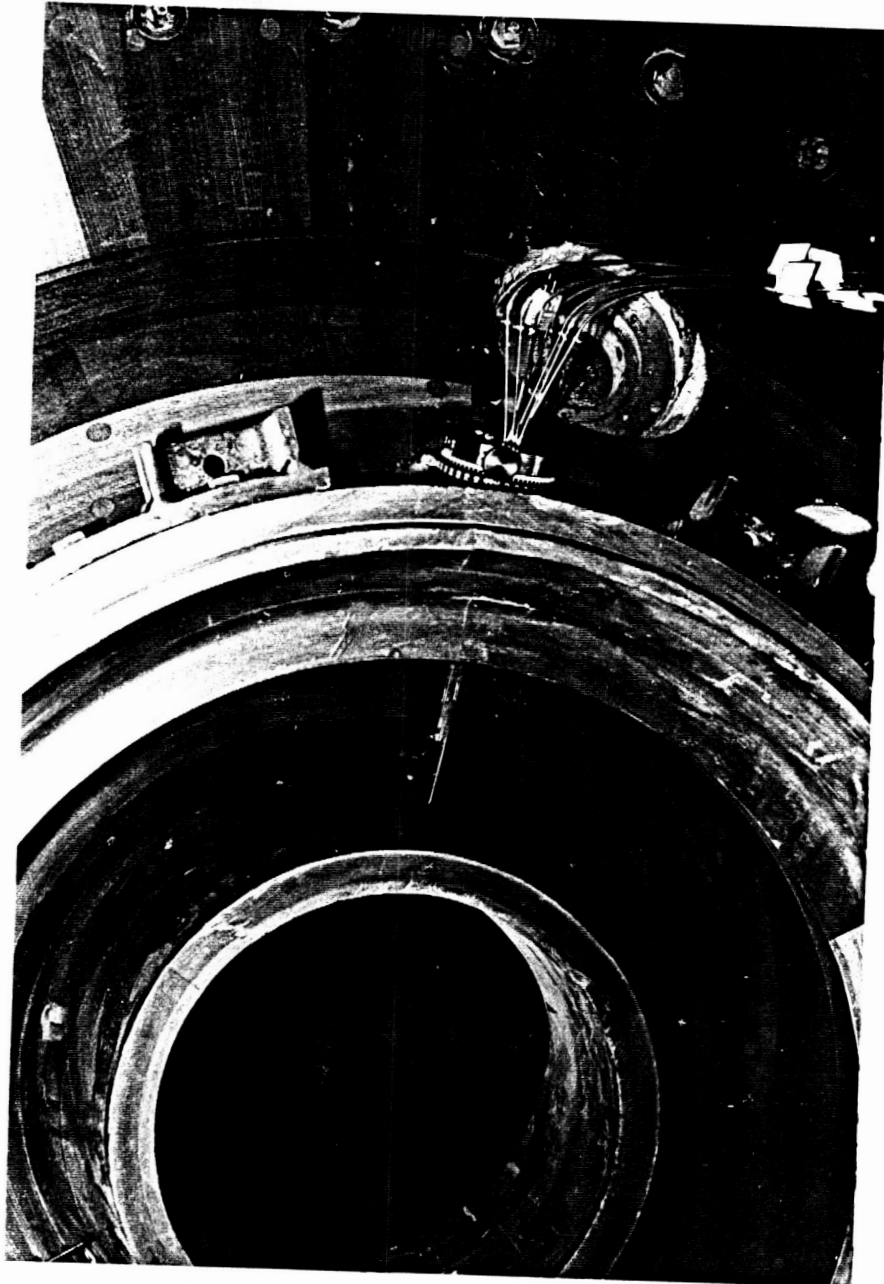
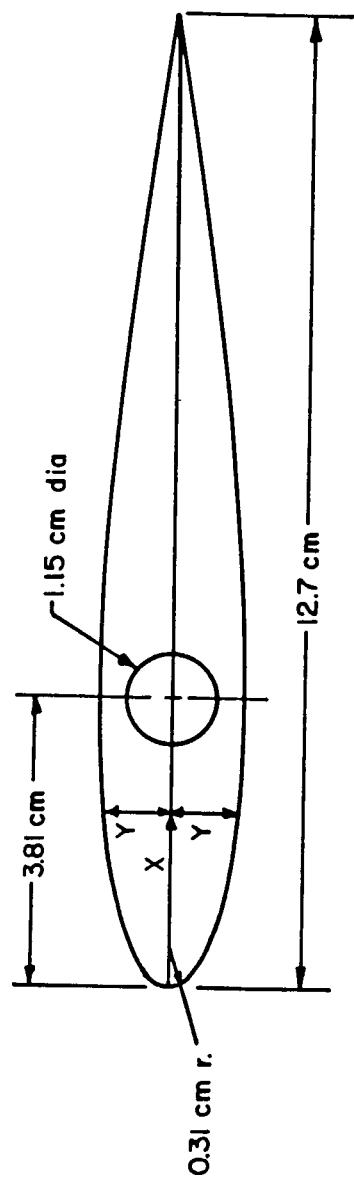


Figure 2.9 View of Inner Side of Inlet



NACA 0015 AIRFOIL SECTION

Figure 2.10 Inlet Guide Vane Profile

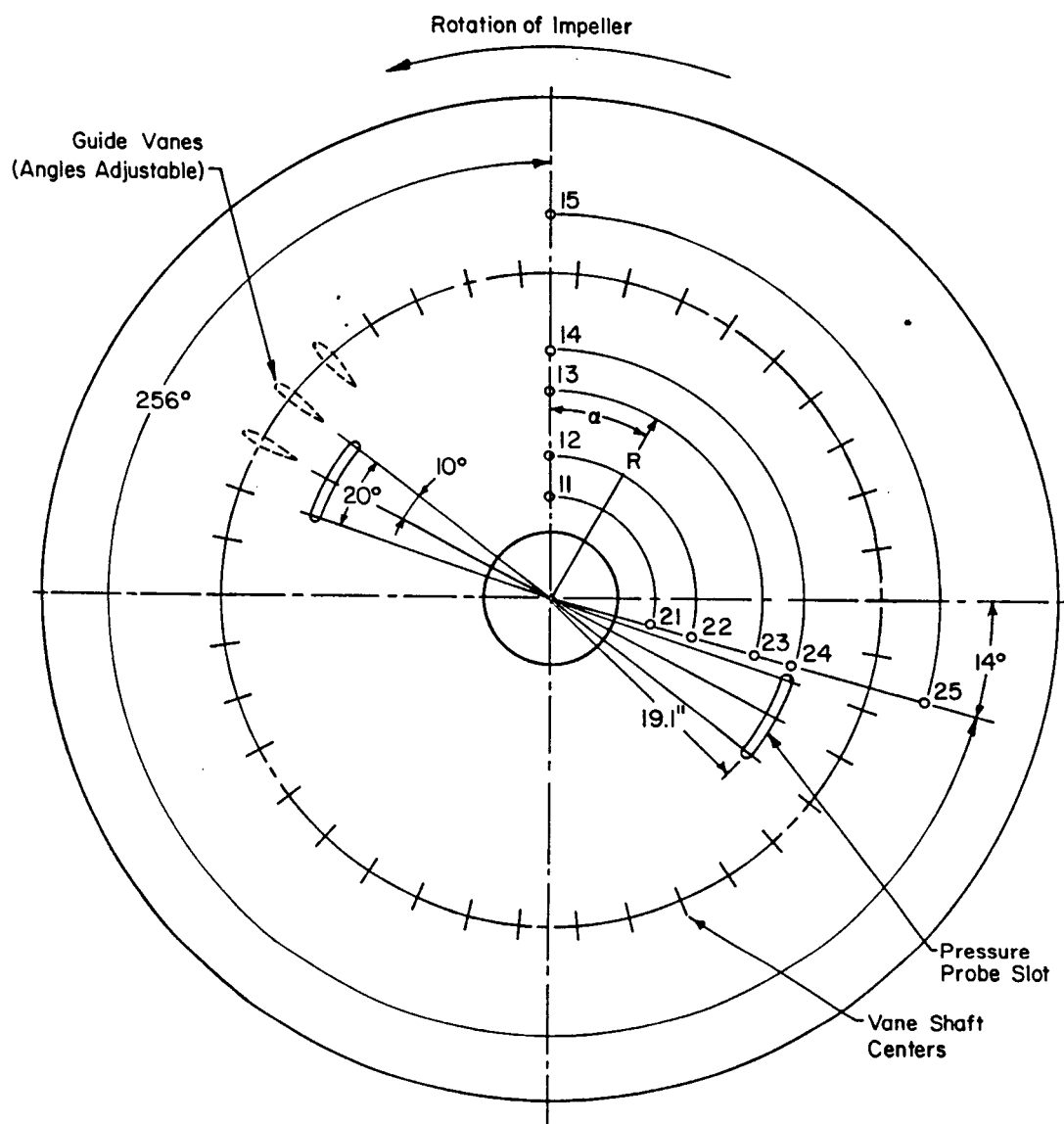


Figure 2.11 Pressure Taps on Inlet Hub Streamline

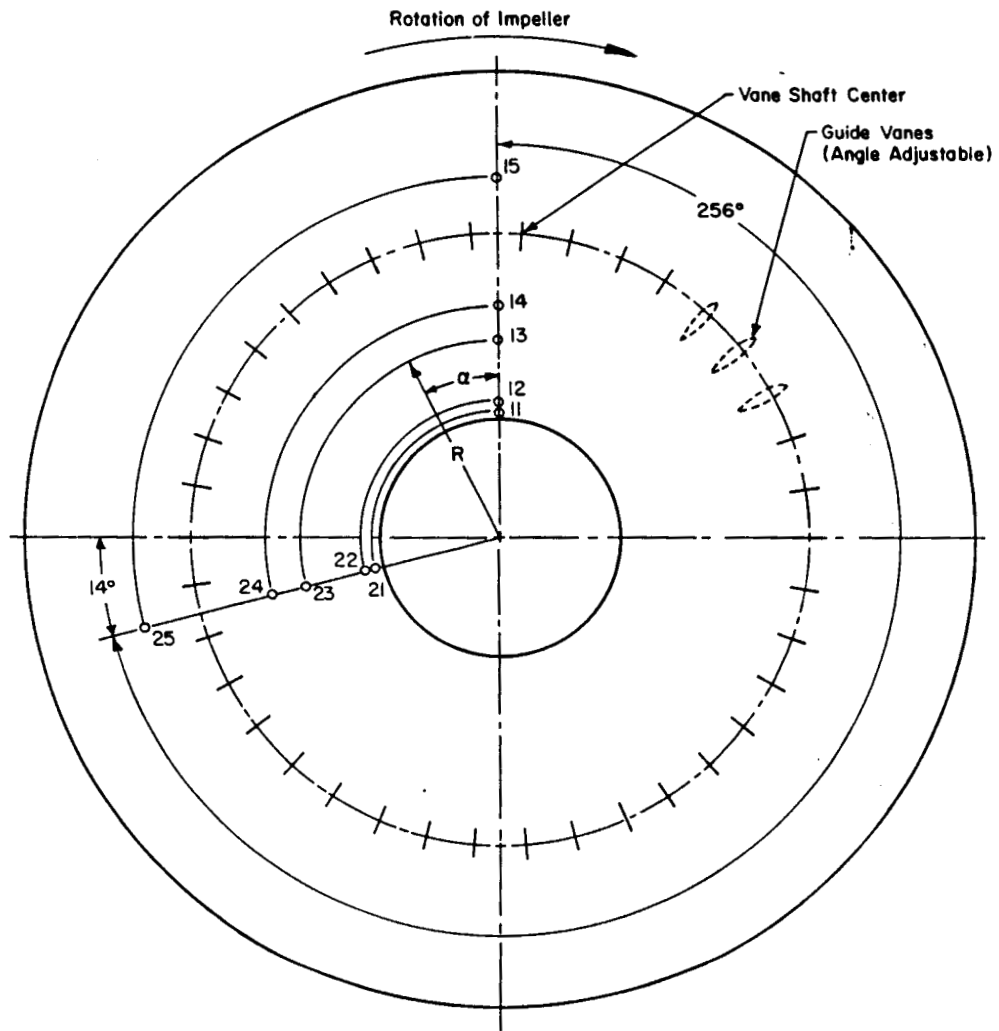


Figure 2.12 Pressure Taps on Inlet Tip Streamline

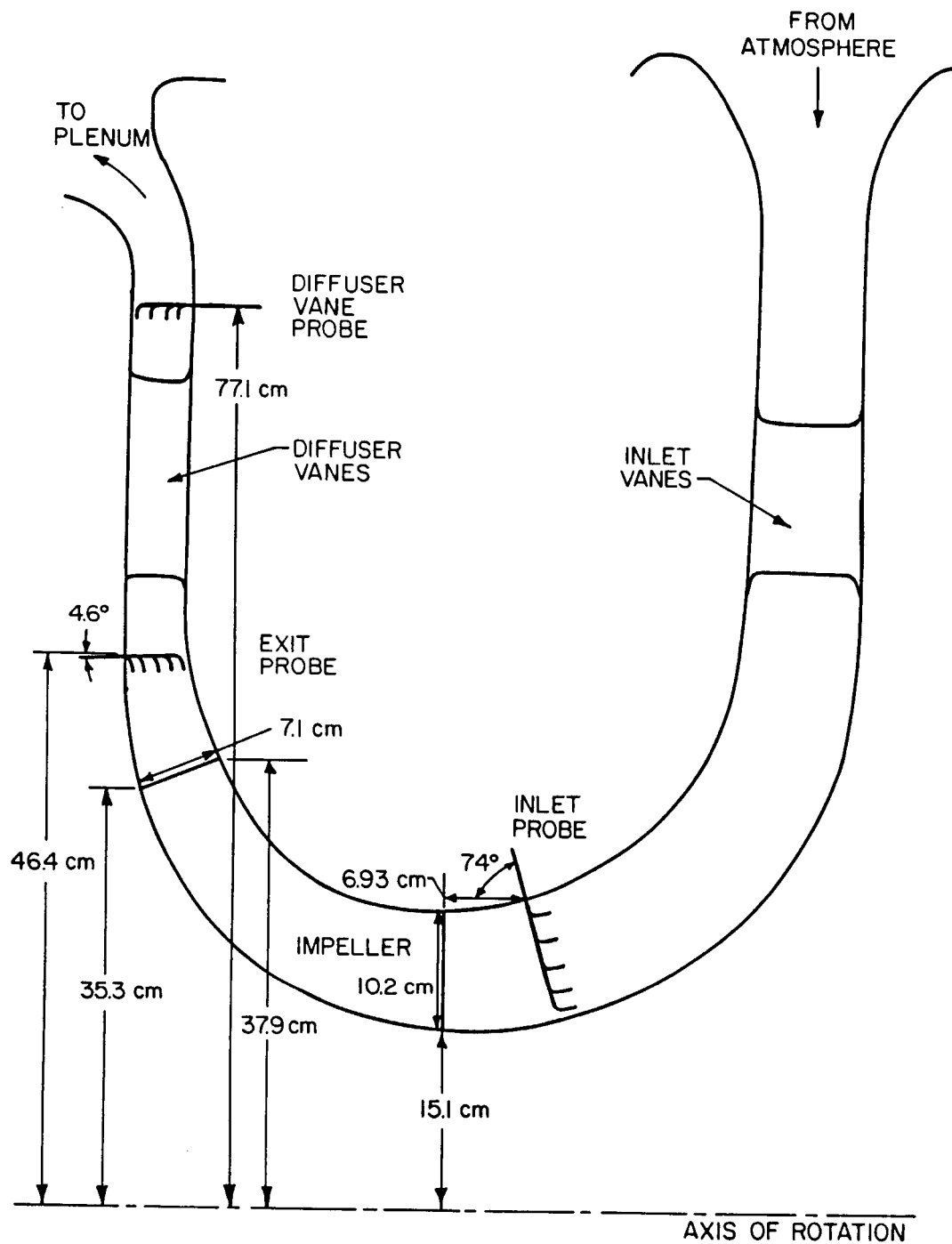
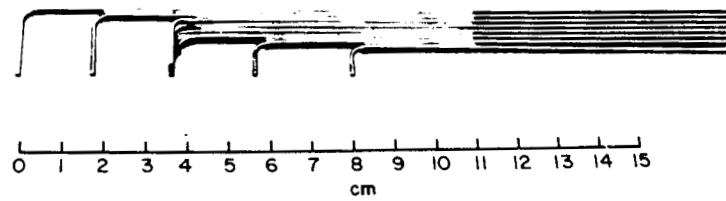
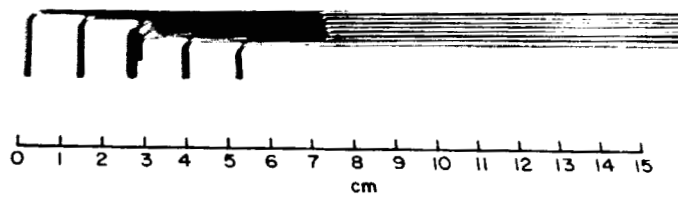


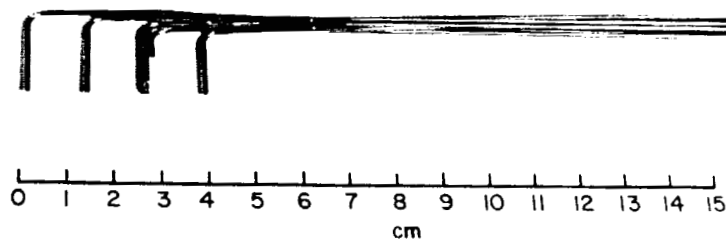
Figure 2.13 Pressure Probe Locations



a) Impeller Inlet Probe



b) Impeller Exit Probe



c) Diffuser Exit Probe

Figure 2.14 Pressure Probes

ORIGINAL PAGE IS
OF POOR QUALITY

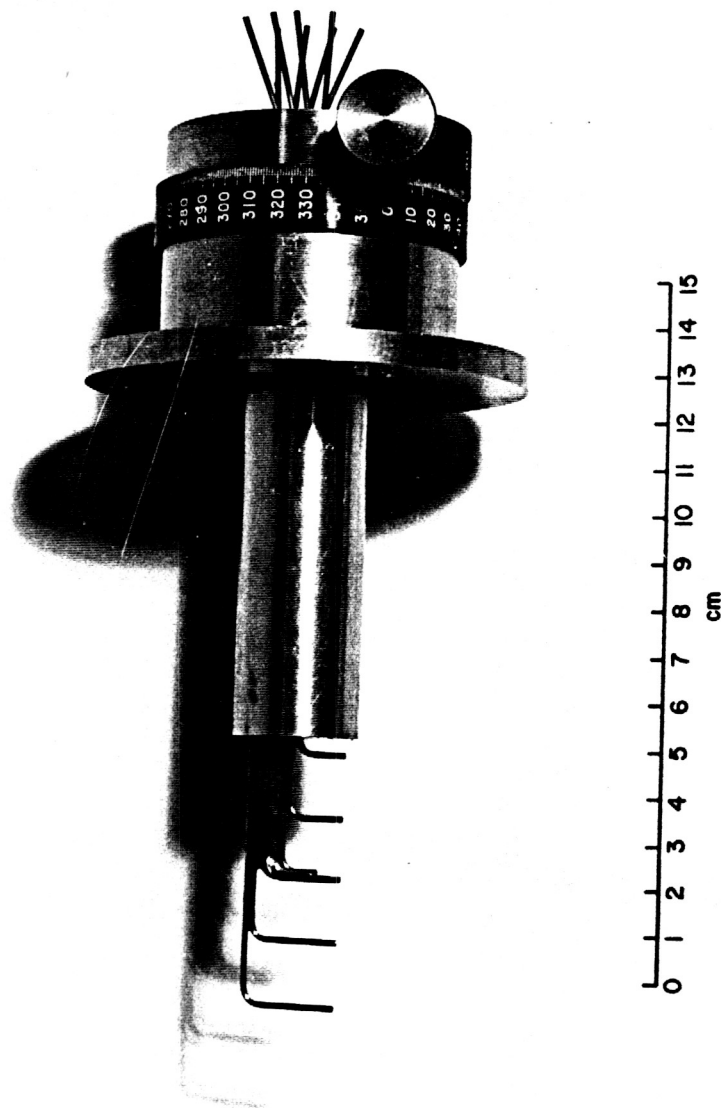


Figure 2.15 Probe Mounted in Holder

is the flow velocity, and θ is the probe yaw angle. The sensitivity of the yawmeter was found to be 0.060. The probe total pressure was within 1% of the true total pressure for up to $\pm 10^\circ$ of misalignment. The null orientation of the probes was determined by adjusting the setting angles of the probes to balance deflections in the two legs of a water manometer while the probes were mounted in the calibration jet. The worst case sensitivity was determined by considering the lowest mass flow rate. A 1° misalignment would result in a pressure differential of 0.38 mm (0.015 in.) of water. The sensitivity of the flow angle measurement would then be no greater than $\pm 2^\circ$.

Diffuser

The exit diffuser is similar in construction to the inlet. It is comprised of two wooden sections with 42 guide vanes, shown in Figures 2.16 through 2.18. These diffuser guide vanes are NACA 4312 airfoil sections with a chord length of 16.5 cm (6.5 in.). The guide vanes are continuously adjustable for angle by loosening the bolt passing the vane and setting the vane according to a vernier mounted on each vane. These bolts also serve to hold the two inlet sections together, as shown in Figure 2.16.

The diffuser section is instrumented with 102 static pressure taps located on the channel walls. These are shown in Figures 2.19 and 2.20. Forty-five additional pressure measurements are made on the diffuser vanes. These are accomplished by means of 15 static pressure taps on each of vanes 4 through 12 of Figure 20, every third of which is redundant as per Figure 2.21. In particular, there are five

ORIGINAL PAGE IS
OF POOR QUALITY

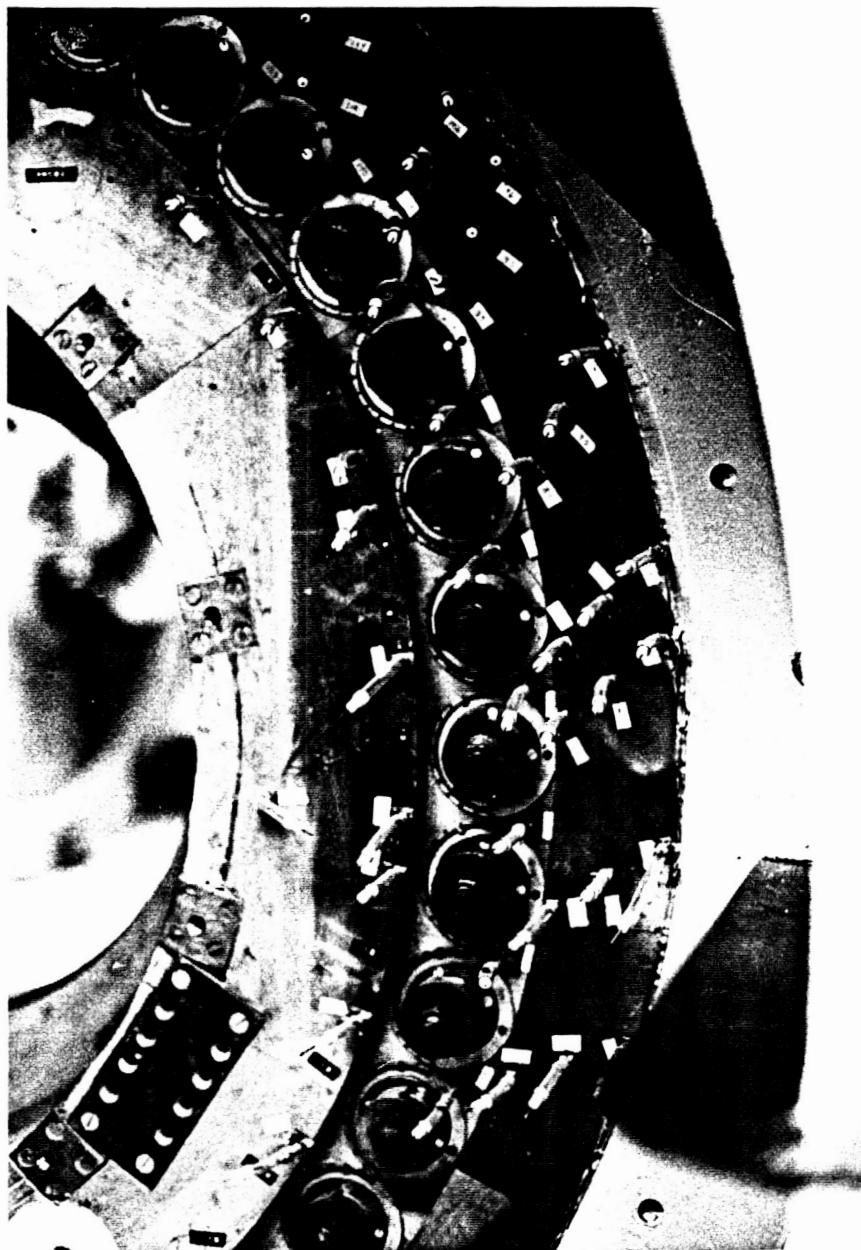
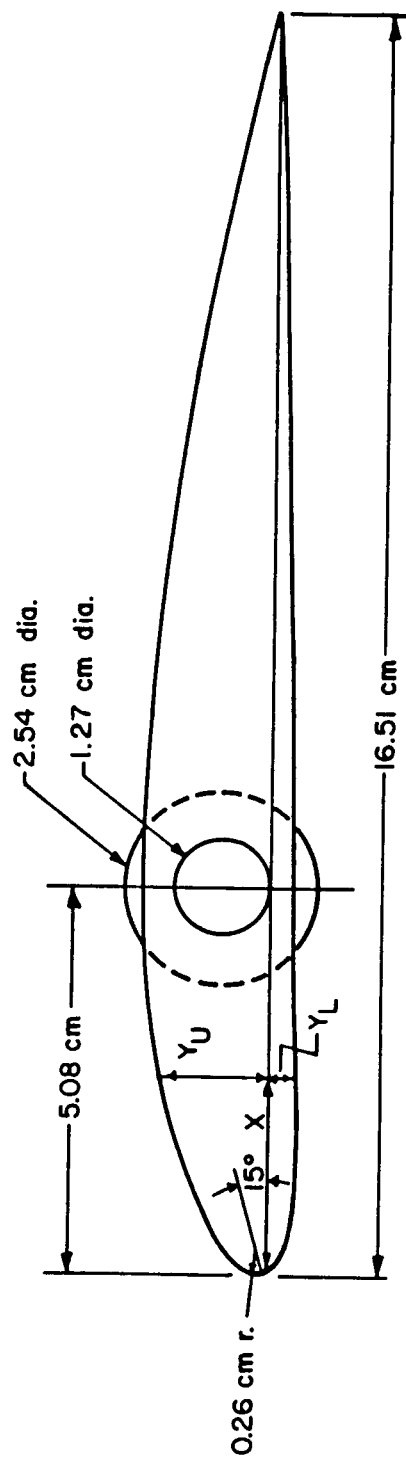


Figure 2.16 Rear of Diffuser Section

ORIGINAL PAGE IS
OF POOR QUALITY



Figure 2.17 Front of Diffuser Section



NACA 4312 AIRFOIL SECTION

Figure 2.18 Diffuser Guide Vane Profile

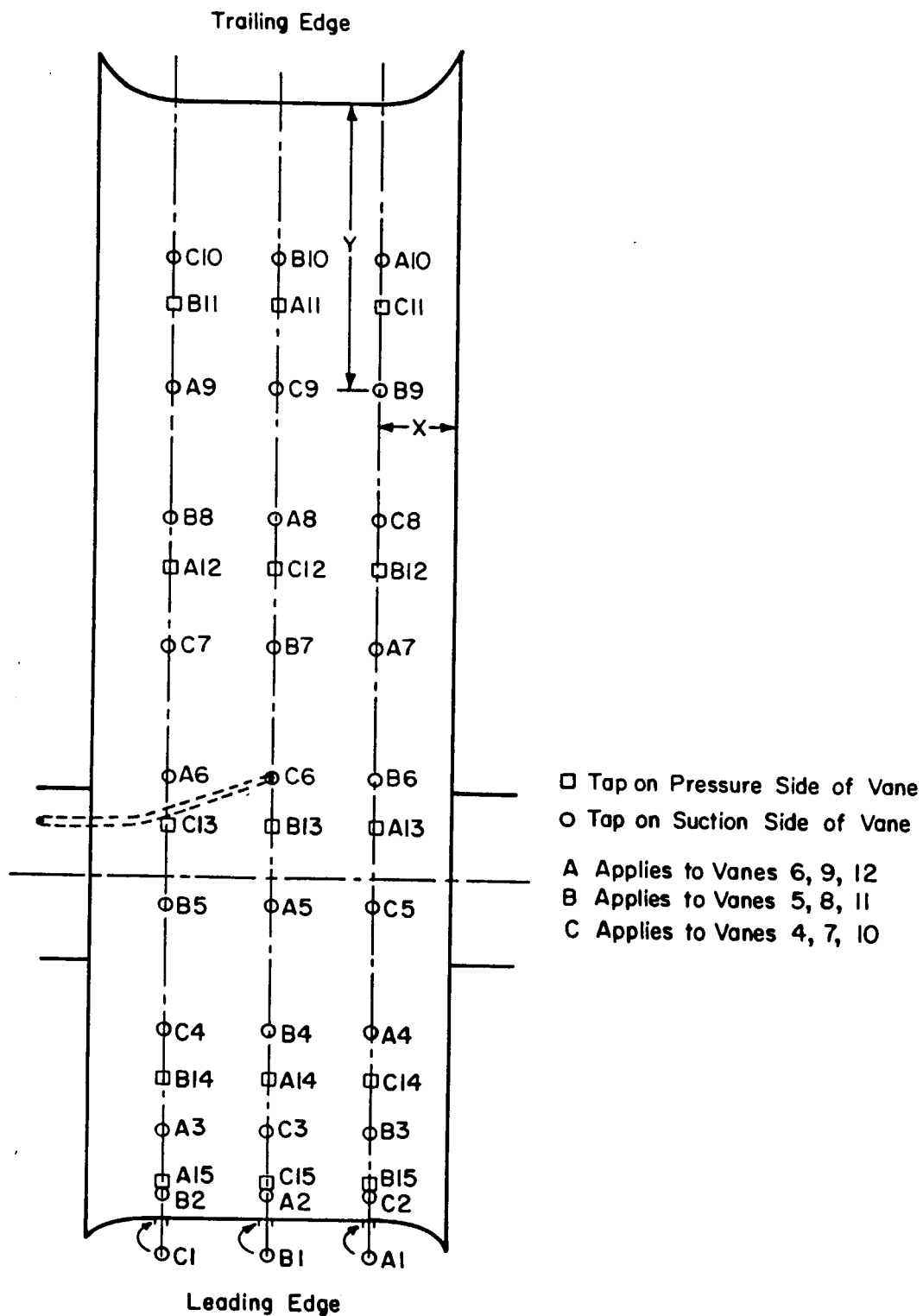


Figure 2.21 Diffuser Vane Static Pressure Taps

pressure surface and ten suction surface static pressure taps at each of three spanwise positions. In addition, four total pressure probes identical to the impeller inlet probes (except for the tube spacing) are located in the diffuser section. Three of these probes are located at the impeller exit. The fourth probe is located behind the diffuser vanes and is mounted on a traversing slide so that flow surveys can be made in the diffuser exit. The probes are shown in Figures 2.14 and 2.15.

Plenum

The plenum is shown in Figures 2.22 and 2.23. It is circular with a square cross section and is constructed of 6.4 mm (0.25 in.) steel plate. The inner diameter of the plenum is 1.69 m (66.4 in.), the outer diameter is 3.15 m (123.9 in.), and the width is 74.2 cm (29.2 in.). The plenum outlet is circular with a 70.0 cm (24 in.) i.d. The steel frame between the inlet and diffuser sections bolts to the plenum and both the frame and plenum are then bolted to the floor. These two sections form the main facility structure. The pressure in the plenum is measured with a static pressure tap on the plenum wall.

Exhaust Piping

The exhaust piping system is shown in Figures 2.24 and 2.25. It is composed of several sections of 3.2 mm (0.125 in.) steel bolted together. As air leaves the plenum, it enters a 90° elbow with an inner diameter of 70.0 cm (24.0 in.). A reducer is connected to the elbow and the inner diameter is decreased to 40.6 cm (16 in.). A straight section of 40.6 cm (16 in.) inner diameter and a length of 18 pipe diameters is connected to the reducer. To remove any swirl or skewing of the

ORIGINAL PAGE IS
OF POOR QUALITY

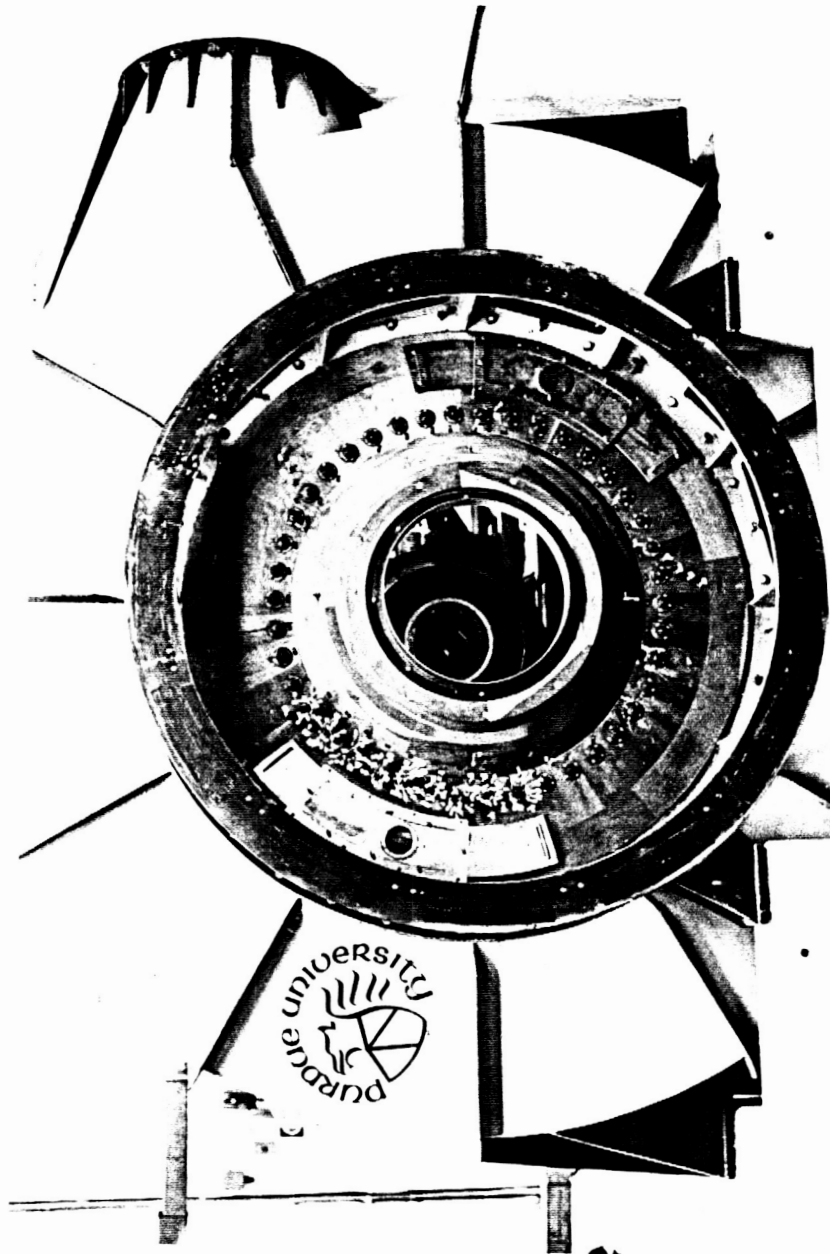


Figure 2.22 Facility Under Construction Showing Plenum

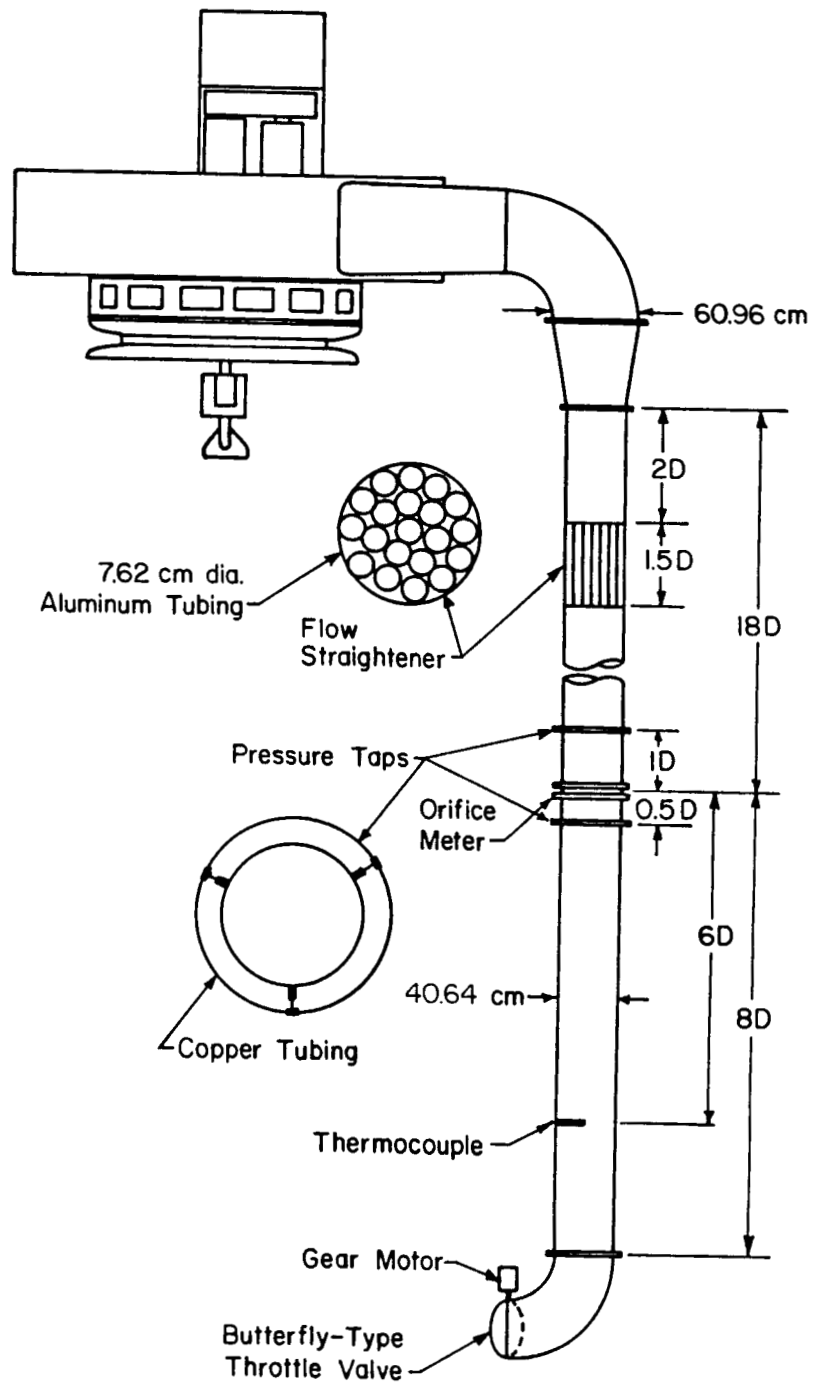


Figure 2.23 Overhead Schematic of Test Facility

ORIGINAL PAGE
BLACK AND WHITE PHOTOGRAPH

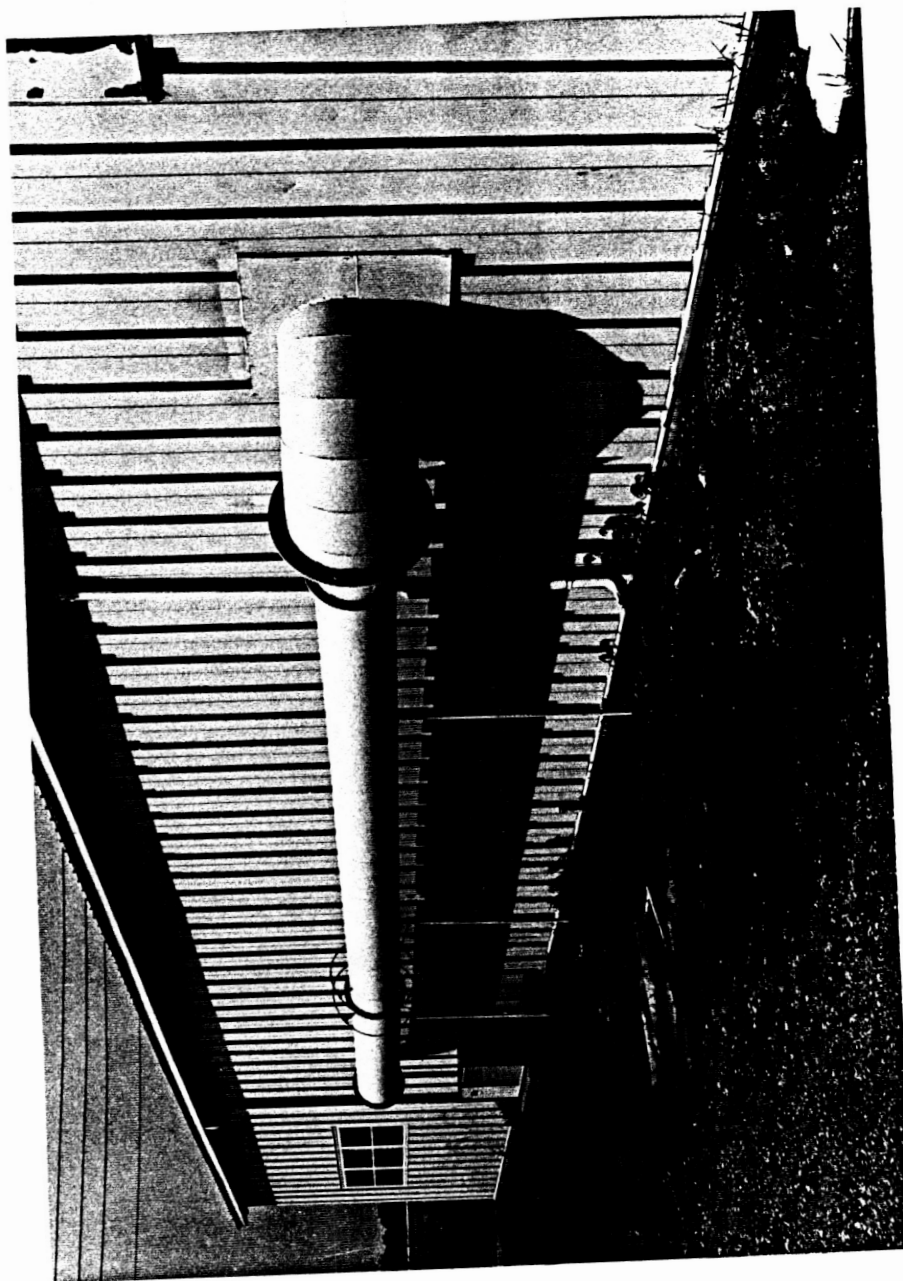


Figure 2.24 Exhaust Piping

ORIGINAL PAGE
BLACK AND WHITE PHOTOGRAPH



Figure 2.25 Exhaust Piping Showing Orifice Location and Pressure Taps

velocity profile, a 55.9 cm (22 in.) long flow straightener made of 7.6 cm (3 in.) diameter aluminum tubing is located 2 pipe diameters downstream of the reducer. A sharp edged orifice plate with 1-diameter and 1/2-diameter pressure taps is located at the end of this straight section for measuring the mass flow rate. These taps are shown in Figure 2.25. Two different orifice plates are used having diameters of 24.13 cm (9.5 in.) and 30.48 cm (12.0 in.). This is necessary to cover the complete operating range of the facility and to obtain reasonable pressure drops across the orifice plate.

Another straight section 8 pipe diameters in length is located behind the orifice plate and contains a thermocouple 6 pipe diameters downstream of the orifice. The flow straightener, pipe lengths and orifice plates were constructed in accordance with ASME standards [11]. A butterfly type throttle valve, driven by a gear motor, is located at the exit of the 90° elbow to control the mass flow through the facility, shown in Figure 2.26. The motor is actuated through a set of relays under control of the data acquisition system.

Summary

The physical components comprising the Purdue Research Centrifugal Compressor Facility have been described. The coordinates of the inlet, diffuser, and impeller channels as well as the location of the pressure taps are given in Appendix A.

ORIGINAL PAGE
BLACK AND WHITE PHOTOGRAPH

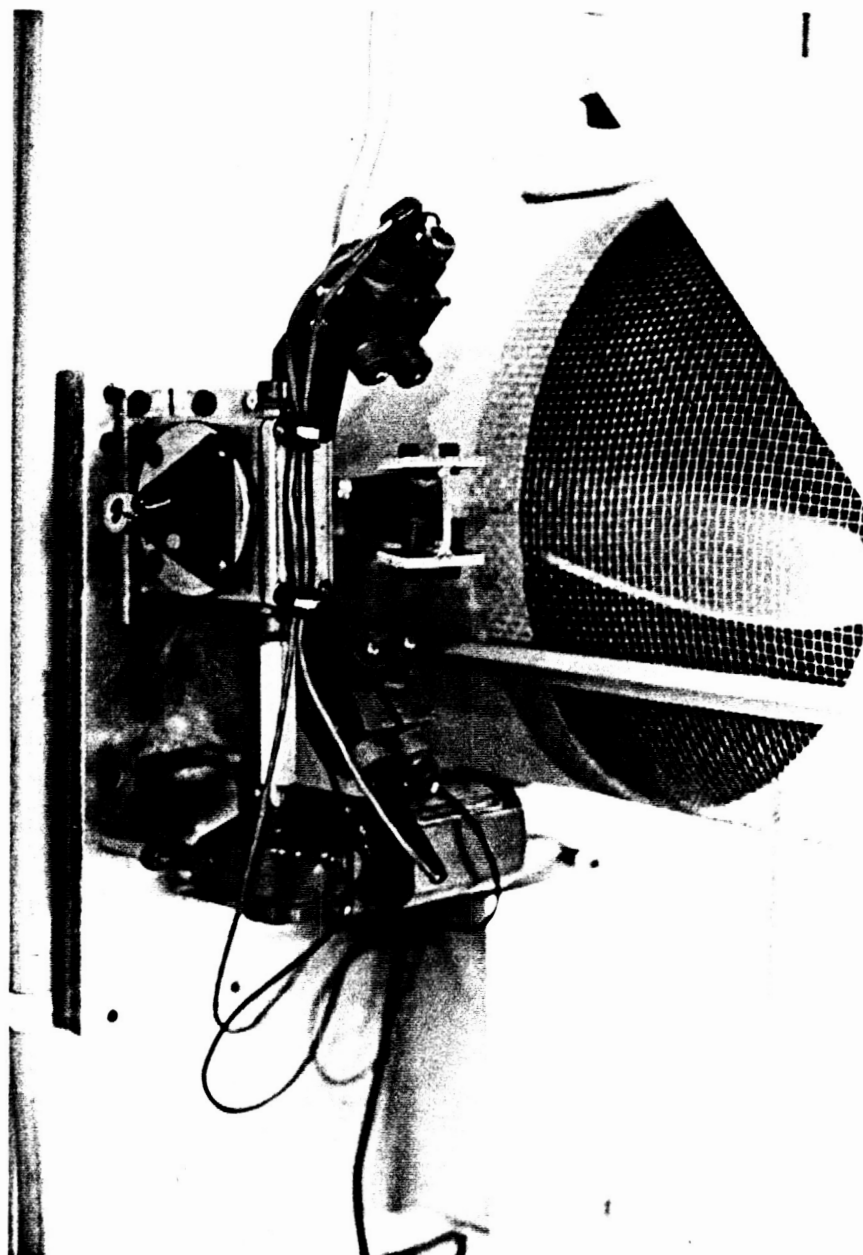


Figure 2.26 Computer Controlled Throttle Plate

CHAPTER 3 - RESEARCH CENTRIFUGAL COMPRESSOR INSTRUMENTATION

Automated data acquisition is essential for efficient acquisition and reduction of data. Since there are a total of 203 pressure measurement locations on stationary passages and probes, an additional 32 rotating static pressure measurements on the impeller, and 8 temperature measurements, data acquisition must be accomplished by means of a computer controlled system.

Stationary Pressure Measurement

The 203 pressures on the stationary components are measured by electrical pressure transducers in conjunction with a pressure multiplexing system (Scanivalve Corporation's valve switching modules #48J9GM-1). Three of these modules are connected to a single solenoid drive unit. Each module has 48 pressure inputs and successively exposes each of these inputs to a single Scanivalve PDCR22-1 psid strain gage transducer. Each of the three transducer outputs is amplified by a Recording Devices' SCSG/D0-5V/0-1 psi signal conditioner. The resulting voltage is read by the computer data acquisition system.

The transducers operate by exposing the back of the diaphragm to a known constant pressure, and the front to the pressure to be measured. The resulting output voltage is linearly proportional to the pressure difference, as shown in Appendix B. However, the slope and intercept of the calibration curve can drift slowly with time. Drift is eliminated by calibrating the transducers each time a scan is made. The voltage output at zero pressure difference and the voltage output at a reference pressure are also measured during each calibration. A linear calibration of the transducer is then made using these two points.

Pressures both above and below ambient are encountered in the research compressor facility. Calibration pressures above and below the maximum and minimum in the test facility are therefore required. The rear of the transducer diaphragm, as well as the home port on the Scanivalve, are exposed to ambient pressure. A reference pressure below ambient is connected to Port 1 and a reference pressure above ambient is connected to Port 2. Using the transducer output at each of these three points, a separate calibration is made for pressures above ambient and for pressures below ambient. This is necessary because the response of the transducer can be different for positive and negative pressure differentials.

The transducers are calibrated each time a scan is made. The computer compares the transducer voltage at zero pressure difference with the voltage of the measured pressure, to determine if the positive or negative calibration is to be used. Each pressure is successively calculated in this manner.

The reference pressure system is shown in Figure 3.1. A vacuum pump supplies air at pressure both above and below ambient pressure. The pressure and vacuum outputs of the pump are each connected to a plenum and pressure regulator. Each of these pressures is read on a leg of a three leg water manometer with ambient on the third leg.

The Scanivalve operation is controlled by a solenoid controller which sends voltage pulses to the unit on command from the computer. The controller can receive two commands. The first steps the module to the home position (Port 48) and the second steps the module to the next port. This allows the computer to

ORIGINAL PAGE
BLACK AND WHITE PHOTOGRAPH

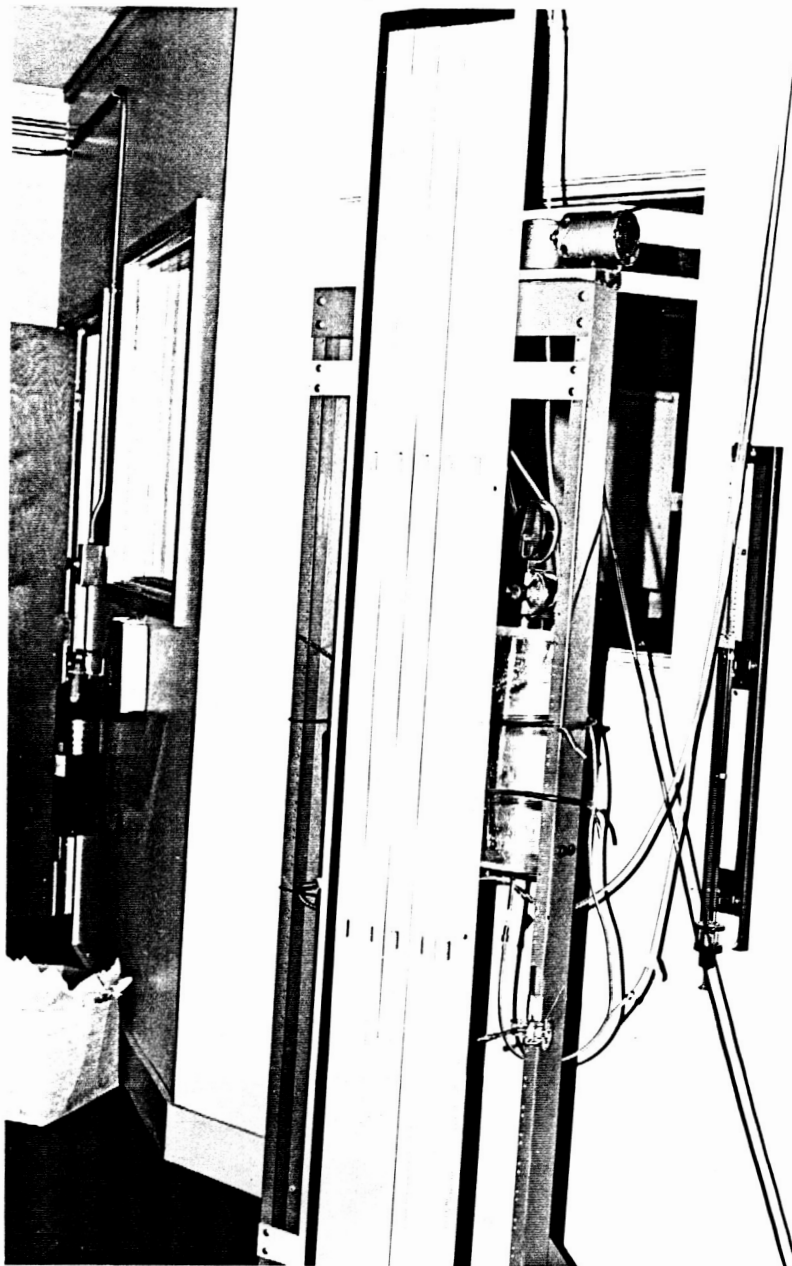


Figure 3.1 Reference Pressure System and Manometer

ORIGINAL PAGE
BLACK AND WHITE PHOTOGRAPH

control the entire Scanivalve operation.

The complete three valve switching module assembly is shown in Figure 3.2. The module is mounted in a plexiglass box. The pressure lines from the test facility are not directly connected to the module but rather are connected using Scanivalve's bulkhead connectors and quick disconnect couplings. This is done to eliminate direct contact with the valve switching module and to provide enough pressure measurement ports for all of the pressure taps. In particular, each module has 46 available pressure measurement ports for a total of 138. Since 203 pressures are to be measured, two of the disconnects must be switched during data acquisition. The initial installation of the above pressure measurement system is described in Reference [12].

Rotating Pressure Measurement System

The impeller is instrumented with 32 static pressure taps on the rotating blade passages. The measurement of pressures in a rotating reference frame is not as straightforward as the corresponding measurements in a stationary frame. To measure the rotating static pressures, Scanivalve Corporation's 36TR rotating Scanivalve pressure multiplexer is employed, seen in Figure 3.3. It is used in conjunction with Scanivalve's PDCR23D-2.5 psid pressure transducer and Recording Devices' SCSG10 $\pm 5V/VG$ signal conditioner.

The 36TR rotating Scanivalve multiplexer is able to measure 36 static pressures. A multiplexing module that rotates with the impeller is used. Because this module is rotating, a pneumatic stepping motor is used to advance the

ORIGINAL PAGE
BLACK AND WHITE PHOTOGRAPH

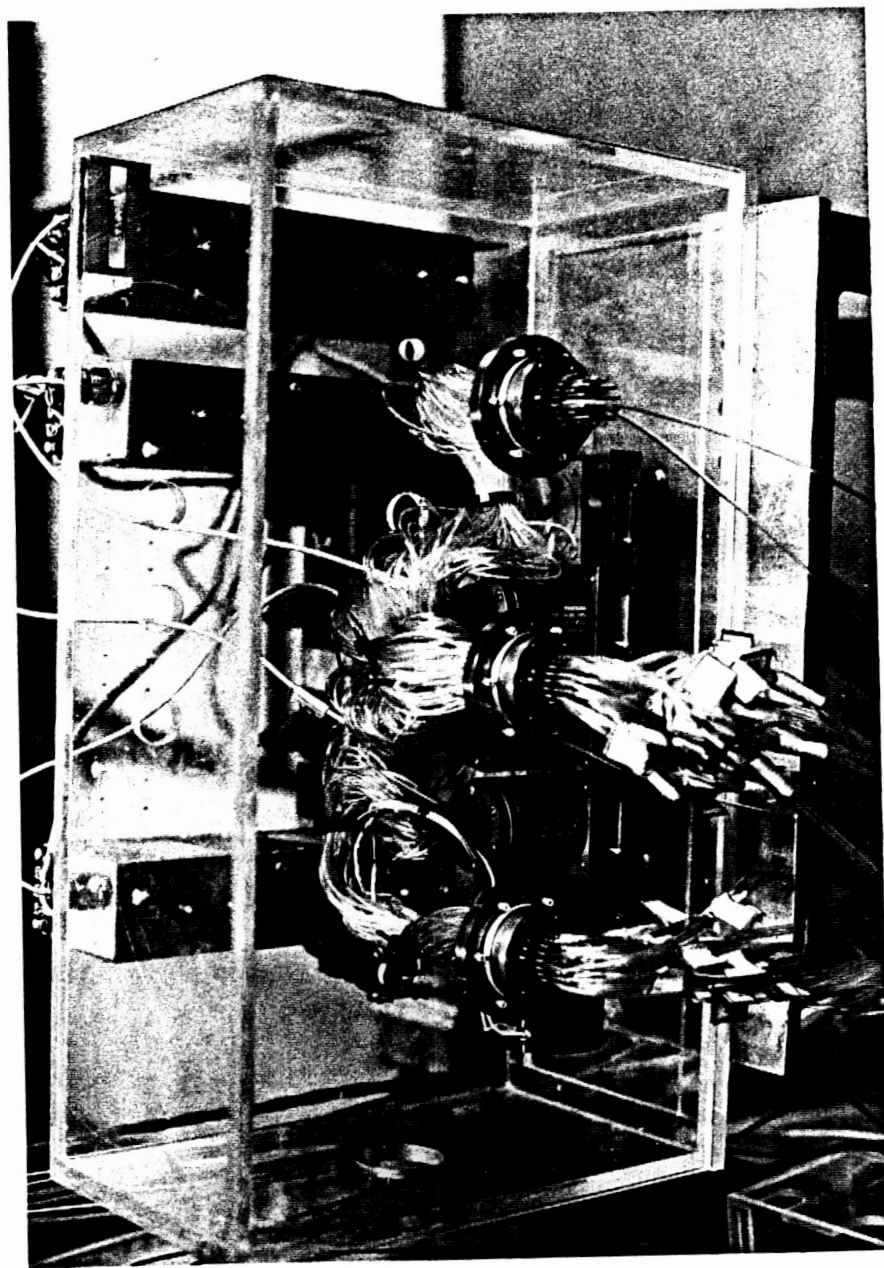


Figure 3.2 Scanivalve Value Switching Assembly

ORIGINAL PAGE
BLACK AND WHITE PHOTOGRAPH



Figure 3.3 Rotating Scanivalve (36TR)

multiplexer from port to port. The air stepping motor has two pressure inputs, one of which steps the module from an odd numbered port to an even numbered port and another which steps it from an even numbered port to an odd numbered port. A pressure of approximately 620 kPa (90 psi) is needed to step the module. Once a pressure is applied to one of the ports, the module will make only one step until the opposite port is pressurized. The position of the multiplexing module is determined by an optical encoder and an odd-even decoder. The pressure from the rotating multiplexing assembly is exposed to a stationary pressure transducer by way of a rotating O-ring gland seal.

Because the pressure measurement frame is rotating, the calibration procedure used on the stationary Scanivalve switching module is not applicable to the rotating Scanivalve. To calibrate the transducer while the Scanivalve is in operation, it is equipped with a feature called ZOC (Zero-Operate-Calibrate). This feature has a pressure operated valve which closes the port from the transducer to the multiplexing module and exposes the transducer to a calibration pressure. Since two separate calibration pressures are needed, an external solenoid controlled valve switches between the two calibration pressures while the ZOC feature is operating. The transducer signal is read by the computer at each of these pressures and the calibration determined.

The operation of the 36TR rotating Scanivalve is controlled by four solenoid air valves which in turn are controlled by the data acquisition system. Two of the solenoid air valves are used along with the building pressure supply to step the scanivalve. A third solenoid is used to operate the ZOC feature and a fourth

bubble tight valve switches between two calibration pressures. The 36TR is connected to the impeller through a manifold and flexible coupling. The entire assembly, without the inlet in place, is shown in Figure 3.4.

Temperature Measurement

Temperatures are measured at 8 locations using copper-constantan (type T) thermocouples. The voltages for the thermocouples are measured by the data acquisition system's voltmeter through an 8 pair extension cable. The voltmeter assembly is discussed in Section 3.4.

Computer Data Acquisition System

The instrumentation is controlled, and the signals analyzed, by a Hewlett-Packard HP-1000 computer interfaced to a Hewlett-Packard HP-3497 data acquisition unit. The HP-3497 has interface cards for various functions. A 20 channel relay multiplexer card is used to multiplex 20 voltage inputs to the HP-3497 internal voltmeter. The voltages of the three pressure transducers in the valve switching assembly and the transducer on the rotating assembly are read using this card. A 20 channel relay multiplexer card with type T thermocouple hardware compensation is used to connect the thermocouples directly to the voltmeter without any external compensation. The temperature of each thermocouple is then only a function of its voltage. A 15 channel actuator output card is used for relay control of motors and solenoids. The solenoid stepper in the main Scanivalve is stepped and homed with this card. The rotating Scanivalve as well as the motor driving the throttle plate are also controlled with this card. A

ORIGINAL PAGE
BLACK AND WHITE PHOTOGRAPH

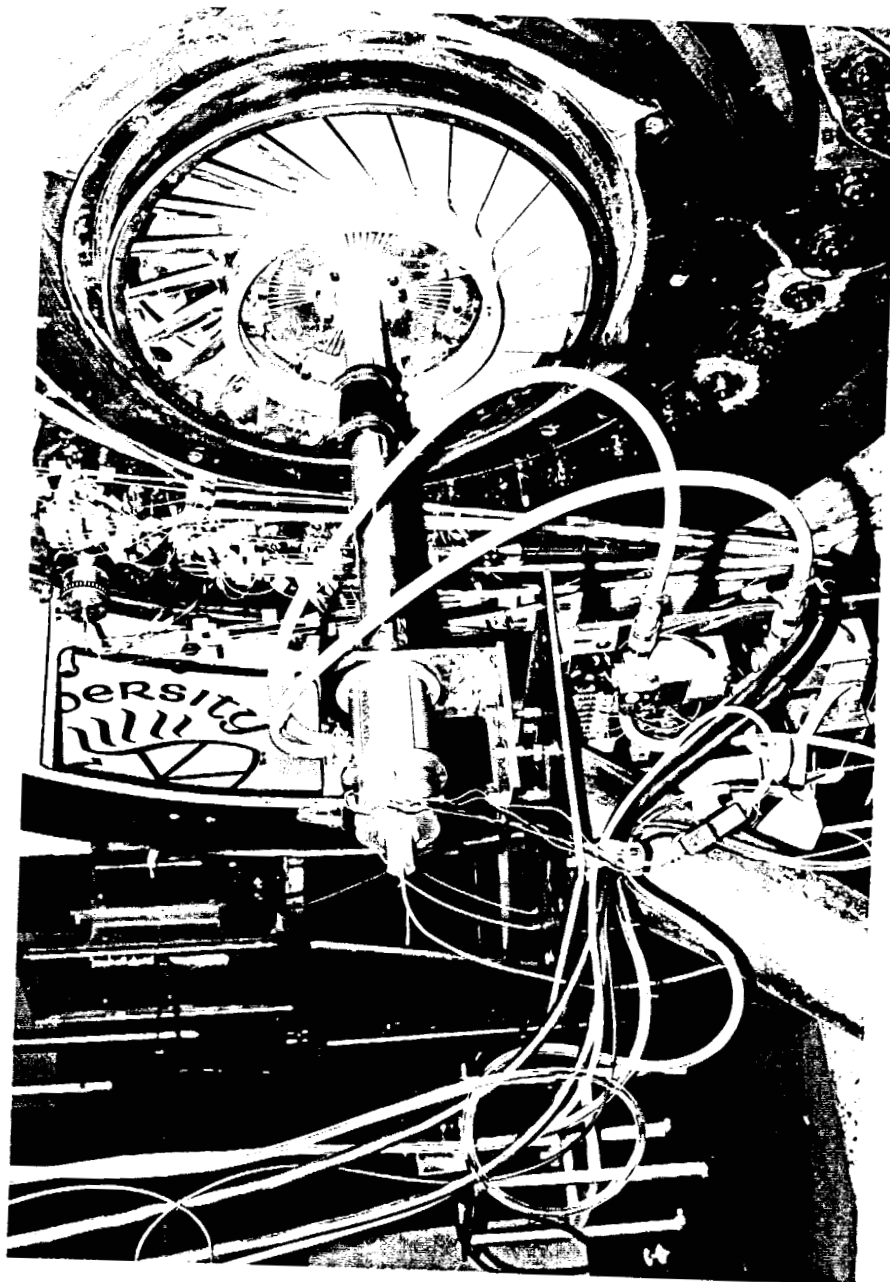


Figure 3.4 Assembled Rotating Pressure Measurement System

digital input card is available to read the position of the rotating Scanivalve from the odd-even decoder.

The HP-1000 computer sends instructions in Fortran to the HP-3497 which performs the directed functions. The HP-3497 then returns the appropriate response to the computer. The control of the system and acquisition of data is discussed in the next chapter.

CHAPTER 4 - DATA ACQUISITION AND ANALYSIS

It is necessary to correctly sample the data and to also quantify the errors and confidence levels associated with each type of measurement. A discussion of the data analysis, sources of error, and methods for determining the uncertainties in the data are described in this chapter.

Stationary Pressure Measurement

The pressures in the Research Centrifugal Compressor are measured with a pressure multiplexing system wherein the transducers are exposed to various pressure inputs. When the module is stepped to a port, the transducers experience a step input. Since the transducers are second order devices, there is a time interval required for the transducer signals to settle to a steady state value. Scanivalve's transducer specification states that the transducers will settle to within 0.1% of the true output within 100 msec when a 27.6 kPa (4 psi) pressure step is applied to the transducer through a 508 cm (200 in.) length of tubing [13]. Two seconds is allowed in the data acquisition routine after each step, a time interval more than sufficient to allow for settling.

The voltage output of the pressure transducers is proportional to the pressure difference across the transducer. As previously stated, two transducer calibrations are made. While the rear of the transducer diaphragm is exposed to ambient pressure, the front of the diaphragm is sequentially exposed to ambient pressure, and a positive and negative gage calibration pressure. The transducer voltage is measured at each point and any subsequent pressure applied to the transducer is calculated as follows:

$$P = P_{cal} \left(\frac{v - v_0}{v_{cal} - v_0} \right) \quad (4.1)$$

where v_0 is the transducer voltage at zero pressure difference, P_{cal} is the calibration gage pressure, v_{cal} is the transducer voltage at the calibration pressure, and P and v are the actual pressure input and voltage output of the transducer at any given pressure.

There are two types of errors that occur in the measurement of any quantity: random errors and systematic errors. The systematic errors are associated with the calibration of the transducers. Namely, any transducer will have some nonlinearity. Thus, there is some error resulting from the linearity assumption. The random errors are due to the static accuracy of the transducers and the scatter of the data.

The error due to the nonlinearity is small as compared to the random error. Scanivalve quotes the static accuracy of the transducers to be within 0.06%. A typical pressure uncertainty is on the order of 0.5%. Therefore, the main source of error is due to data scatter and the uncertainty of the measurements and is the only error considered.

To find the uncertainty in the pressures calculated from the transducer voltage measurements per Equation 4.1, it is first necessary to find the uncertainty in the quantities upon which the measurement depends. The quantities v_{cal} and v_0 are measured by the data acquisition system from Ports 1 and 2 of the scanivalve modules. The voltage v is measured at each port of the scan. The computer reads each of these quantities a specified number of times, and calculates the sum of

these readings and the sum of the squares of these readings. The mean, \bar{v} , and standard deviation, s , are given by Equations 4.2 and 4.3 where n is the number of samples.

$$\bar{v} = \frac{\sum v}{n} \quad (4.2)$$

$$s = \left(\frac{n \sum v^2 - (\sum v)^2}{n(n-1)} \right)^{1/2} \quad (4.3)$$

This is only a finite sampling out of an infinite sample population. Therefore, \bar{v} and s are only estimates of the true mean μ and true standard deviation. If it is assumed that all samples come from a population which is normally distributed, then a confidence interval for the true mean can be found using Student's t -distribution. The true mean can be bounded with any desired confidence level as follows

$$\bar{v} - \frac{s}{\sqrt{n}} t < \mu < \bar{v} + \frac{s}{\sqrt{n}} t \quad (4.4)$$

where t comes from Student's t -distribution and is dependent upon the confidence level and the number of samples [14]. In the current investigation, 30 samples were used for all data.

The uncertainties in the voltage readings are taken from a 95% confidence interval for the true mean. That is, the uncertainty of the voltage is $\frac{s}{\sqrt{n}} t$, with t evaluated for a 95% confidence level and 30 samples. The value for P_{cal} is not measured by the computer, but rather is read from a manometer and entered by

the operator. It is the difference between the high manometer level and the low manometer level multiplied by the density of water and the acceleration of gravity. The uncertainty for each manometer reading is half of the smallest division or 0.127 cm (0.05 in.) of water.

The uncertainty in the pressure data, e_p , can be calculated, once the uncertainties for the above quantities have been determined:

$$e_p = \left(\sum_i (w_{x_i} \frac{\partial P}{\partial x_i})^2 \right)^{1/2} \quad (4.5)$$

where, w represents the uncertainty of the quantity denoted by its subscript and x_i represents the i th quantity upon which the pressure measurement depends.

Rotating Pressure Measurement

The measurement of the pressures on the rotating impeller blades is similar to the measurement of the pressure in the stationary passages with one exception. When measuring the pressures in the rotating frame, the transducer is mounted on the axis of rotation but the pressure taps are at off-axis radii. Thus, the angular acceleration of the impeller causes a pressure gradient in the tube leading to the pressure tap and the pressure measured by the transducer is significantly lower than the value at the tap. A correction for this difference can be applied by considering a force balance on an element of fluid in a tube, Figure 4.1. Setting the sum of the forces equal to the acceleration and reducing yields:

$$(P - (P + dP))A = -m\omega^2 r$$

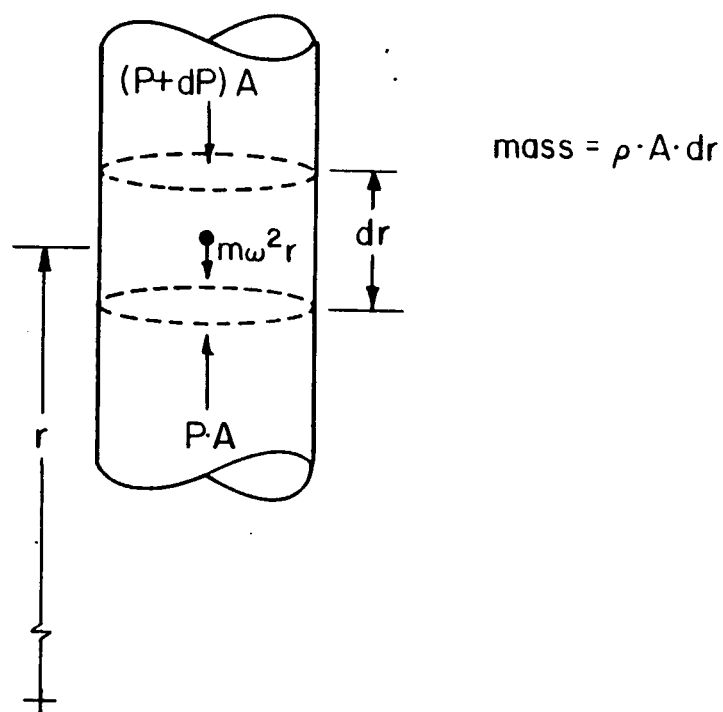


Figure 4.1 Rotating Fluid Element Kinetic Diagram

$$-AdP = -(A\rho dr)\omega^2 r$$

$$dP = \rho\omega^2 r dr \quad (4.6)$$

where P is the pressure in the tube, ρ is the fluid density, ω is the rotational speed, and r is the radius of the fluid element.

The density, ρ , can be expressed in terms of the pressure, the fluid temperature, T , and the gas constant, R , by the perfect gas equation.

$$\rho = \frac{P}{RT} \quad (4.7)$$

Rearranging terms and integrating from the axis, which is at zero radius, to the radius of the impeller pressure tap gives:

$$dP = \frac{P}{RT} \omega^2 r dr$$

$$\frac{dP}{P} = \frac{\omega^2}{RT} r dr$$

$$\int_{P_{\text{axis}}}^{P_{\text{tap}}} \frac{dP}{P} = \frac{\omega^2}{RT} \int_0^{r_{\text{tap}}} r dr$$

$$\ln\left(\frac{P_{\text{tap}}}{P_{\text{axis}}}\right) = \frac{\omega^2 r^2}{2RT}$$

$$P_{\text{tap}} = P_{\text{axis}} \exp\left(\frac{\omega^2 r^2}{2RT}\right). \quad (4.8)$$

Equation 4.8 relates the pressure measured at the axis of the impeller to the pressure at the tap in terms of the tap radius, the rotational speed and the

temperature, which is assumed to be constant along the tube.

Since all of the quantities in Equation 4.8 are known or measured, the pressure at the transducer face can be corrected to give the true static pressure at the tap. After correcting for the rotational effects using Equation 4.8, the measurement and analysis of the rotating pressures on the impeller is the same as for the stationary measurement. The uncertainty in the pressure is then derived from the uncertainties in the independent variables by using Equation 4.5.

Temperature Measurement

The temperature measurements are much less complicated than the pressure measurements. The voltages for the eight thermocouples are read by the data acquisition system a specified number of times. The uncertainty due to data scatter is then calculated in the same manner as used for the pressure. The conversion from voltage to temperature is done through a ninth order polynomial for type T thermocouples [15]. The systematic error of the polynomial is 0.5°C (0.9°F). The total uncertainty due to random and systematic errors is calculated using Equation 4.5.

Compressor Performance

Once the pressures and temperatures have been measured, the computer calculates certain parameters which relate to compressor performance. The performance parameters of a turbomachine can be expressed in two ways. If the density changes through the machine are small, the overall performance can be expressed by defining a dimensionless pressure rise coefficient:

$$\Psi = \frac{P_{02} - P_{01}}{1/2\rho U_2^2} \quad (4.9)$$

where P_{02} is the impeller exit total pressure, P_{01} is the impeller inlet total pressure, ρ is the air density, and U_2 is the wheel speed at the mean exit diameter.

In addition, the efficiency and the power coefficient can be defined as

$$\eta = \frac{(P_{02} - P_{01})/\rho}{U_2 c_{\theta 2} - U_1 c_{\theta 1}} \quad (4.10)$$

$$\mathcal{P} = \frac{\text{Power}}{1/2\rho U_2^3 A_2} \quad (4.11)$$

where A_2 is the exit area of the impeller, U_1 is the wheel speed at the mean inlet diameter, Power is the power imparted to the fluid, and $c_{\theta 1}$ and $c_{\theta 2}$ are the impeller inlet and exit absolute tangential velocities respectively.

For a fixed geometry and negligible viscous effects, it can be shown that Ψ , η , and \hat{P} , are functions only of the flow coefficient ϕ , defined as

$$\phi = \frac{Q}{A_2 U_2} \quad (4.12)$$

where Q is the volume flow rate through the machine [1].

For a more general turbomachine analysis considering variable density, the overall performance can be expressed using five parameters. The total pressure ratio across the compressor, $\frac{P_{02}}{P_{01}}$, the efficiency, η , and $\frac{\Delta T_0}{T_{01}}$, are plotted versus

the corrected mass flow, $\frac{\dot{m} \sqrt{\frac{T_{01}}{T_{\text{ref}}}}}{\frac{P_{01}}{P_{\text{ref}}}}$, and the corrected speed, $\frac{\omega}{\sqrt{\frac{T_{01}}{T_{\text{ref}}}}}$.

In the above parameters, T_{01} and P_{01} are the compressor inlet total temperature and pressure, P_{02} is the exit total pressure, ΔT_0 is the stagnation temperature rise, and P_{ref} and T_{ref} are a reference pressure and temperature. The efficiency, considering the flow to be compressible, is then calculated as

$$\eta = \frac{c_p T_{01} \left(\left(\frac{P_{02}}{P_{01}} \right)^{\frac{\gamma-1}{\gamma}} - 1 \right)}{U_2 c_{\theta 2} - U_1 c_{\theta 1}} \quad (4.13)$$

where c_p is the specific heat at constant pressure and γ is the specific heat ratio. The numerator represents the work that would be required to produce the measured pressure rise under isentropic conditions. The denominator is the actual work done on the air by the impeller.

Since the density changes through the Centrifugal Compressor Facility are small at the current operating speed, the performance can be accurately assessed using an incompressible analysis. For consistency with the literature, the performance is also expressed in terms of pressure ratio versus corrected mass flow. The corrected speed is not important here since the speed and inlet total temperature are essentially constant.

Pressures and Velocities

The pressures measured in the test facility are plotted in terms of a pressure coefficient, Equation 4.14.

$$C_p = \frac{P - P_{amb}}{1/2 \rho U_2^2} \quad (4.14)$$

where P is the measured pressure, P_{amb} is the ambient pressure, and the denominator is the same as for the impeller pressure rise coefficient given in Equation 4.9.

The velocities in the facility are calculated using the data from the pressure probe measurements by

$$V = \left(\frac{2\gamma RT_0}{\gamma-1} \left(1 - \left(\frac{P}{P_0} \right)^{\frac{\gamma-1}{\gamma}} \right) \right)^{1/2} \quad (4.15)$$

where P and P_0 are the static and total pressures and T_0 is the total temperature.

CHAPTER 5 - RESULTS

A series of experiments was performed in the Purdue Research Centrifugal Compressor Facility to investigate and quantify the effect of flow rate and inlet flow field prewhirl on the overall and detailed aerodynamic performance. Detailed aerodynamic data were acquired and analyzed over a range of mass flow rates with inlet guide vane settings varied from -15° to 45° . The rotational speed and exit diffuser vane settings were held constant. Primary facility parameters are listed in Table 5.1. The static pressure distributions in the compressor inlet section and on the impeller and exit diffuser vanes as well as the overall pressure and temperature rise and mass flow rate were measured and analyzed at each operating point to determine the overall performance as well as the detailed aerodynamics throughout the compressor.

Overall Compressor Performance

The effect of flow rate and inlet flow field prewhirl on the aerodynamic performance of the impeller is presented in Figures 5.1 through 5.4 in the format of pressure rise coefficient versus flow coefficient, the total pressure ratio as a function of corrected mass flow, and the efficiency and power coefficient versus flow coefficient, respectively. The data shows that increasing the inlet guide vane setting angle and thus the prewhirl, tends to flatten the pressure and efficiency curves. At each inlet guide vane setting less than 45° , there is a region in which the impeller performance is superior to the other inlet guide vane settings either from an efficiency or pressure rise point of view, with the maximum pressure rise on a particular curve found at progressively greater flow rates as the inlet guide vane

Table 5.1 Research Compressor Facility Parameters

Mean Impeller Exit Diameter:	73.2 cm (28.8 in.)
Impeller Inlet Hub Diameter:	30.2 cm (11.9 in.)
Impeller Inlet Tip Diameter:	50.6 cm (19.9 in.)
Impeller Exit Flow Area:	0.16 m ² (1.726 ft. ²)
Impeller Inlet Flow Area:	0.129 m ² (1.39 ft. ²)
Impeller Inlet Blade Angle:	50°
Impeller Exit Blade Angle:	51°, backward swept
Number of Impeller Blades:	23
Inlet Guide Vanes:	NACA 0015
Chord:	12.7 cm (5.0 in.)
Diffuser Guide Vanes:	NACA 4312
Chord:	16.51 cm (6.5 in.)
Diffuser Radius Ratio:	1.46
Rotational Speed:	1795 RPM
Impeller Tip Mach Number:	0.20
Reynolds Number: (based on U_2 , d_2 , and ambient conditions)	$3.2 \cdot 10^7$

ORIGINAL PAGE IS
OF POOR QUALITY

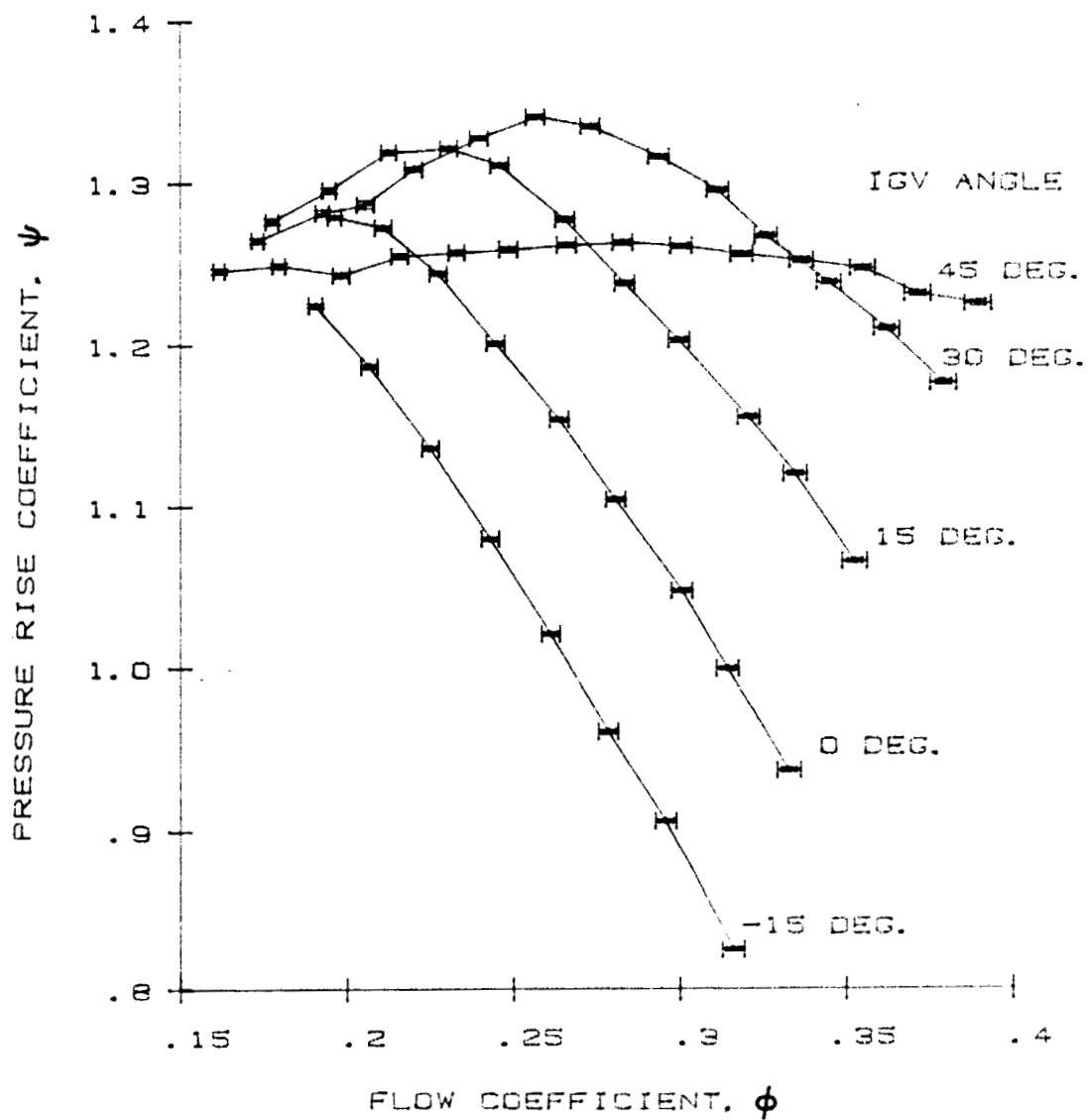


Figure 5.1 Pressure Rise Coefficient Versus Flow Coefficient

ORIGINAL PAGE IS
OF POOR QUALITY

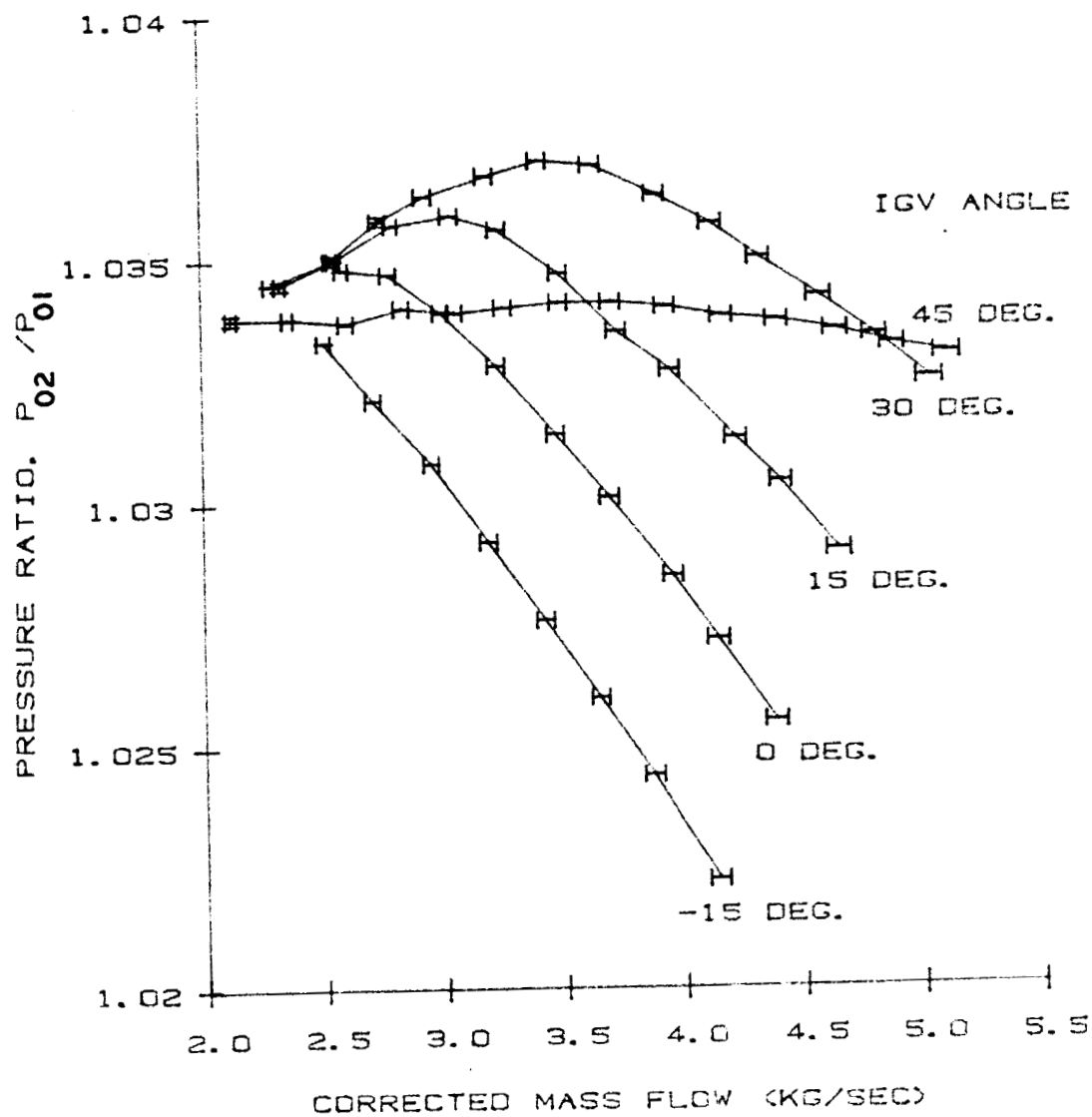


Figure 5.2 Pressure Ratio Versus Corrected Mass Flow

ORIGINAL PAGE IS
OF POOR QUALITY

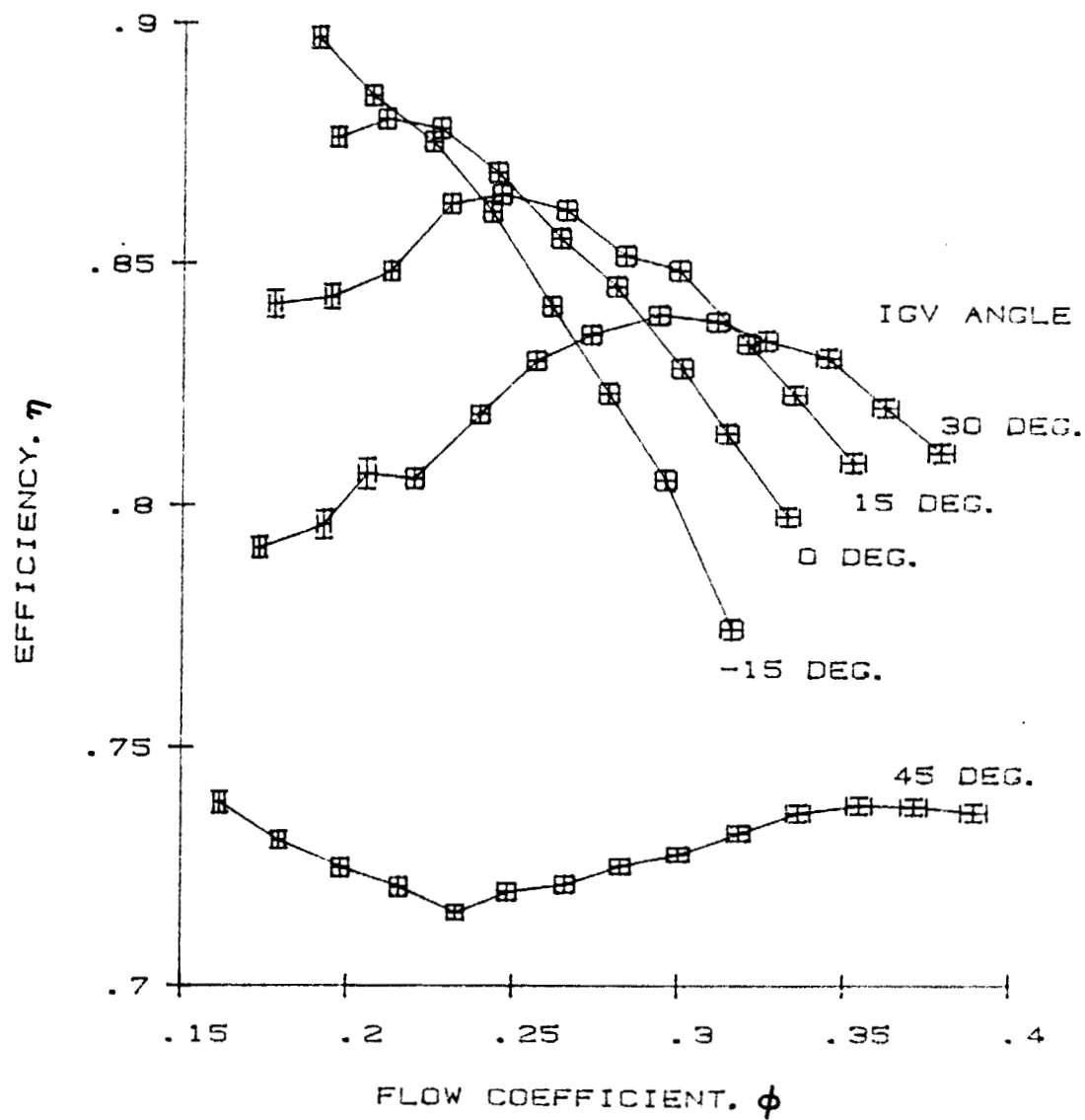


Figure 5.3 Efficiency Versus Flow Coefficient

ORIGINAL PAGE IS
OF POOR QUALITY

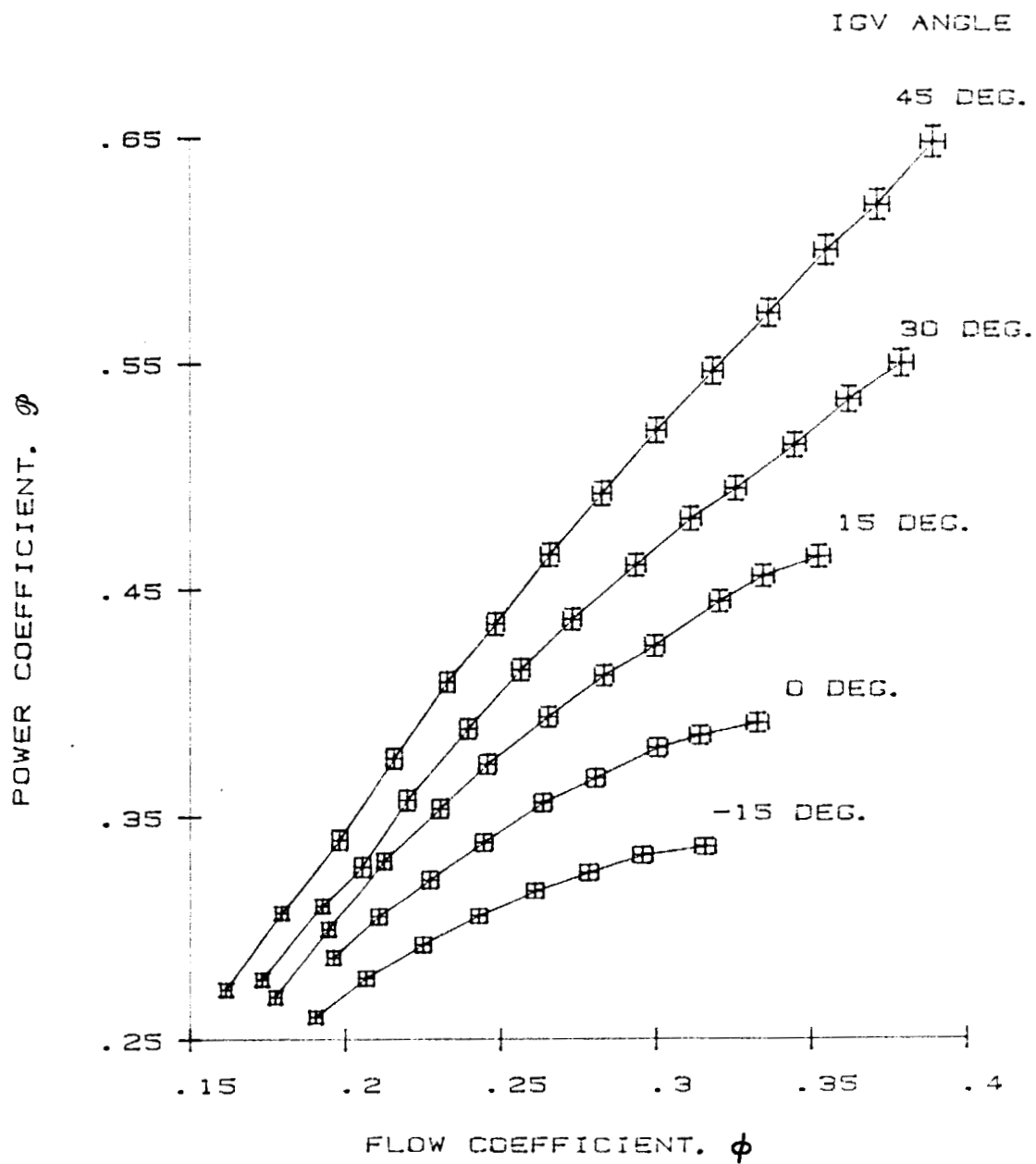


Figure 5.4 Power Coefficient Versus Flow Coefficient

angle is increased. Also, the power coefficient is a monotonically increasing function of the flow coefficient over the range investigated.

This behavior can be explained using the impeller velocity relations shown in Figure 5.5, and the definition of compressor efficiency at constant density as given in Chapter 4.

$$\eta = \frac{(P_{02}-P_{01})/\rho}{U_2 c_{\theta 2} - U_1 c_{\theta 1}} \quad (5.1)$$

In Figure 5.5, c and α refer to the absolute velocity and flow angle, w and β refer to the velocity and flow angle relative to the impeller. Subscripts x , r and θ refer to the axial, radial and tangential components of velocity, respectively. From the velocity relations, it can be seen that,

$$c_{\theta 1} = - \frac{\dot{m}}{\rho_1 A_1} \tan \alpha_1 \quad (5.2)$$

and

$$c_{\theta 2} = U_2 - \frac{\dot{m}}{\rho_2 A_2} \tan \beta_2 \quad (5.3)$$

where the subscripts 1 and 2 denote the inlet and exit of the impeller, respectively, and A is the area at the location given by the subscript.

Substituting Equations 5.2 and 5.3 into Equation 5.1, the impeller pressure rise can be determined.

$$\frac{(P_{02}-P_{01})}{\rho} = \eta \left(\dot{m} \left(\frac{U_1}{\rho_1 A_1} \tan \alpha_1 - \frac{U_2}{\rho_2 A_2} \tan \beta_2 \right) + U_2^2 \right). \quad (5.4)$$

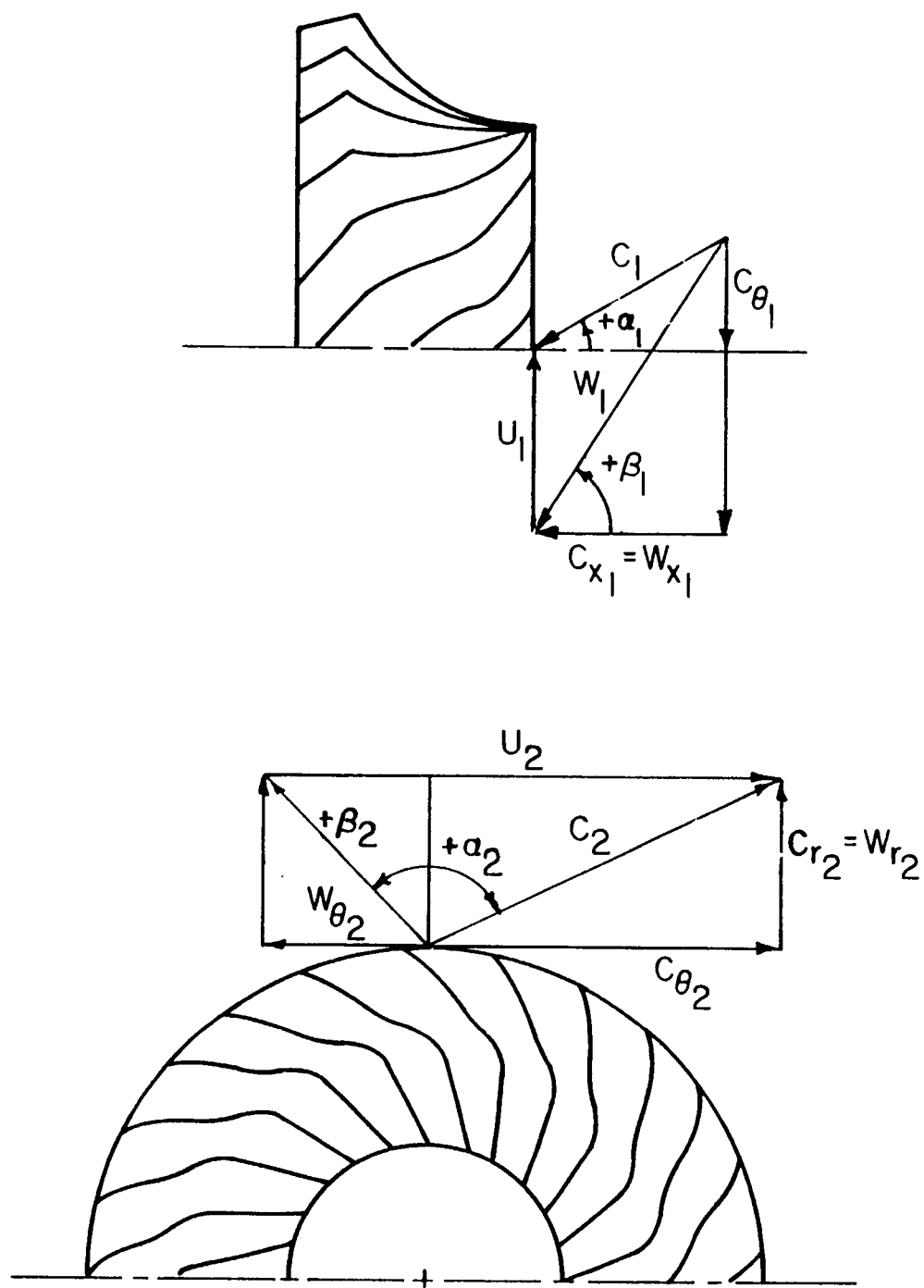


Figure 5.5 Impeller Velocity Relations

Rewriting this equation in terms of the pressure rise and flow coefficients, Equation 5.5, shows that the pressure rise coefficient is dependent on α_1 , ϕ , β_2 , and η ,

$$\Psi = 2\eta\left(\left(\frac{r_1}{r_2}\right)\left(\frac{A_2}{A_1}\right) \tan \alpha_1 - \tan \beta_2\right)\phi + 1 \quad (5.5)$$

where r_1 and r_2 are the mean impeller inlet and exit radii. In this equation, η and β_2 are solely functions of ϕ and α_1 . Thus, Ψ is dependent only on ϕ and α_1 . Since the functional forms $\eta = f(\phi, \alpha_1)$, and $\beta_2 = f(\phi, \alpha_1)$ are not obvious but must be determined experimentally, $\Psi = f(\phi, \alpha_1)$ is best expressed as in Equation 5.5.

The flow angle with respect to radial at the impeller face, α_1 , remained constant over the entire range of flow rates at each setting of the inlet guide vanes. This is due to the conservation of angular momentum which requires that,

$$r_{igv} c_{\theta igv} = r_1 c_{\theta 1} \quad (5.6)$$

where the igv subscripts refer to quantities at the inlet guide vanes and 1 refers to values at the impeller inlet.

Applying Equation 5.2 at the inlet guide vanes and the impeller inlet and substituting into Equation 5.6 yields:

$$\tan \alpha_1 = \left(\frac{r_{igv}}{r_1}\right)\left(\frac{A_1}{A_{igv}}\right) \tan \alpha_{igv} \quad (5.7)$$

This equation shows that the flow angle at the impeller face, α_1 , while not necessarily equal to the inlet guide vane angle, α_{igv} , is independent of flow rate. Thus, the inlet flow angle is only a function of the inlet guide vane angle, α_{igv} .

The angle β_2 is the flow angle with respect to radial at the impeller exit, relative to the impeller, seen in Figure 5.5. This angle was not constant over the range of flow rates but was found to vary from 53° to 70° , and to decrease with increasing flow rate. Thus, the exit flow receives less than perfect guidance from the impeller blades. This is accounted for by means of the slip factor which is defined as $\sigma = \frac{c_{\theta 2}}{c_{\theta 2}'}$, where $c_{\theta 2}'$ is the absolute tangential flow velocity at the impeller exit based on the blade angle, and $c_{\theta 2}$ is the actual absolute tangential flow velocity [1]. The angle β_2 was found to be only a weak a function of inlet guide vane angle.

The observed compressor performance can now be explained using Equation 5.5, and by considering how the four parameters in the equation vary. It should be noted that ϕ and α_1 vary over a much greater range than η and β_2 . The variation in inlet flow angle, α_1 , with varying inlet guide vane angle, α_{igv} , is given in Table 5.2. The variation in flow coefficient, ϕ , was between 0.15 and 0.40. The efficiency, η , varied slightly from 0.7 to 0.9 and the variation in impeller relative exit flow angle was 17° (53° to 70°).

Equation 11 can be viewed as a line in the Ψ - ϕ plane with Ψ -intercept 2η and slope given by:

$$2\eta \left(\left(\frac{r_1}{r_2} \right) \left(\frac{A_2}{A_1} \right) \tan \alpha_1 - \tan \beta_2 \right). \quad (5.8)$$

At higher flowrates, β_2 is close to the blade exit angle β_2' , and a weak function of ϕ .

Table 5.2 Inlet Swirl Angle Versus Inlet Guide Vane Angle

α_{igv}	α_1
-15°	-23°
0°	-1°
15°	21°
30°	39°
45°	57°

Thus, the slope changes little with flowrate since α_1 is not dependent on ϕ and the change of η with ϕ is small. The slope of the Ψ – ϕ curves in this linear portion is dominated by the blade exit angle, β_2' , being slightly influenced by variations in α_1 . The slight curve downward in this region is due to the small change of β_2 with ϕ . At lower values of ϕ , as ϕ decreases, β_2 increases due to the slip velocity [7] and the efficiency, η , decreases, thus resulting in the peaks seen in Figure 5.1.

The efficiency is highly dependent upon the interaction of the inlet flow field and inlet of the impeller. For optimum performance, the flow should enter the impeller at an angle close to that of the impeller blades. Because this relative velocity angle, β_1 , varies with flow rate, an optimum inlet condition only occurs over a small range of flow rates. At conditions other than optimum, a positive or negative incidence angle between the flow and the impeller blades occurs. The resulting flow conditions are detrimental to performance. This can be quantified by considering the relative inlet flow angle,

$$\beta_1 = \tan^{-1}\left(\tan \alpha_1 + \frac{U_1 \rho_1 A_1}{\dot{m}}\right) \quad (5.9)$$

It can be seen that a positive incidence angle between the flow and the impeller inlet occurs at low flow rates and this angle decreases as the flow rate increases. It is also noted that at any particular flow rate, the incidence angle increases as α_1 increases. However, the range over which the incidence angle varies decreases.

It was noted previously that α_1 was invariant with flow rate. However, there will be a variation in α_1 with radius, due to the conservation of angular momentum. This variation tends to decrease α_1 at the blade tip and increase it at the hub. This is discussed in Appendix B.

It can be seen that a variation in the relative incidence angle at the impeller face occurs due to the variation in the absolute flow angle and the variation in the inlet wheel speed. In the Research Compressor Facility, the inlet tip wheel speed is nearly twice the inlet hub speed. The variation in wheel speed increases the incidence angle at the impeller blade tip in relation to the hub incidence angle. The variation in absolute flow angle, however, has the opposite effect with the variation in wheel speed having a greater effect on the incidence angle.

As the flow rate is decreased, the relative incidence angle increases. Eventually, the machine reaches a point where the flow cannot enter the impeller smoothly and flow separation occurs on the suction surface of the impeller blades. As the flow rate continues to decrease, stall cells begin to form which rotate with the impeller. This condition is known as rotating stall and with it comes a degradation in the

performance. The stalling of the impeller blades is the cause for the peaks in the pressure curves. Once the machine begins to stall, the impeller loses its ability to produce a rise in pressure and the pressure rise and efficiency begin to decrease. As stated above, increasing the inlet guide vane angle increases the relative incidence angle at the impeller face. Therefore, stall occurs at higher flow rates as the inlet guide vane angle is increased. This explains the shift in pressure curve peaks toward higher flow rates as the inlet guide vane angle is increased. At low flow rates, the variation in efficiency has a greater effect on the pressure curve slope than does the range of specific power input. At higher flow rates, the converse is true.

From Figure 5.3, it is evident that the maximum efficiency on a particular curve decreases as the inlet guide vane angle increases, and that the flow rate for maximum efficiency does not necessarily correspond to the flow rate for maximum pressure rise. Because the denominator in the efficiency definition, Equation 5.1, represents the specific power imparted to the fluid, and since this value is constantly decreasing with increasing ϕ , the maximum value of efficiency does not necessarily occur at the same flow rate as the value of maximum pressure rise. The maximum efficiency cannot, however, occur at a lower flow rate than that of maximum Ψ . Furthermore, because the maximum value of efficiency occurs at greater flow rates as the inlet guide vane angle is increased, the velocities and thus the losses in the impeller are higher and cause the maximum value of efficiency to be lower than for smaller values of inlet guide vane angle.

As the flow rate is increased, the relative incidence angle decreases, reaching a point where it becomes negative. Under the conditions of the current investigation, negative incidence angles only occur at low inlet guide vane angles and high values of ϕ . A degradation in performance due to negative incidence is not evident from the pressure rise curves but its effect can be observed by the decrease in efficiency at high flow rates.

The power coefficient, \mathcal{P} , was defined in Chapter 4. \mathcal{P} can be expressed as

$$\mathcal{P} = \frac{\Psi\phi}{\eta} \quad (5.10)$$

and, using Equation 5.5, can be written as follows.

$$\mathcal{P} = 2\left(\left(\frac{r_1}{r_2}\right)\left(\frac{A_2}{A_1}\right) \tan \alpha_1 - \tan \beta_2\right)\phi^2 + \phi \quad (5.11)$$

This equation predicts a maximum in power at a certain value of ϕ . This value, however, is beyond the range of ϕ considered in this investigation. For the regions of interest, \mathcal{P} is a monotonically increasing function of ϕ .

Impeller Static Pressure Distribution

The static pressure distributions on the impeller surface were measured on three streamlines at five normal locations on both the pressure surface and the suction surface of the impeller blades. These are presented in Figures 5.6 through 5.25 in the form of the static pressure coefficient on the pressure and suction surfaces of the impeller versus the tap radius referred to the impeller radius, r/r_2 . The impeller inlet incidence angles for the hub, mean and tip are given in Tables B1

ORIGINAL PAGE IS
OF POOR QUALITY

IGV ANGLE = -15.0 DEG.
FLOW COEFFICIENT = 0.132

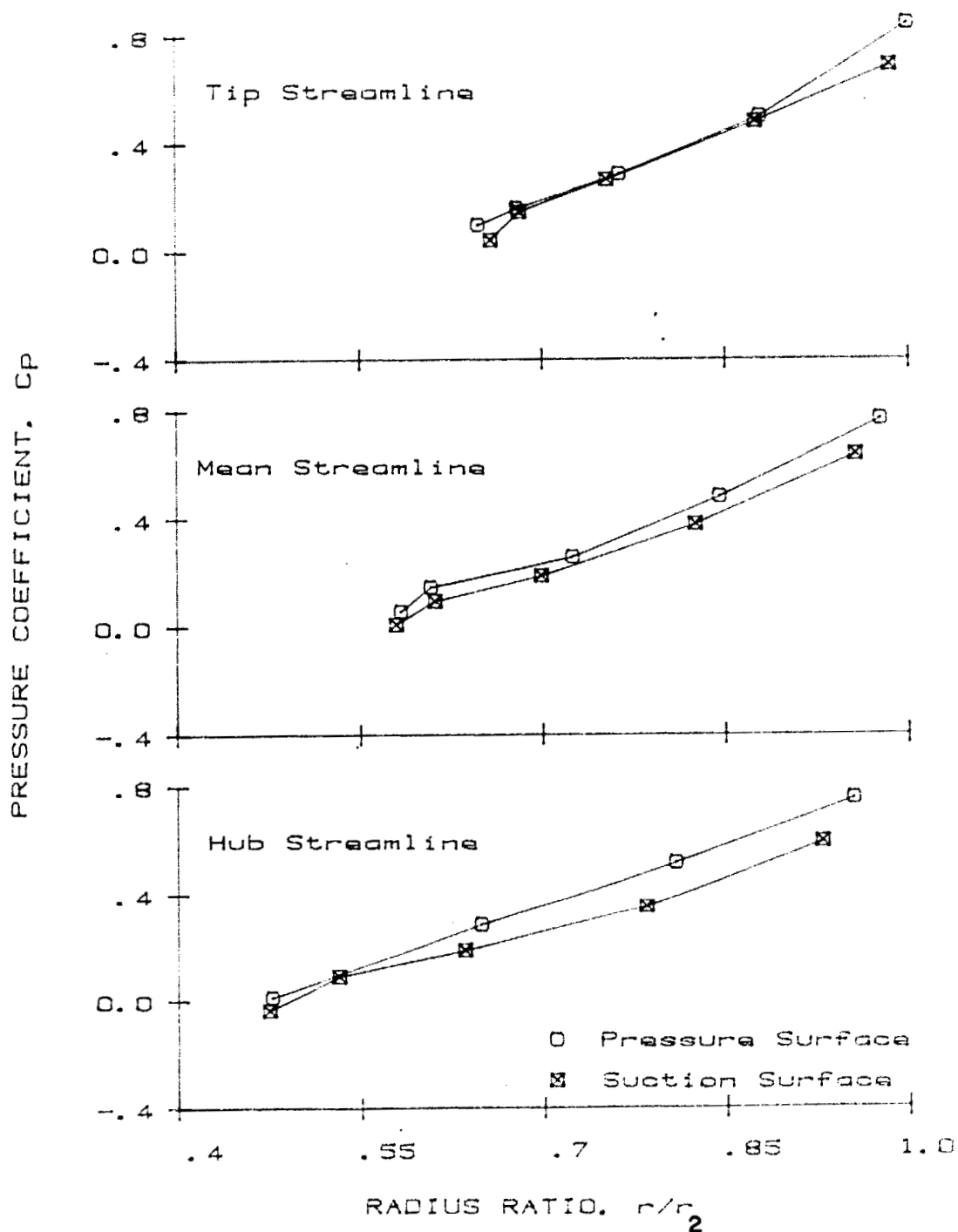


Figure 5.6 Impeller Blade Static Pressure Distribution (IGV Angle = -15° , $\phi = 0.132$)

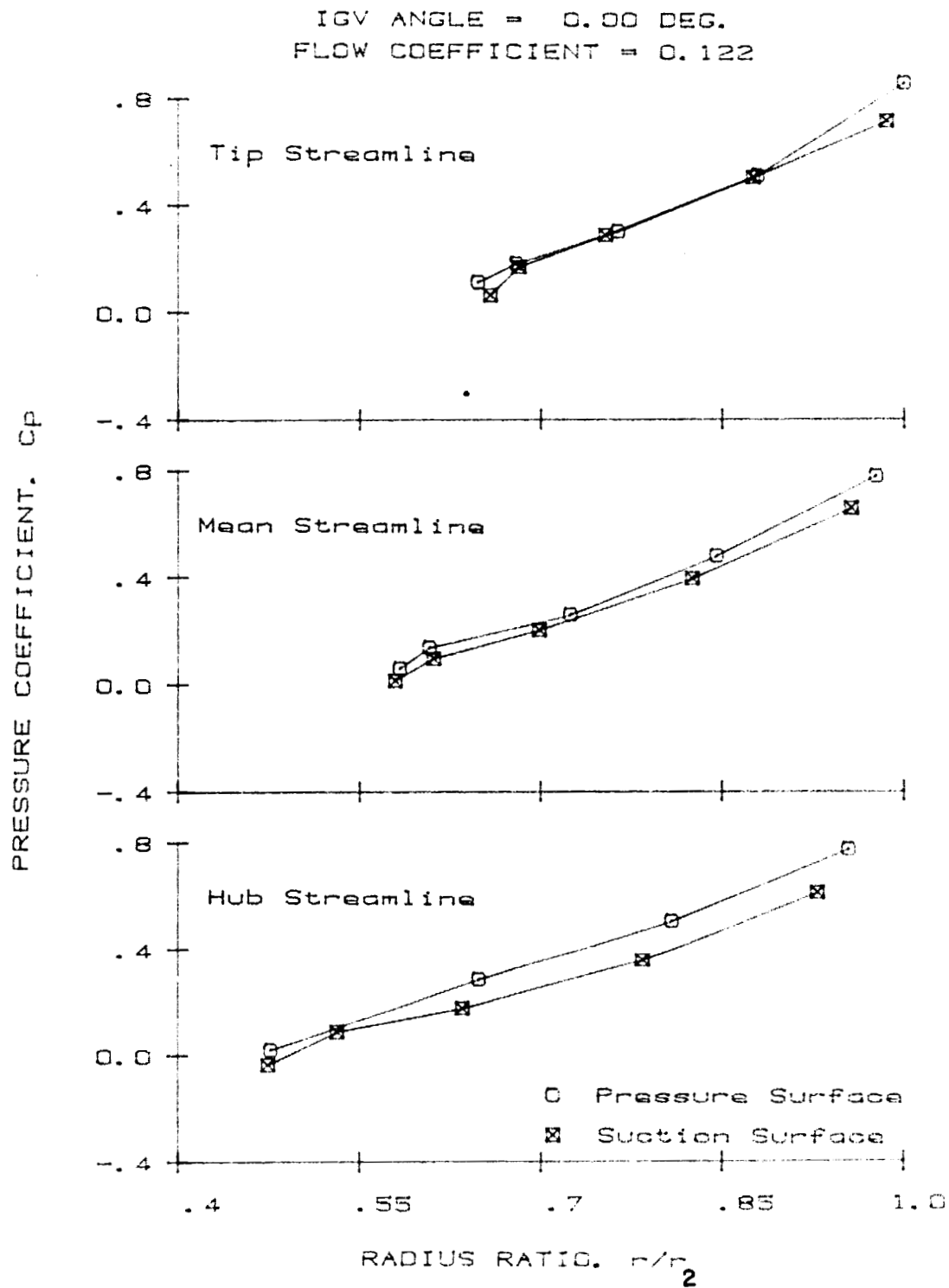


Figure 5.7 Impeller Blade Static Pressure Distribution (IGV Angle = 0°, $\phi = 0.122$)

ORIGINAL PAGE IS
OF POOR QUALITY

IGV ANGLE = 15.00 DEG.
FLOW COEFFICIENT = 0.125

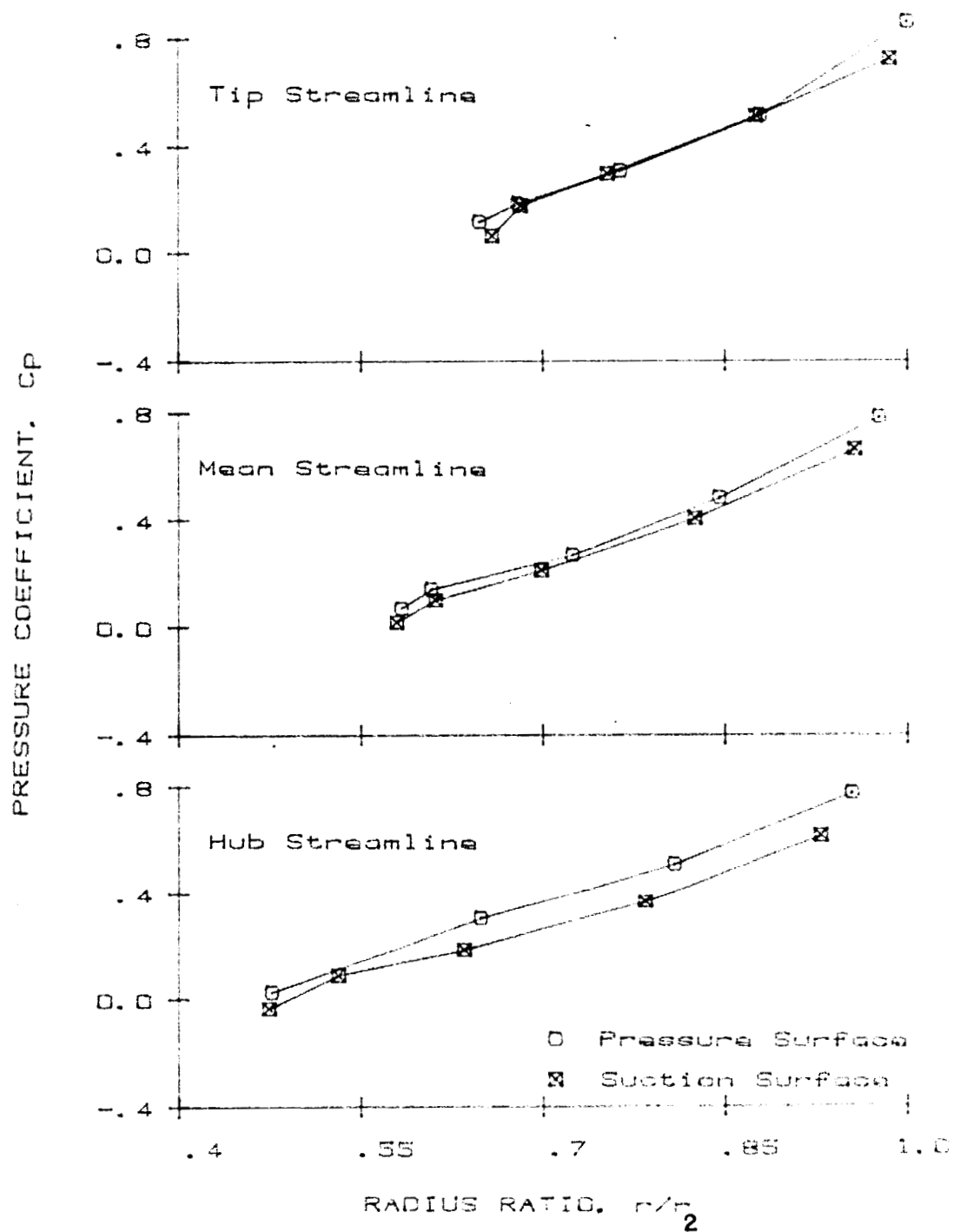


Figure 5.8 Impeller Blade Static Pressure Distribution (IGV Angle = 15°, $\phi = 0.125$)

ORIGINAL PAGE IS
OF POOR QUALITY

IGV ANGLE = 30.00 DEG.
FLOW COEFFICIENT = 0.127

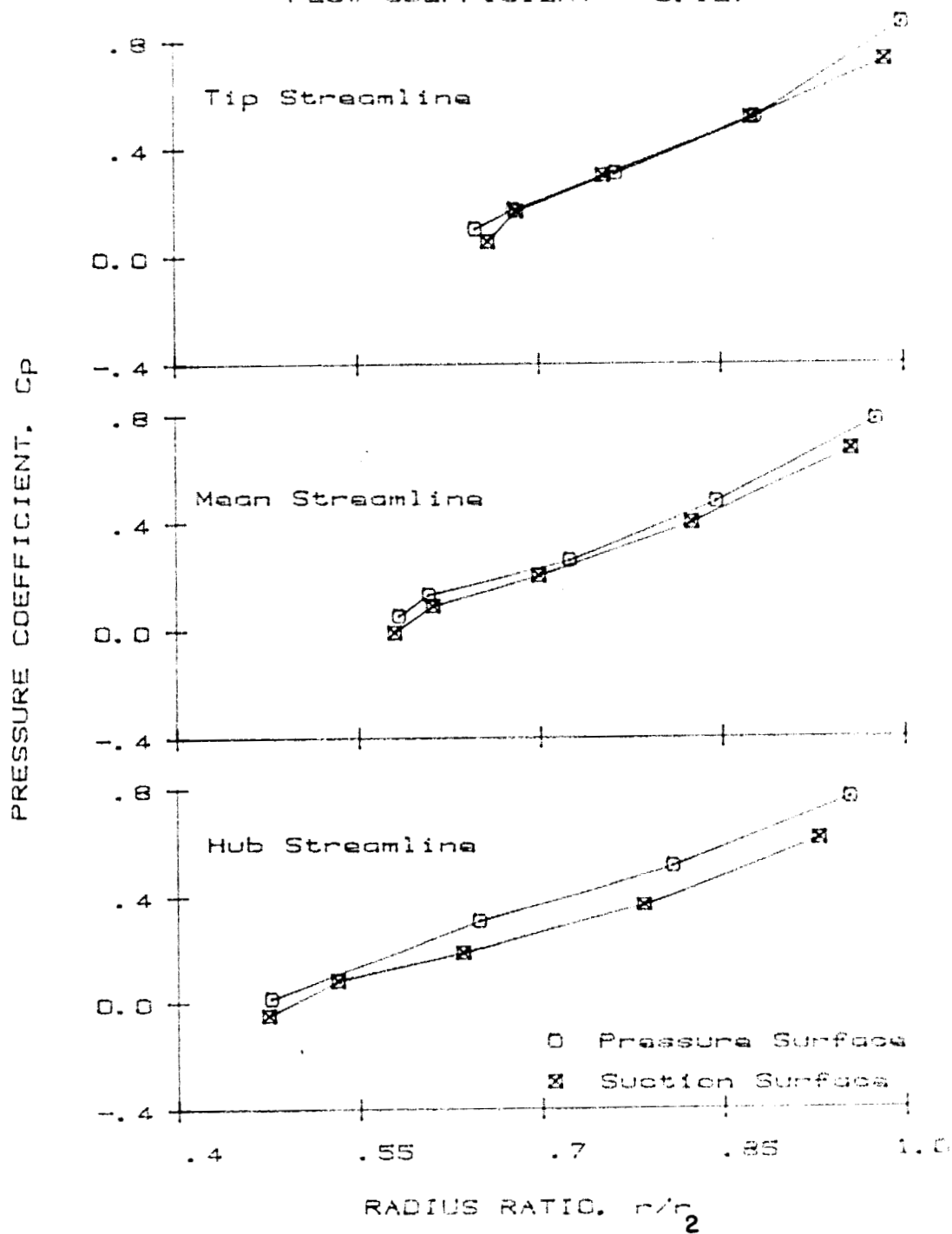


Figure 5.9 Impeller Blade Static Pressure Distribution (IGV Angle = 30° , $\phi = 0.127$)

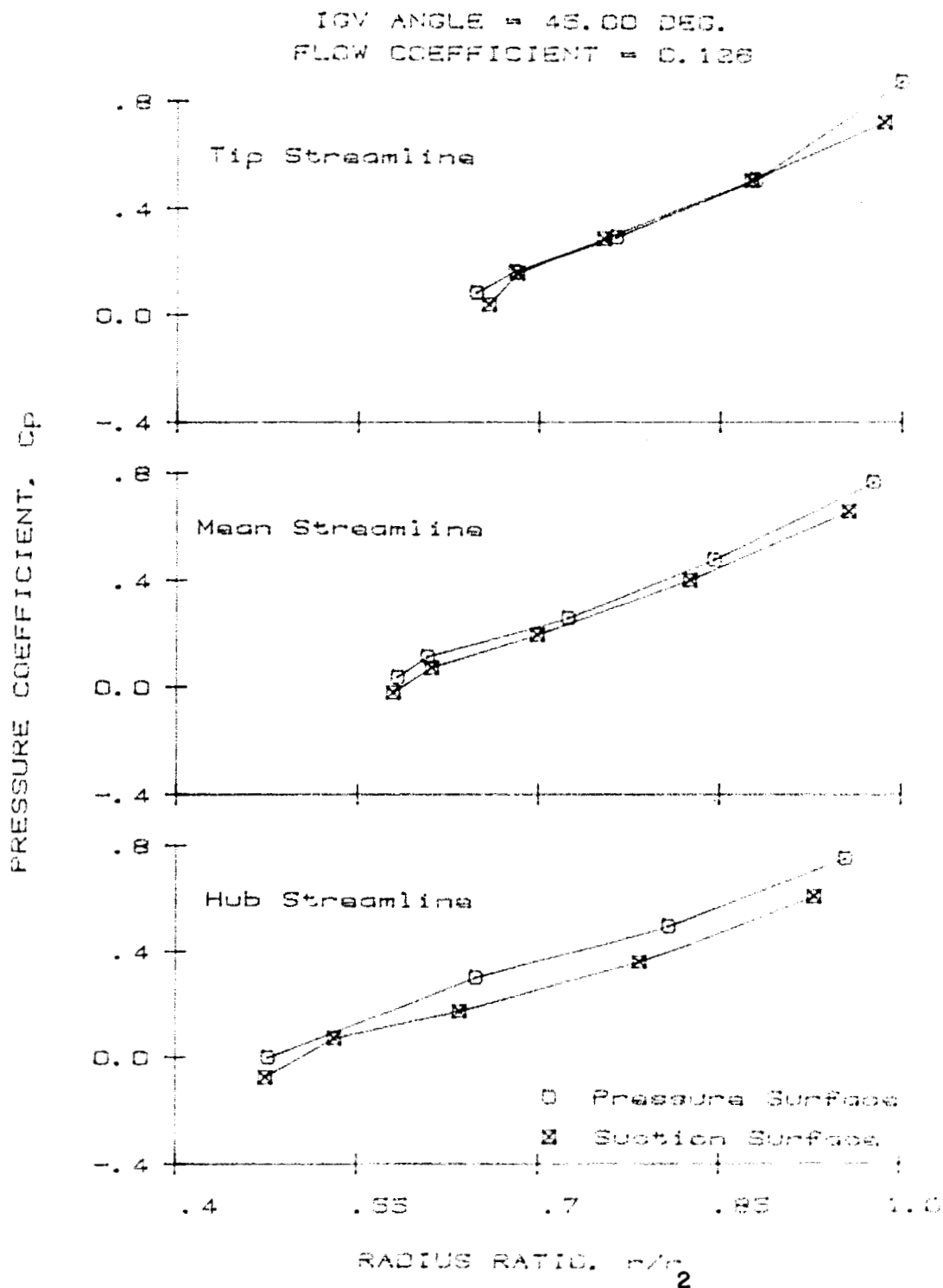


Figure 5.10 Impeller Blade Static Pressure Distribution (IGV Angle = 45°, $\phi = 0.126$)

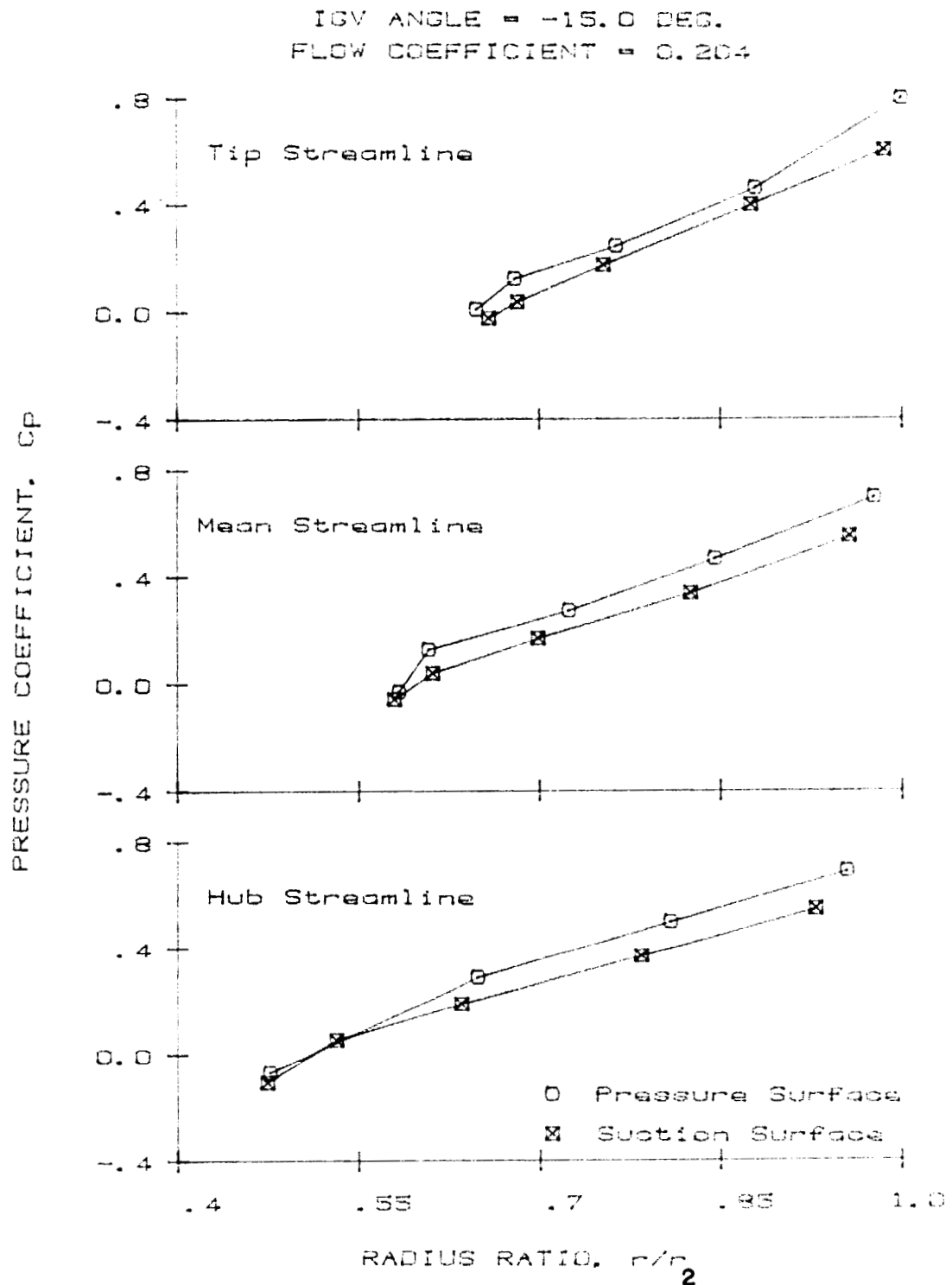


Figure 5.11 Impeller Blade Static Pressure Distribution (IGV Angle = -15° , $\phi = 0.204$)

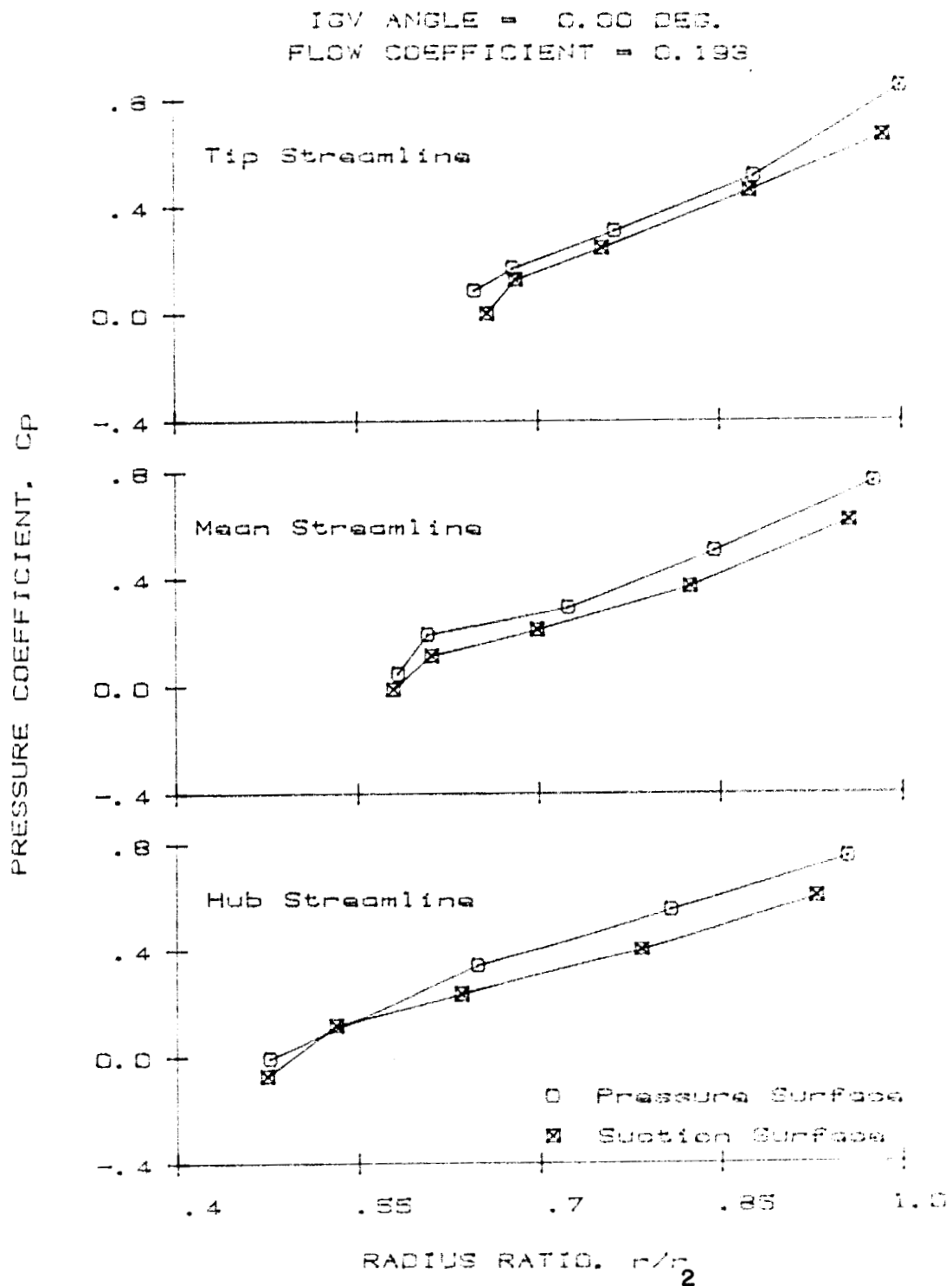


Figure 5.12 Impeller Blade Static Pressure Distribution (IGV Angle = 0° , $\phi = 0.193$)

0.2

ORIGINAL PAGE IS
OF POOR QUALITY

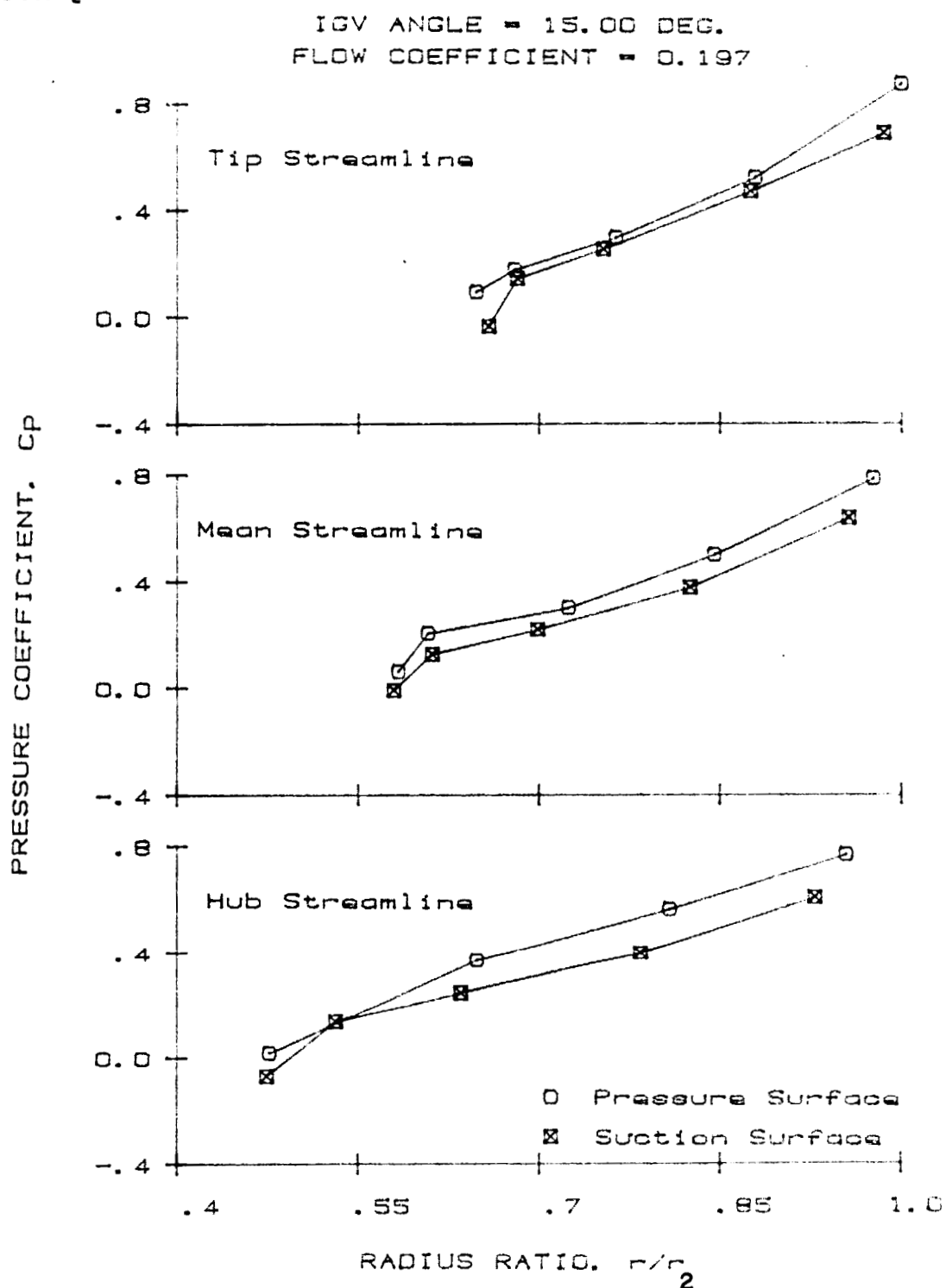


Figure 5.13 Impeller Blade Static Pressure Distribution (IGV Angle = 15°, $\phi = 0.197$)

ORIGINAL PAGE IS
OF POOR QUALITY

IGV ANGLE = 30.00 DEG.
FLOW COEFFICIENT = 0.196

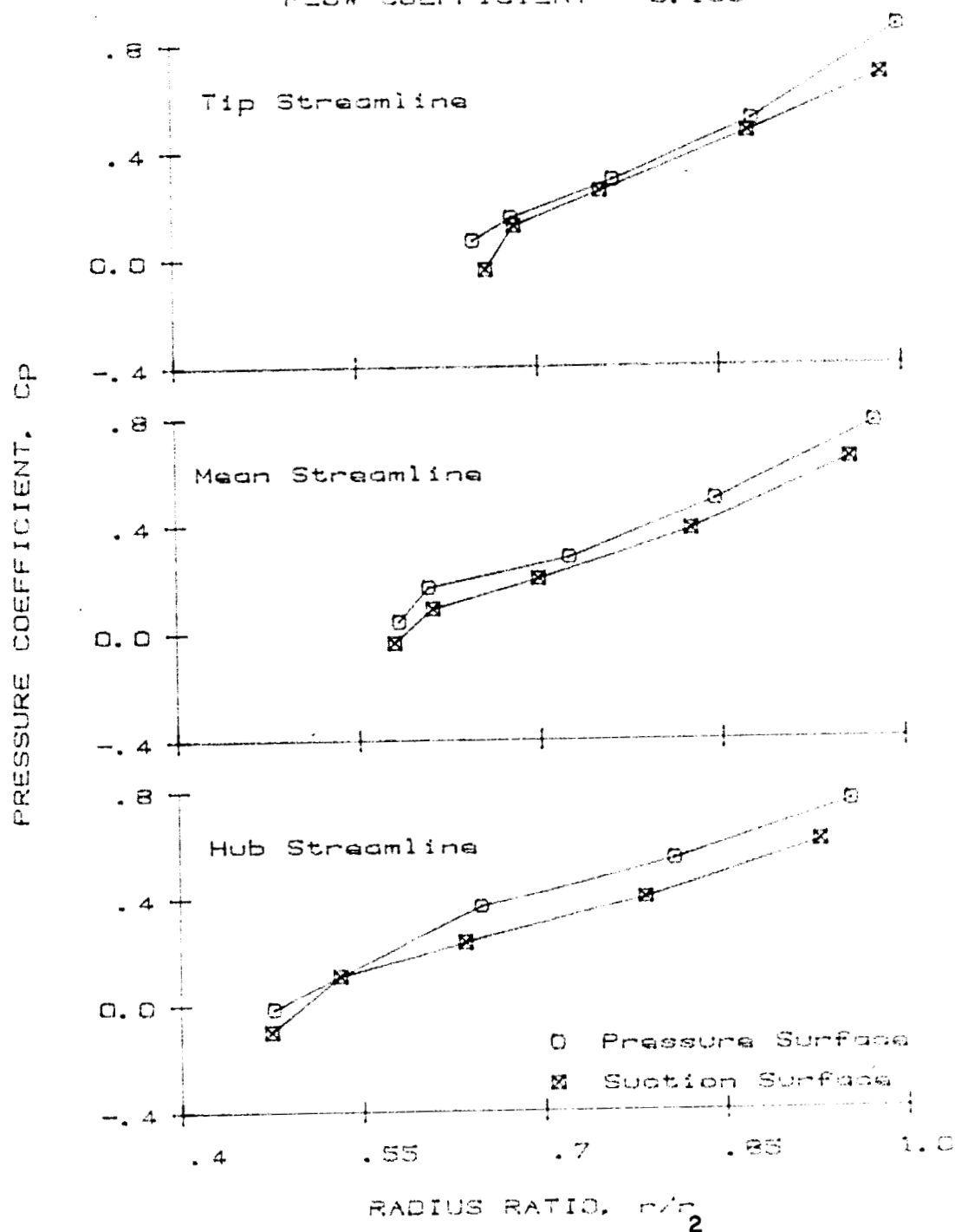


Figure 5.14 Impeller Blade Static Pressure Distribution (IGV Angle = 30°, $\phi = 0.196$)

ORIGINAL PAGE IS
OF POOR QUALITY

IGV ANGLE = 45.00 DEG.
FLOW COEFFICIENT = 0.197

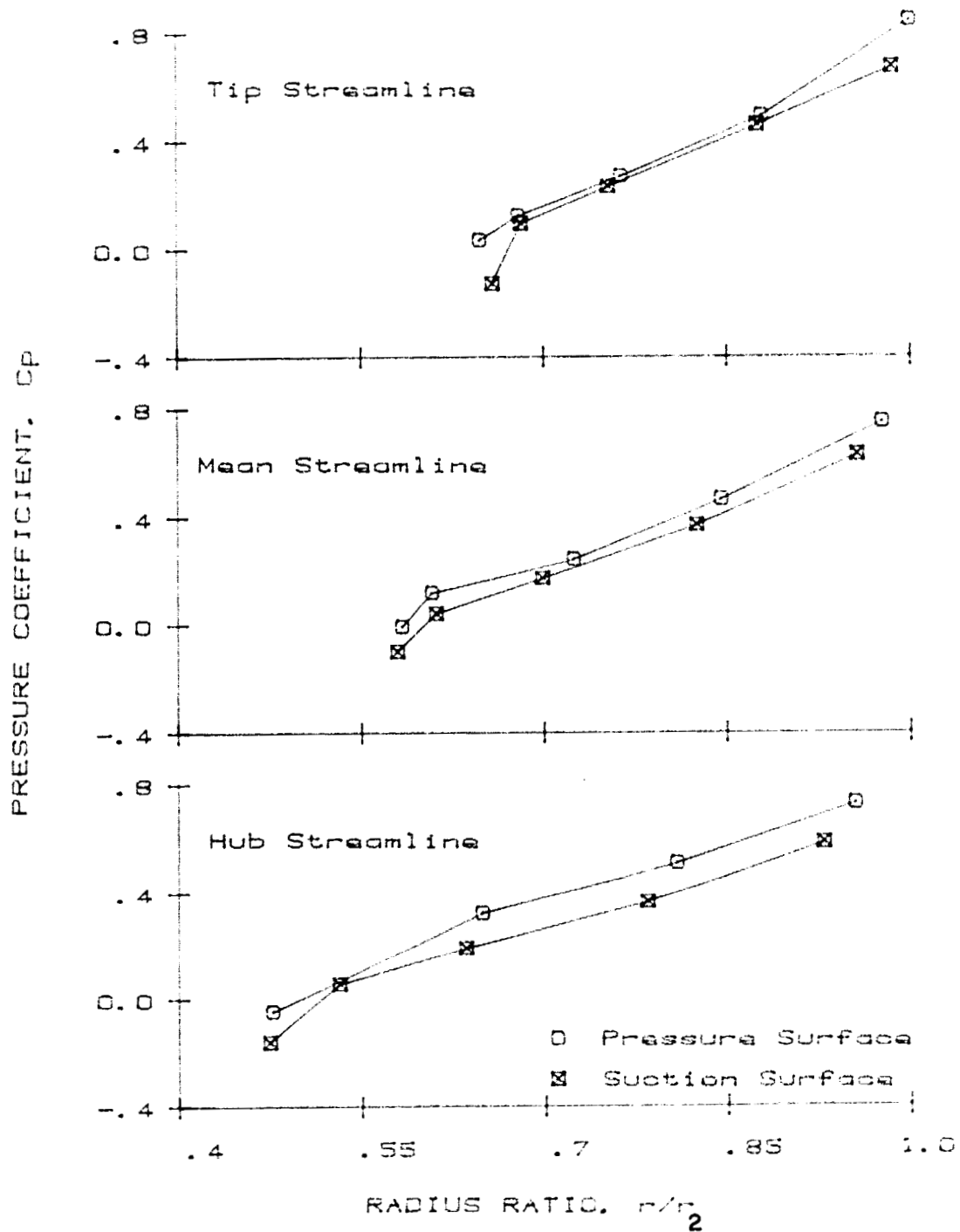


Figure 5.15 Impeller Blade Static Pressure Distribution (IGV Angle = 45°, $\phi = 0.197$)

IGV ANGLE = -15.0 DEG.
FLOW COEFFICIENT = 0.258

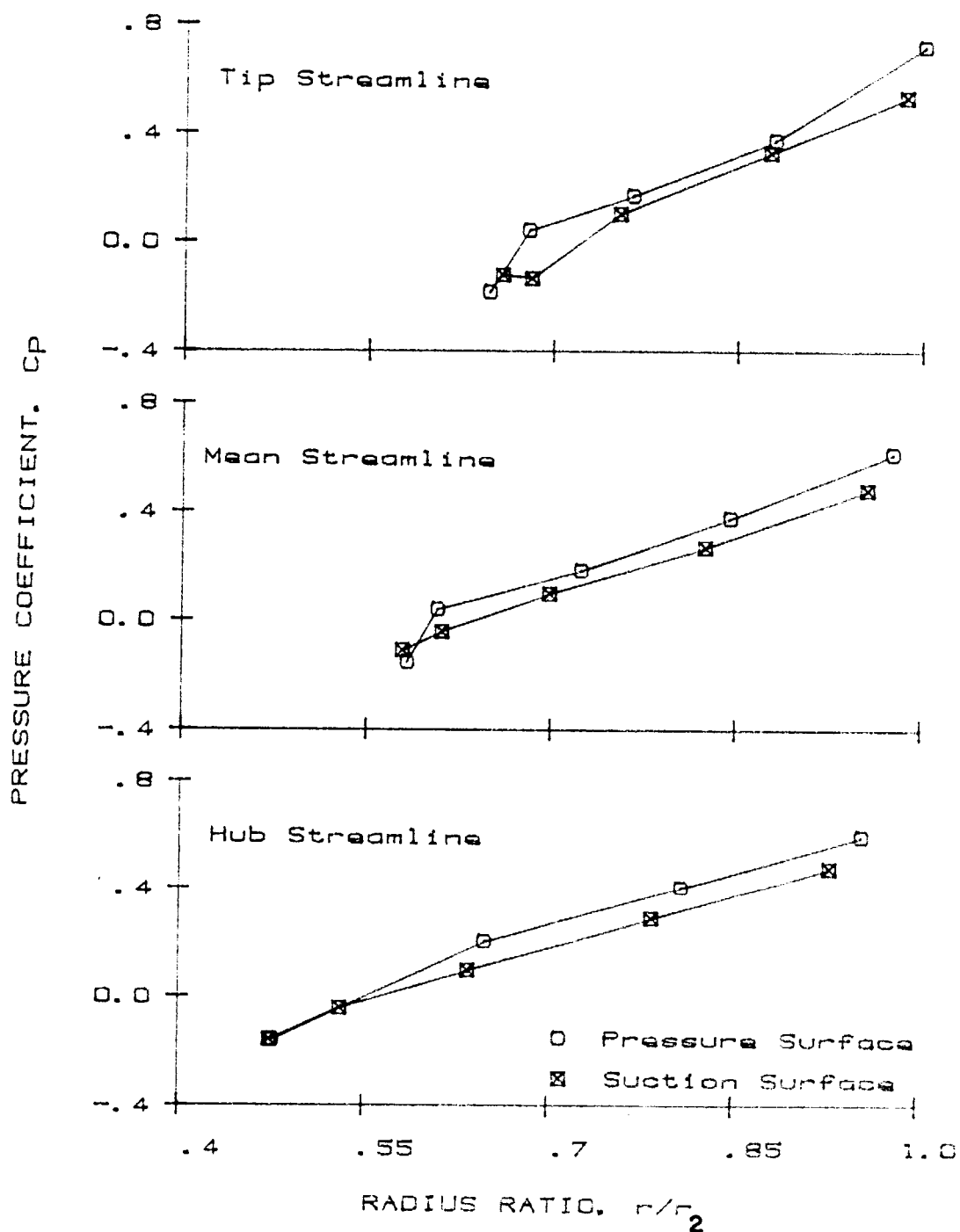


Figure 5.16 Impeller Blade Static Pressure Distribution (IGV Angle = -15° , $\phi = 0.258$)

ORIGINAL PAGE IS
OF POOR QUALITY

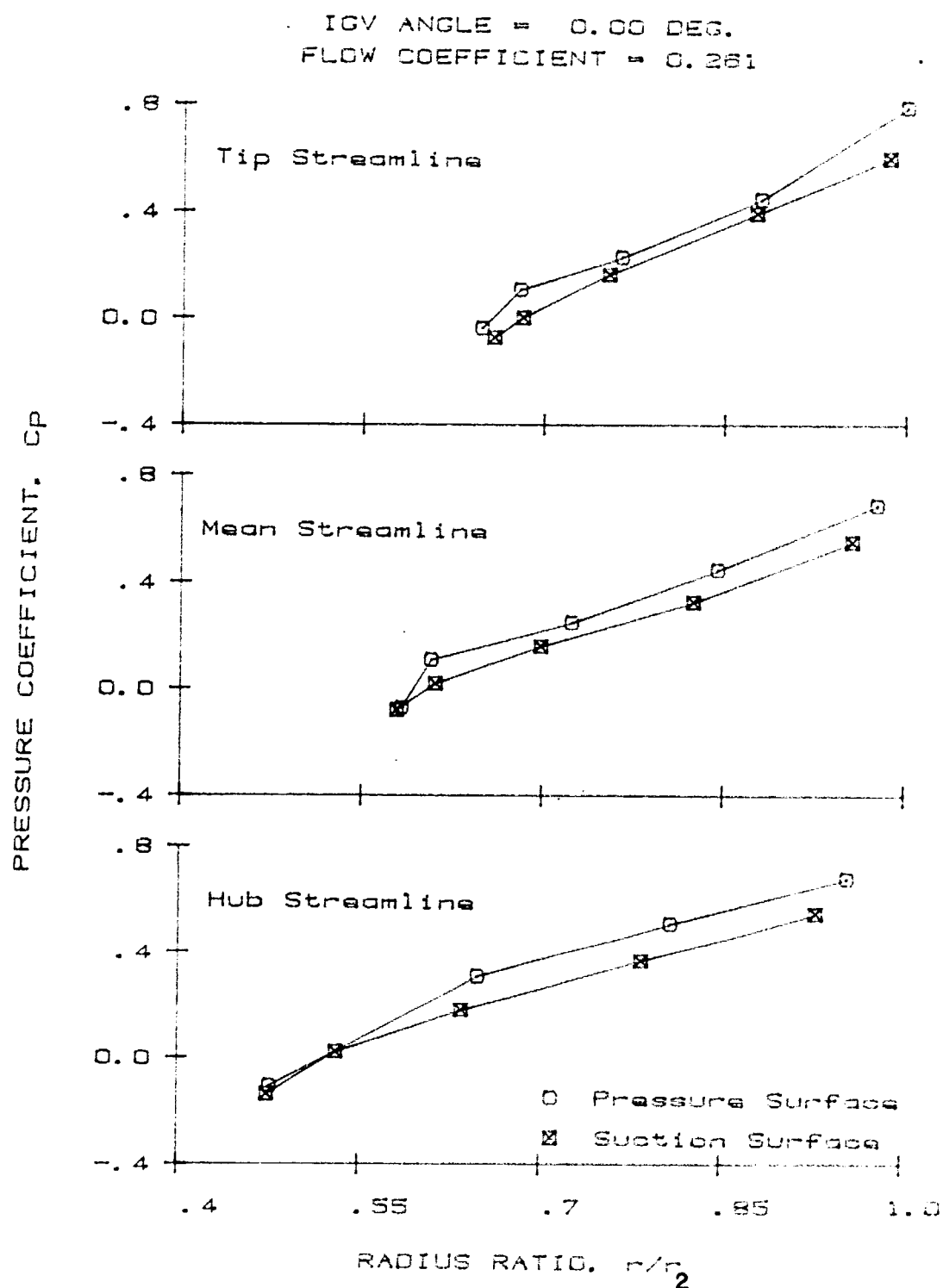


Figure 5.17 Impeller Blade Static Pressure Distribution (IGV Angle = 0°, $\phi = 0.261$)

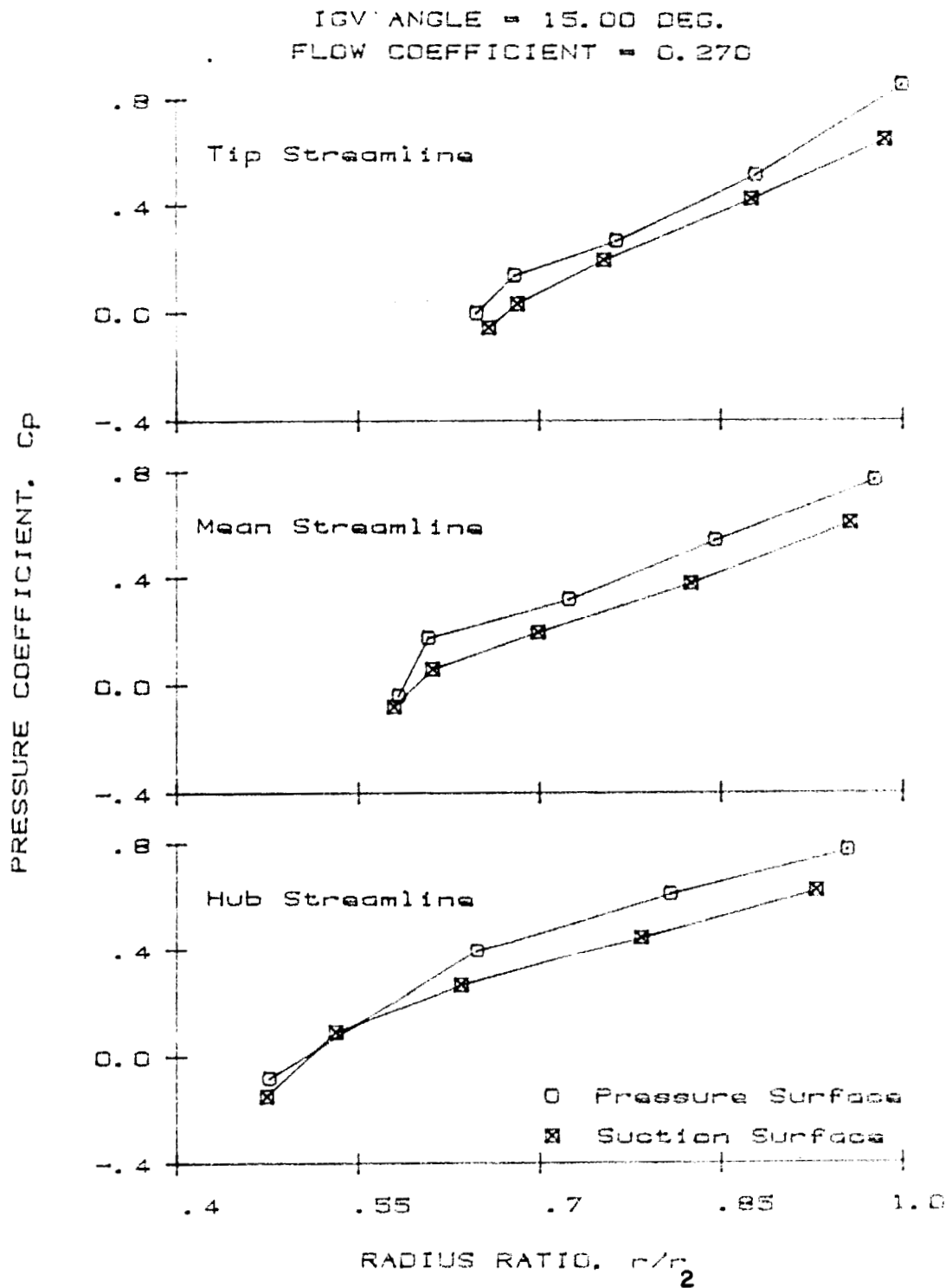


Figure 5.18 Impeller Blade Static Pressure Distribution (IGV Angle = 15°, $\phi = 0.270$)

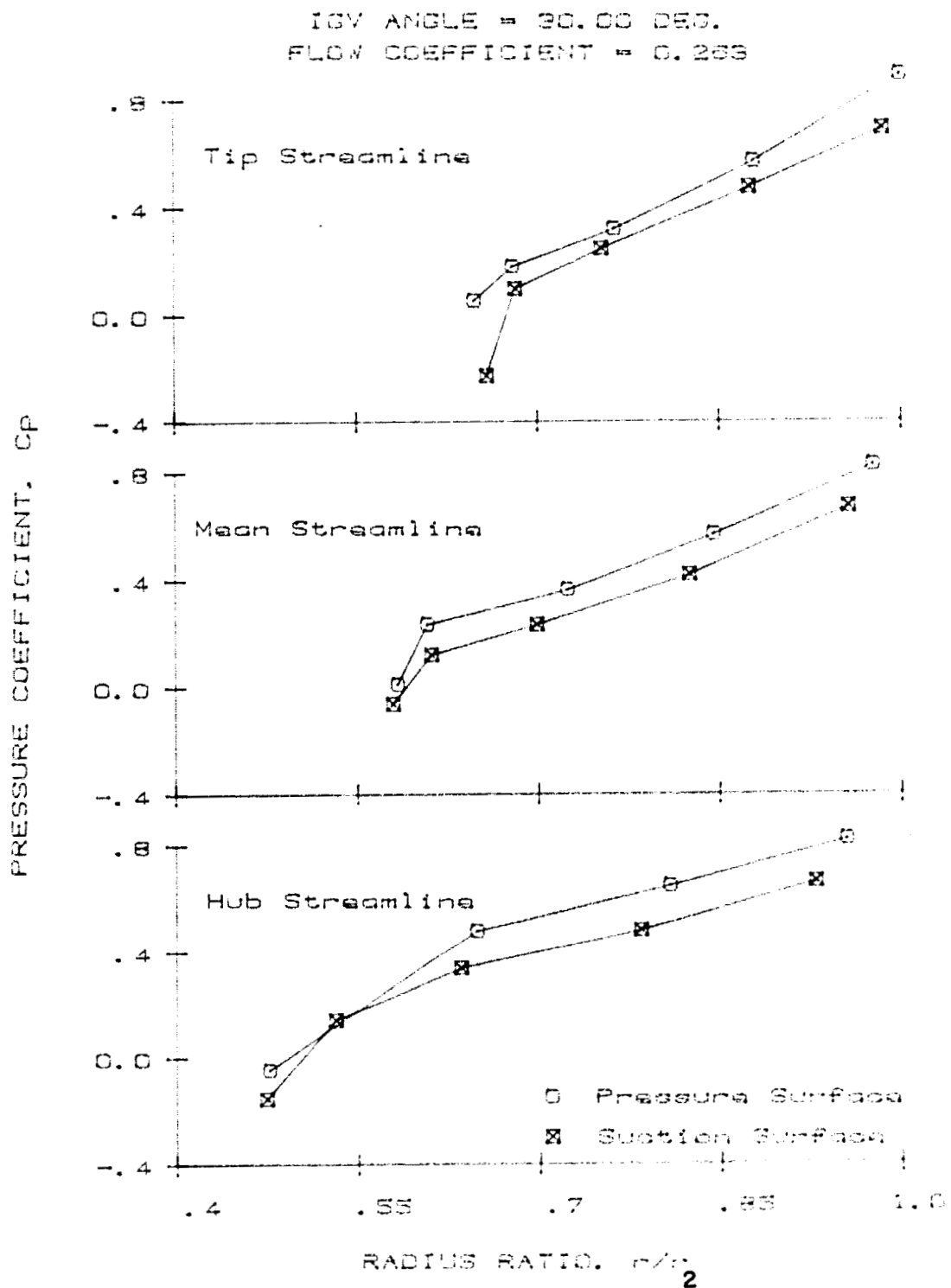


Figure 5.19 Impeller Blade Static Pressure Distribution (IGV Angle = 30° , $\phi = 0.263$)

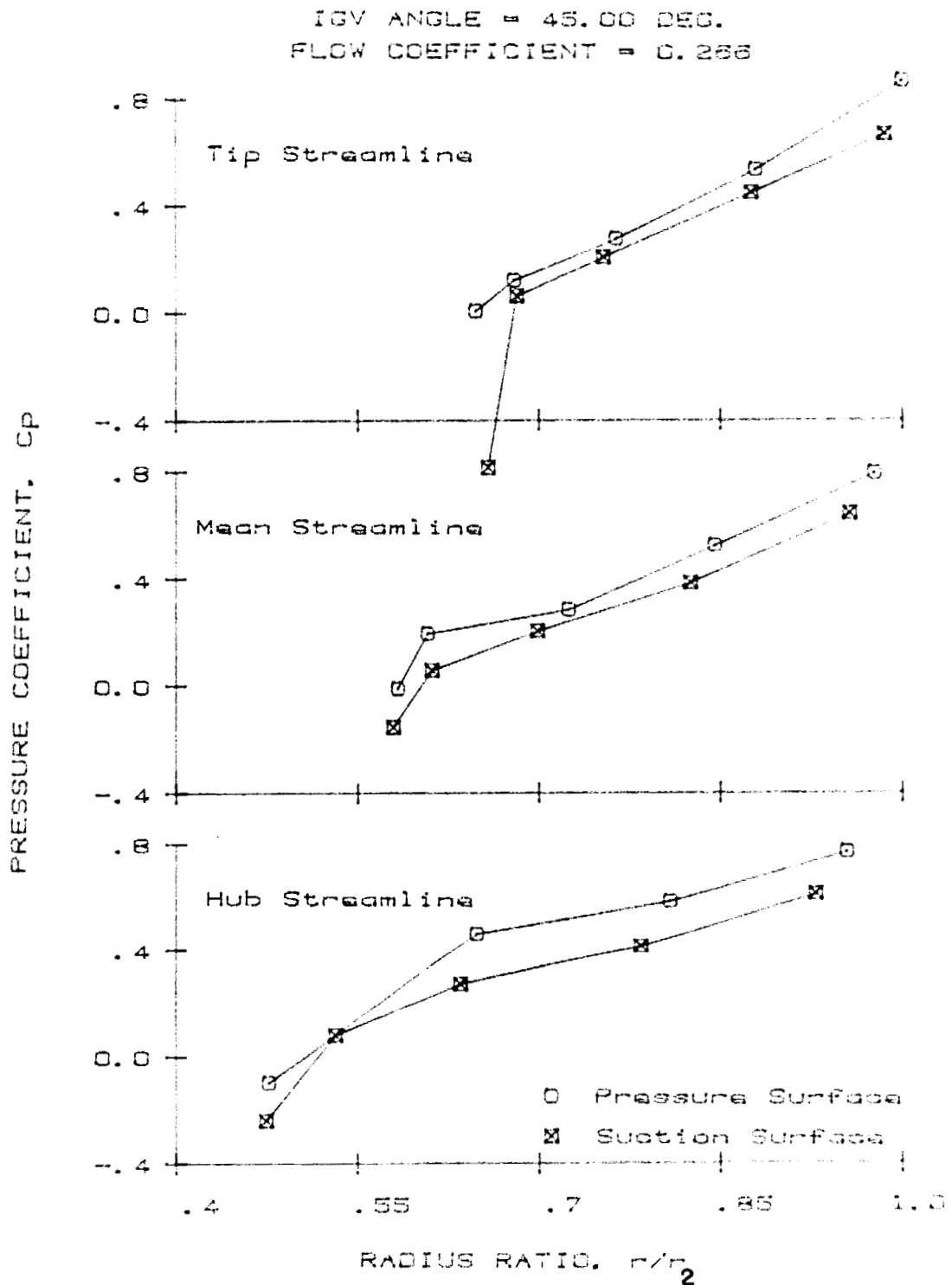


Figure 5.20 Impeller Blade Static Pressure Distribution (IGV Angle = 45°, $\phi = 0.266$)

IGV ANGLE = -15.0 DEG.
FLOW COEFFICIENT = 0.313

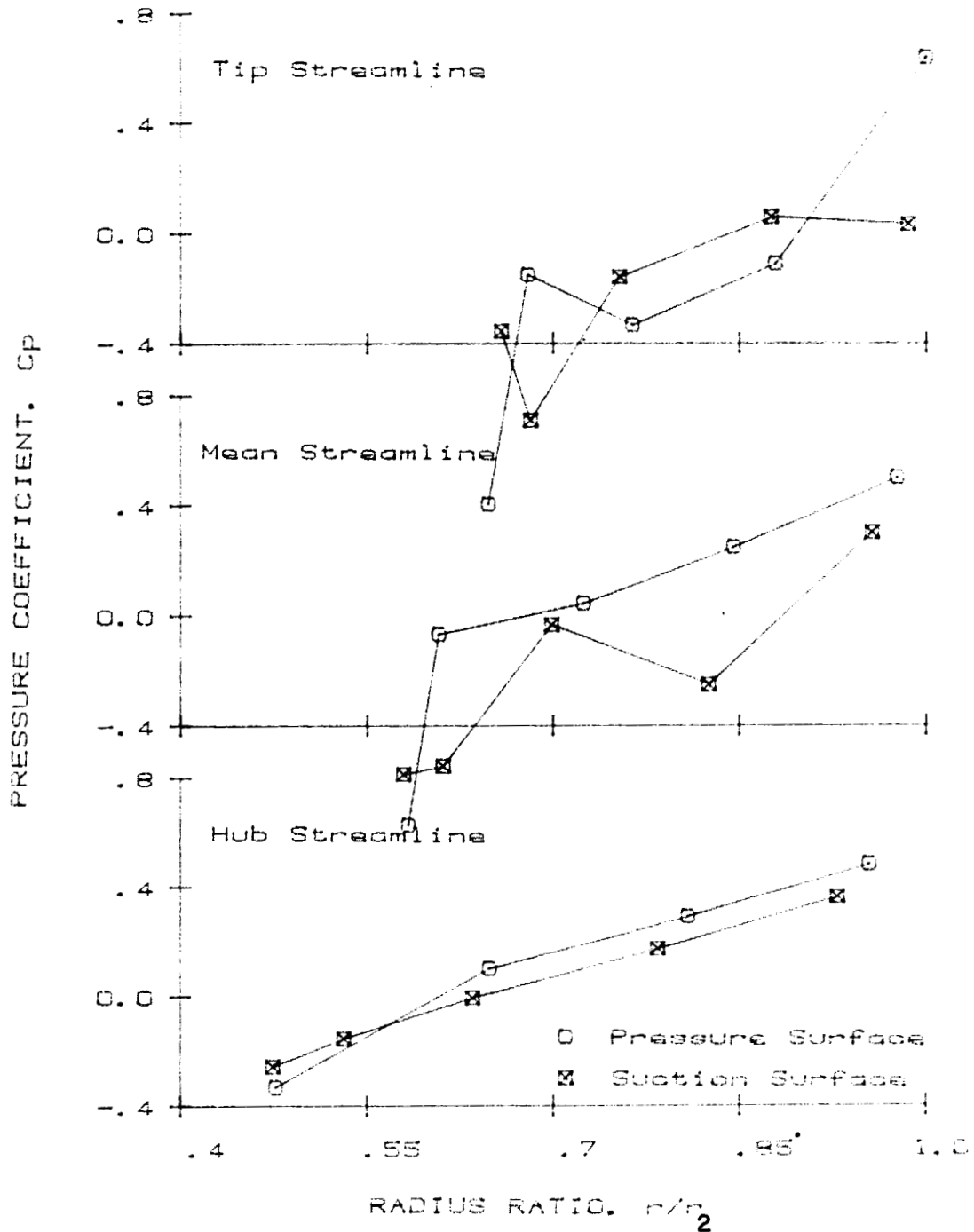


Figure 5.21 Impeller Blade Static Pressure Distribution (IGV Angle = -15° , $\phi = 0.313$)

ORIGINAL PAGE IS
OF POOR QUALITY

IGV ANGLE = 0.00 DEG.
FLOW COEFFICIENT = 0.313

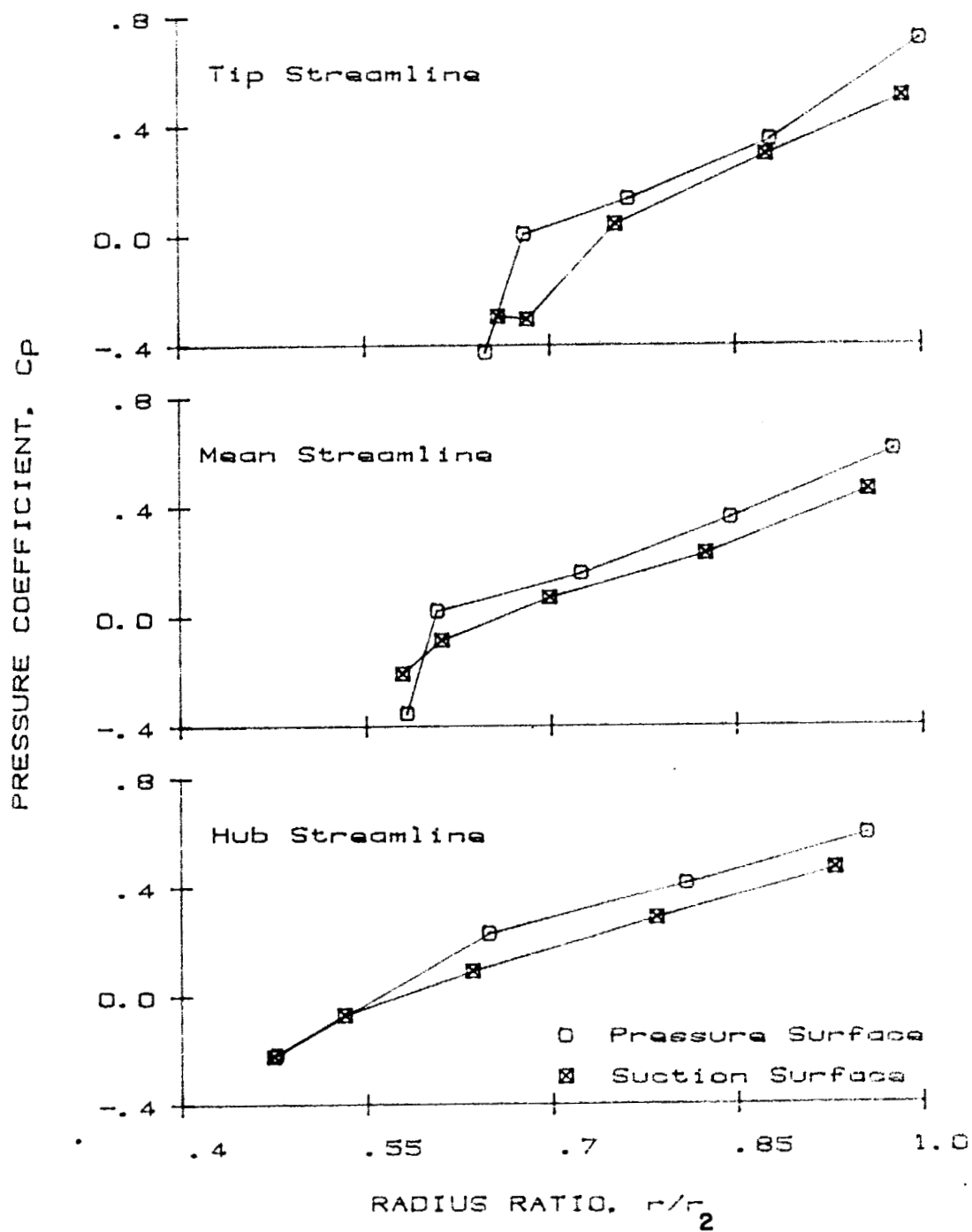


Figure 5.22 Impeller Blade Static Pressure Distribution (IGV Angle = 0°, $\phi = 0.313$)

ORIGINAL PAGE IS
OF POOR QUALITY

IGV ANGLE = 15.00 DEG.
FLOW COEFFICIENT = 0.325

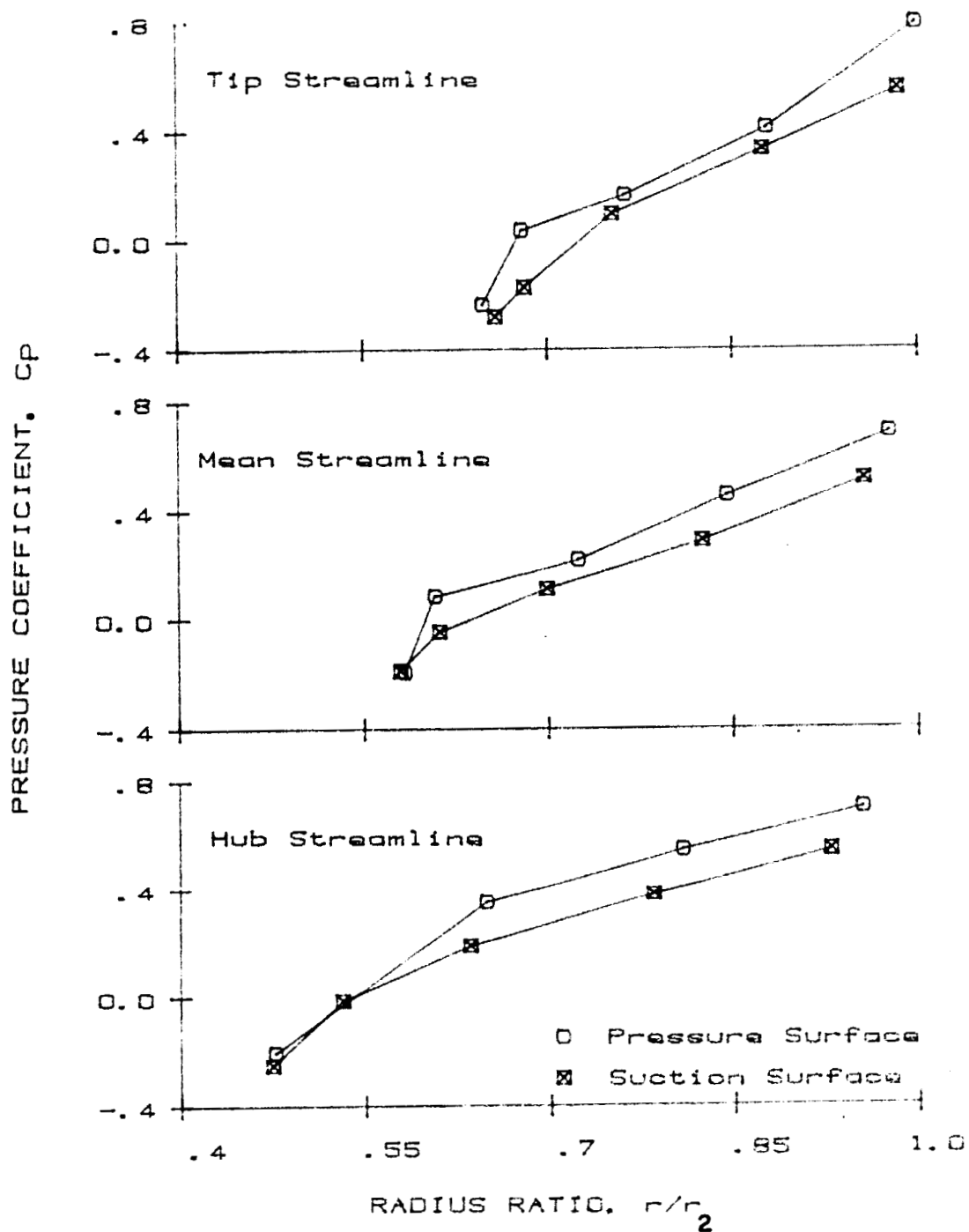


Figure 5.23 Impeller Blade Static Pressure Distribution (IGV Angle = 15°, $\phi = 0.325$)

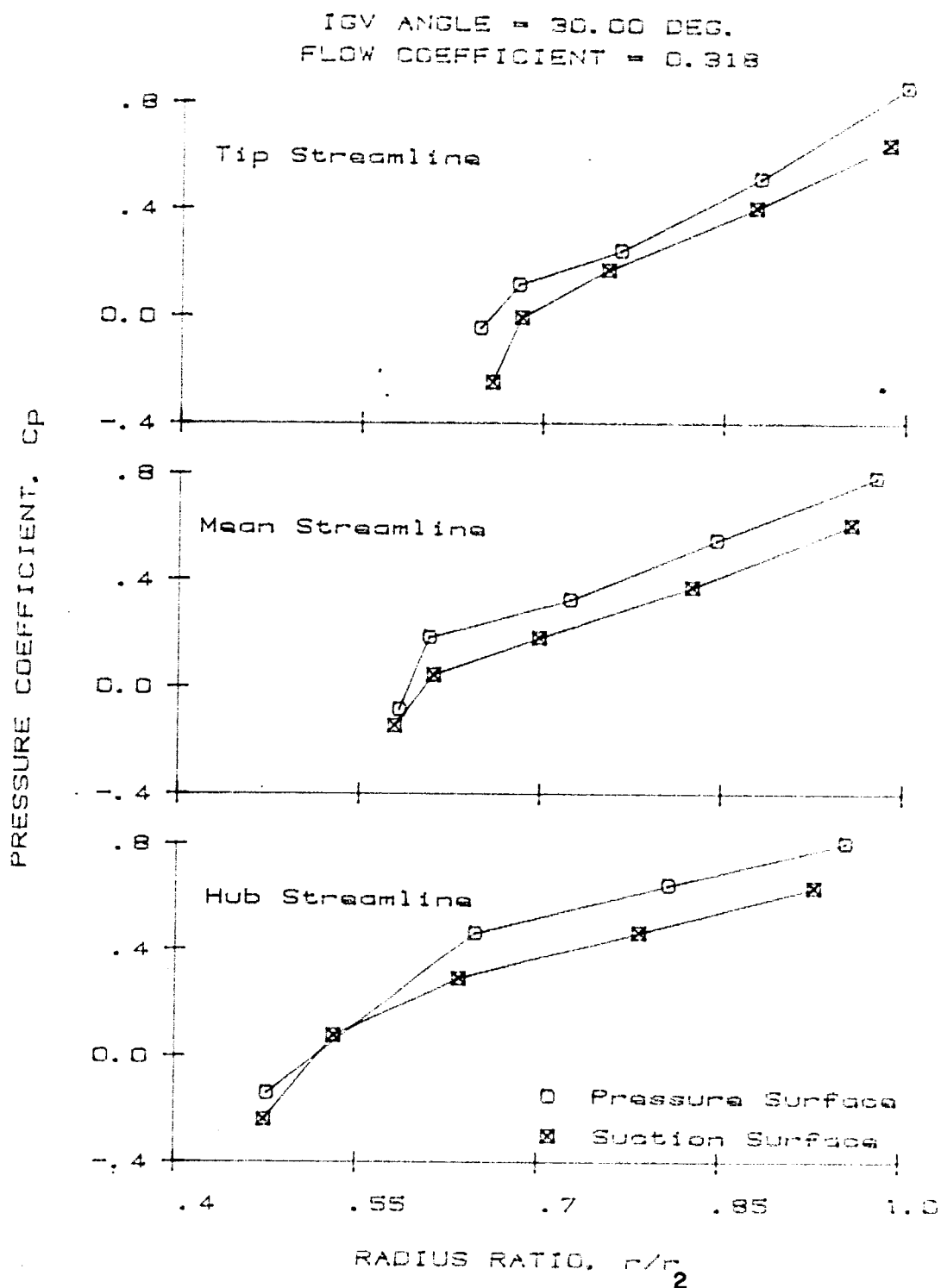


Figure 5.24 Impeller Blade Static Pressure Distribution (IGV Angle = 30°, $\phi = 0.318$)

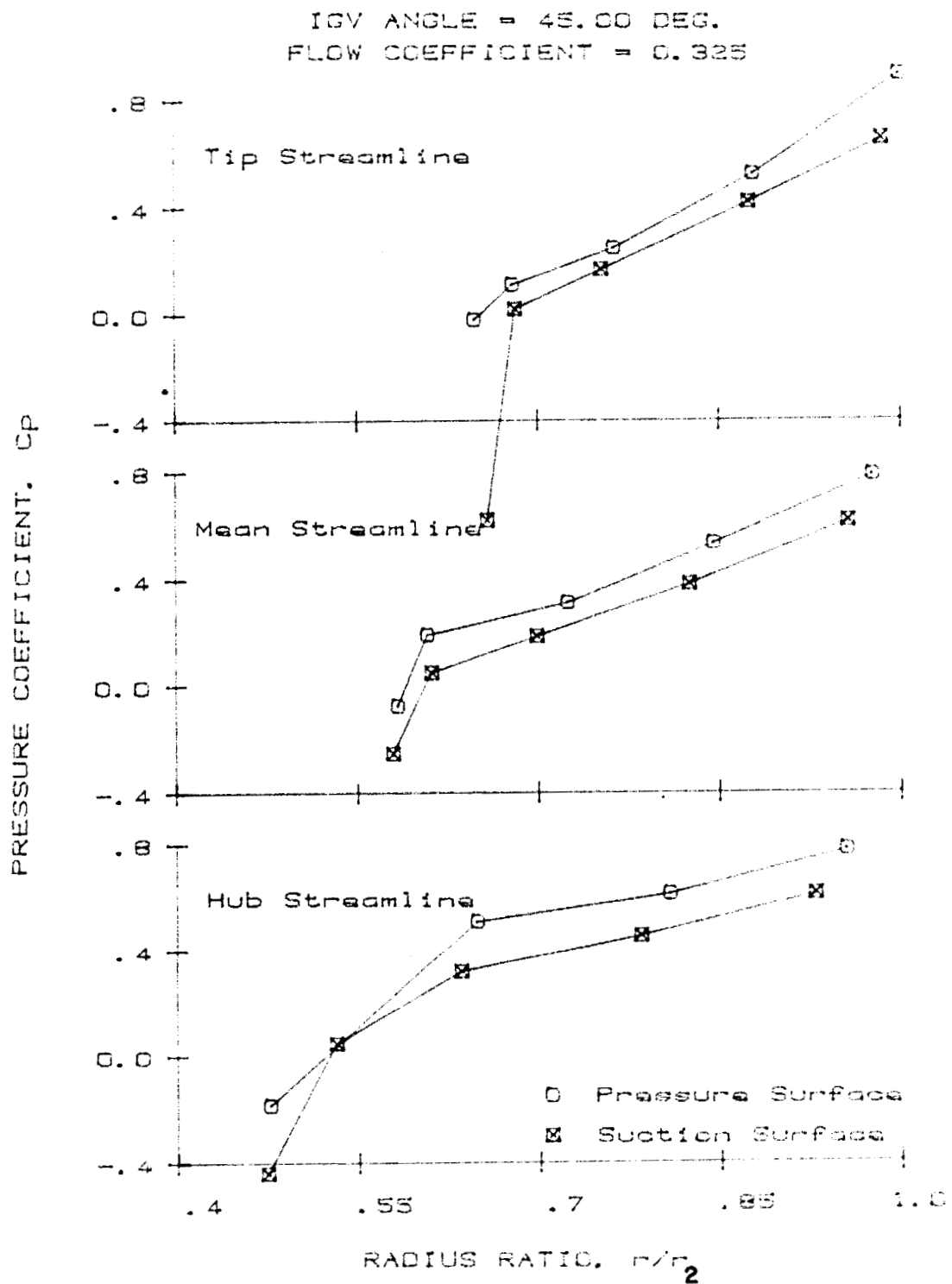


Figure 5.25 Impeller Blade Static Pressure Distribution (IGV Angle = 45°, $\phi = 0.325$)

through B5 of Appendix B.

Several general observations can be made on the overall performance of the compressor. It was noted in the previous section that the power coefficient, \mathcal{P} , and thus the power transmitted to the air, was a monotonically increasing function of flow rate over the range of conditions investigated. The power is also equal to the torque times the angular speed of the impeller. The torque on the impeller is due to the pressure difference between the suction and pressure surfaces, integrated over the blades of the impeller. The area enclosed by the impeller blade pressure and suction surface pressure coefficient distributions is a measure of this pressure force. Thus, an increase in the area between these curves is expected as the flow rate increases. This is observed in the data presented in Figures 5.6 through 5.25, although the change from point to point is small.

The difference in pressure between the two blade surfaces is due to the Coriolis acceleration of the fluid as it passes through the impeller. The Coriolis acceleration is proportional to $\vec{\omega} \times \vec{V}$, where $\vec{\omega}$ is the vector rotational velocity and \vec{V} is the vector velocity of the fluid in the rotating reference frame. Since the pressure differential between the impeller blade pressure and suction surfaces integrated over the blade area is the force producing the Coriolis acceleration, the magnitude of the pressure differential is roughly an indication of the flow velocity through a certain portion of the passage. Thus, regions of high pressure differential indicate high velocities and regions of low pressure differential indicate low velocities. In regions where the suction surface static pressure is greater than the pressure surface static pressure, a reverse flow is suspected. The impeller blade

static pressure distribution, therefore, gives an indication of the magnitude and direction of the impeller passage velocities.

The overall effect of relative inlet flow angle on the static pressure distributions should be noted. At low values of inlet guide vane angle, the difference in relative flow angle, β_1 , between the hub and the tip is considerable. The change in this flow angle with flow rate is also significant. As the inlet guide vane angle is increased, the difference in β_1 between the hub and tip becomes smaller as well as the change in β_1 with flow rate. Consequently, changes in the impeller static pressure distribution at low values of inlet guide vane angle occur mostly at the blade tip. As the inlet guide vane angle is increased and a more even distribution of relative flow angle is achieved, the changes in pressure distribution occur more evenly over the entire blade. Changes are also more gradual at higher inlet guide vane angles due to more gradual changes in flow angle.

Considering the impeller pressure distributions at any particular inlet guide vane setting, it can be seen that the variation in the magnitude of the pressure coefficients on the impeller blades with flow rate is gradual, whereas the changes in Ψ with flow rate shown in Figure 5.1 are considerable. In regions of flow rate where the flow through the impeller is not severely stalled or distorted, the pressure rise due to the centrifugal pressure field is approximately constant since it only depends on the radius of the impeller and the angular velocity. The static pressure at the impeller inlet changes gradually with flow rate since the pressure decreases with increasing velocity. It is this gradual change in static pressure at the impeller inlet in addition to the turning of the flow at the inlet of the impeller which

accounts for changes in the magnitude of the static pressure distribution. The large changes observed in the pressure rise coefficient versus flow coefficient plot, Figure 5.1, are due to the pressure rise gained through diffusing the flow leaving the impeller. Since the magnitude of the absolute velocity leaving the impeller decreases with increasing flow rate over the range investigated, the pressure rise gained by diffusion of the exit flow decreases as the flow rate increases. Thus, the downward slope observed in the performance plots, Figures 5.1 and 5.2.

Figures 5.6 through 5.10 show the impeller pressure distribution at a stalled condition for all inlet guide vane settings. As can be seen, the pressure distributions at all inlet guide vane angles are very similar. This is consistent with Figure 5.4, which showed the power coefficients converging toward a single value as the flow rate decreased. Since the power coefficient is roughly proportional to the area between the pressure coefficient curves, it is expected that the areas between the curves for different inlet guide vane settings will be equal. Considering the tip streamline pressure distributions, it appears that the flow velocity towards the tips of the blades is very small and, therefore, a stalled condition exists. It is reasonable that stalling occurs at the tips first, since the incidence angle is greatest there.

When stalling occurs over part of the passage, the velocities become small and thus the effective flow area is reduced. As the flow rate is reduced and the stall becomes greater, flow is diverted into adjacent passages of the impeller. As this happens, the incidence angle changes on the adjacent blades, increasing the incidence angle on the on the passage the direction opposite the impeller rotation,

and decreasing the incidence angle on the passage in the direction of rotation. Thus, the stall rotates in a direction opposite that of the impeller. An oscillation in the water manometers used for nulling the impeller exit probes and a noticeable increase in the uncertainty of the pressure data indicated that rotating stall was occurring at all inlet guide vane settings at sufficiently low flow rates. It is not evident from the pressure distributions when separation on the suction surface is a steady condition, or when a rotating stall occurs. It is evident that the flow velocities at the mean streamline and especially the tip streamline are small at low flow rates.

It can be seen from Figures 5.6 through 5.10 that the stall does not propagate through the entire flow channel. The flow reattaches toward the exit of the impeller to give a more uniform velocity profile. Perhaps the turning of the flow to a more radial direction enables the flow to reattach at the impeller exit.

Figures 5.11 through 5.15 show the impeller pressure coefficients for flow coefficients near 0.2. This point is close to the maximum pressure ratio and maximum efficiency points for inlet guide vane angles of -15° and 0° . At higher inlet guide vane settings, the performance is degraded due to separation and stalling, as was seen in Figure 5.2 and noted in the previous section. This can be seen from Figures 5.13 through 5.15 where the velocity at the blade tip is small, however, the flow is not completely stalled. It can be seen that a small region of attached flow at the tip of the impeller inlet exists. A decrease in pressure on the suction surface tip streamline at the impeller inlet indicates an accelerating flow around the leading edge of the vanes due to a positive incidence angle. The

pressure then rises to a value close to that of the pressure surface indicating a low velocity. As in the previous results, a reattachment at the impeller exit is evident due to the pressure differential between blade surfaces..

Figures 5.16 through 5.20 show the distributions of the impeller pressure coefficients for flow coefficient values of approximately 0.27. For inlet guide vane angles of 30° and 45° , significant changes in the pressure distribution at the hub are evident. For inlet guide vane angles less than 30° , there are no significant changes with flow rate at the hub. At inlet guide vane angles of 30° and 45° , acceleration of the flow around the leading edge of the impeller blades is evident towards the blade tips. The magnitude of this acceleration is greater than in Figures 5.11 through 5.15. This acceleration is due to the high incidence angle on the blades which occurs over most of the flow range at high inlet guide vane angles. This can be seen from Tables B3 through B5. This behavior is not seen at lower inlet guide vane angles since high incidence angles only occur at lower flow rates. Because of this, the velocities at the blade tips are lower and acceleration around the leading edge is less.

At an inlet guide vane angle of -15° , the beginning of negative incidence angles is evident. A definite increase in the pressure coefficient at the suction surface leading edge is seen over the entire blade. There is not yet an indication of stalling on the pressure surface, although a decreasing incidence is noted. The incidence angle at the hub is less than at the tip of the blade. However, there appears to be a slight decrease in velocity at the hub for increasing flow rates for the -15° inlet guide vane angle. It appears that this decrease, as opposed to an increase at

higher inlet guide vane angles and the smaller relative velocity at the hub, has tended to distribute the effects of negative incidence over the entire blade even though the incidence angle is smaller at the hub.

The impeller static pressure distributions at a value of ϕ approximately equal to 0.32 are shown in Figures 5.21 through 5.25. The effects of decreasing incidence are seen clearly for inlet guide vane angles of -15° and 0° . At -15° , the effects are evident over the entire blade. At the mean and tip streamline, a drop in pressure due to acceleration around the blade is seen on the pressure surface. The effect of flow impingement on the suction surface is evident due to higher pressure at the first pressure tap. At the third tap, a significant stall on the pressure surface is seen at the tip with the pressure dropping below that on the suction surface, indicating the possibility of a reverse flow. At the exit of the impeller, the flow appears to reattach to the pressure surface and separate from the suction surface on the tip streamline. At the mean streamline, a small separation from the suction surface is noted, but the most significant flow separations occur at the blade tip, similar to suction surface stall. This behavior is noted for an inlet guide vane angle of 0° at higher flow rates. At 15° , some indication of decreasing incidence is noted, although the flow appears to be uniform. At this point, a significant loss in performance has occurred.

For inlet guide vane angles of 30° and 45° , a positive angle of attack is still evident due to the acceleration of the flow around the leading edge, especially at 45° . This behavior is still evident at the highest flow rates of this investigation. The high acceleration, caused by the turning of the flow, raises the static pressure

throughout the impeller passage as noted previously. Because of the greater turning of the flow, the power imparted to the air is greater, as was discussed in Section 5.1.

It can be seen that changes in inlet guide vane angle have a significant impact on the flow phenomena in the impeller passages. At all inlet guide vane angles, the most significant changes occur at the blade tips, mainly due to the greater relative velocity between the fluid and impeller. The changes in pressure distribution between different inlet guide vane settings are very significant at high flow rates. Decreasing incidence angles cause pressure surface separations at low inlet guide vane angles. At high inlet guide vane angles, positive incidence angles cause high turning of the flow and acceleration around the blade leading edge. The data for the impeller is consistent with that of the overall performance.

Diffuser Flow Field

The flow field in the exit diffuser section was investigated by measuring the static pressure distribution on the diffuser vanes and taking velocity measurements downstream of the diffuser at four locations across the channel and across one vane passage. Figures 5.26 through 5.30 show the diffuser vane static pressure distributions for all inlet guide vane settings at a flow coefficient of approximately 0.32. The data are plotted as the pressure coefficient on the diffuser vane versus percent chord along three streamlines. The mean incidence angle on the diffuser vanes is given in Tables B6 through B10 of Appendix B. The behavior at each of the five inlet guide vane settings is similar. In all cases, the incidence angle on the

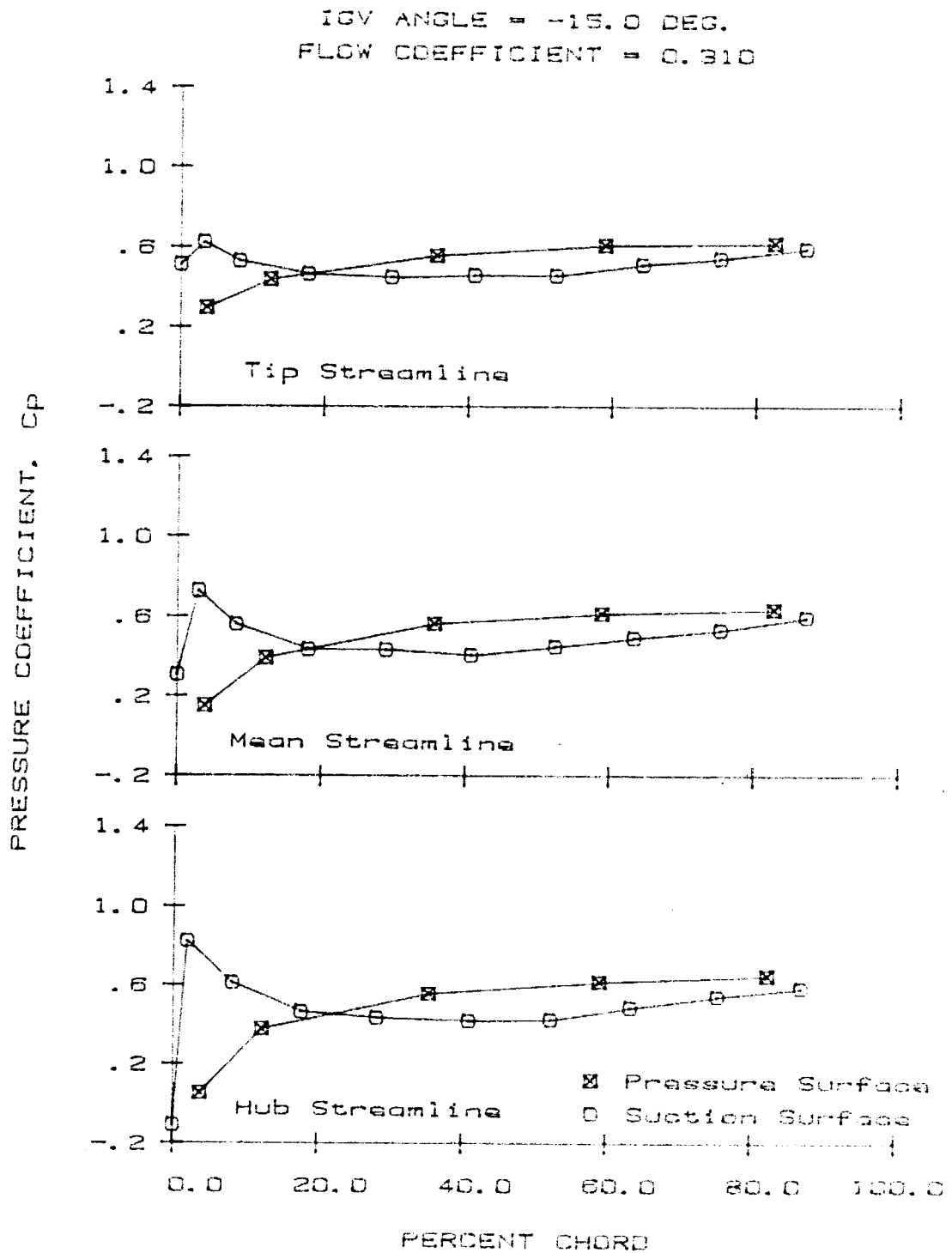


Figure 5.26 Diffuser Vane Static Pressure Distribution (IGV Angle = -15° , $\phi = 0.310$)

ORIGINAL PAGE IS
OF POOR QUALITY

IGV ANGLE = 0.00 DEG.
FLOW COEFFICIENT = 0.319

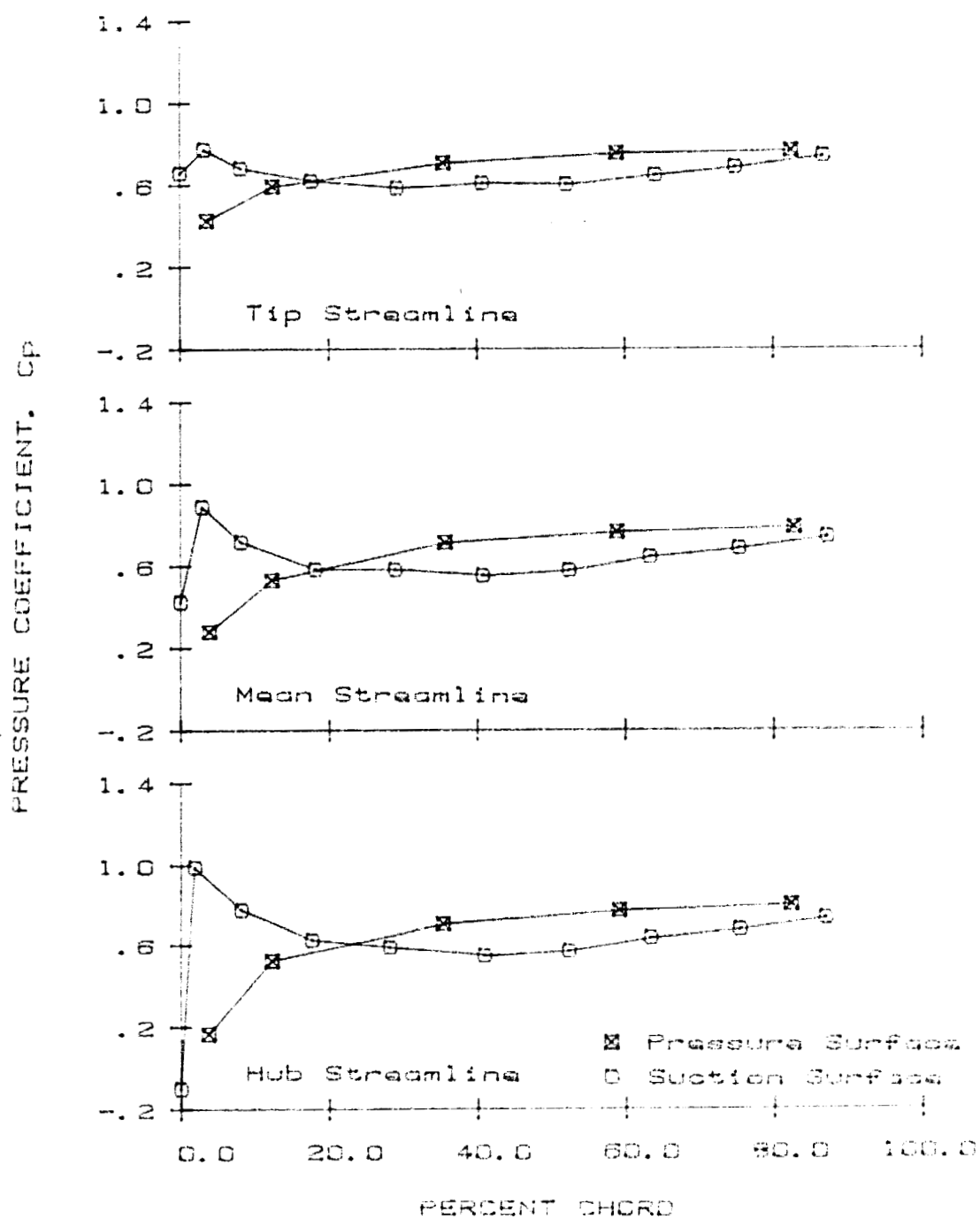


Figure 5.27 Diffuser Vane Static Pressure Distribution (IGV Angle = 0°, $\phi = 0.319$)

ORIGINAL PAGE IS
OF POOR QUALITY

IGV ANGLE = 15.00 DEG.
FLOW COEFFICIENT = 0.324

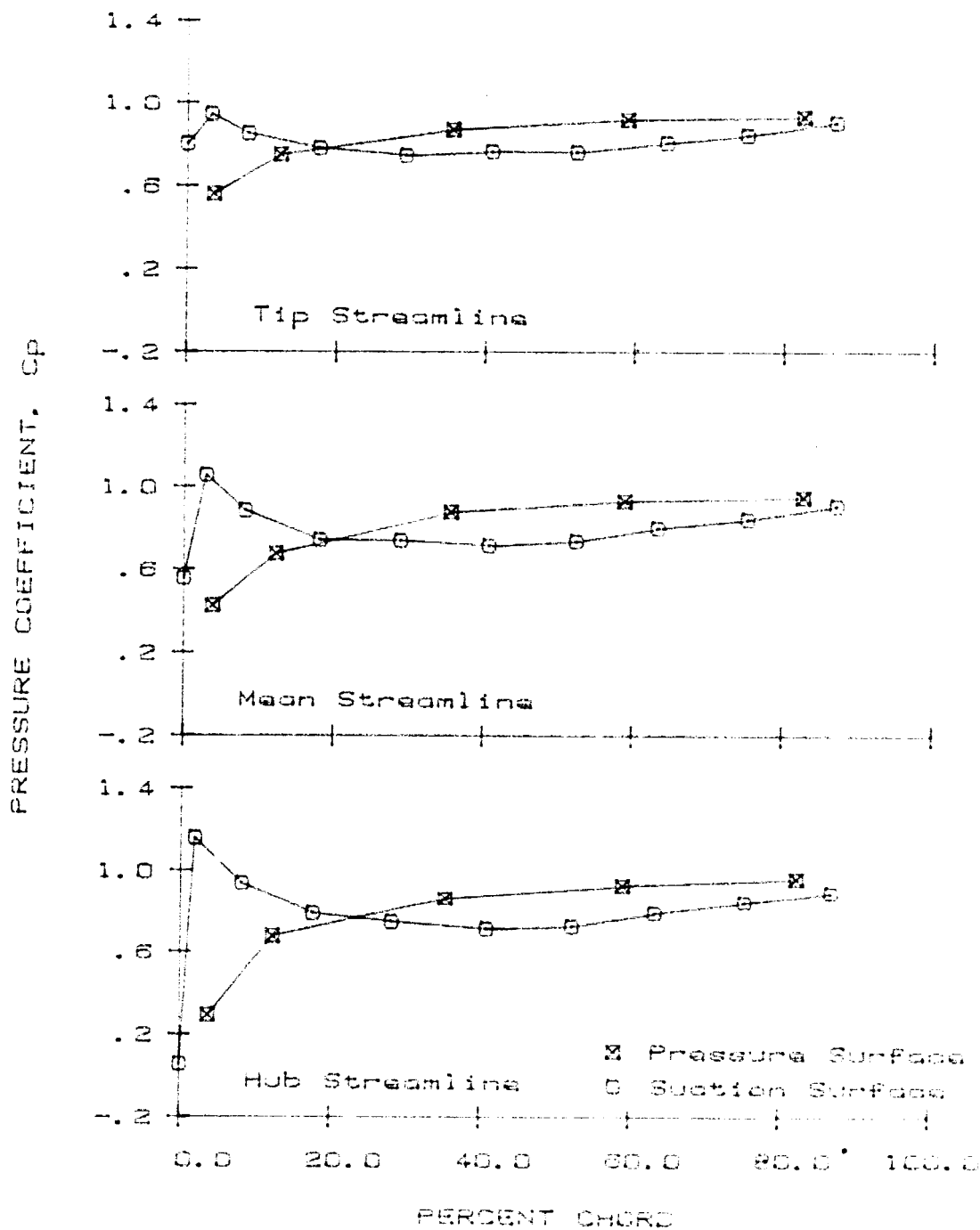


Figure 5.28 Diffuser Vane Static Pressure Distribution (IGV Angle = 15°, $\phi = 0.324$)

ORIGINAL PAGE IS
OF POOR QUALITY

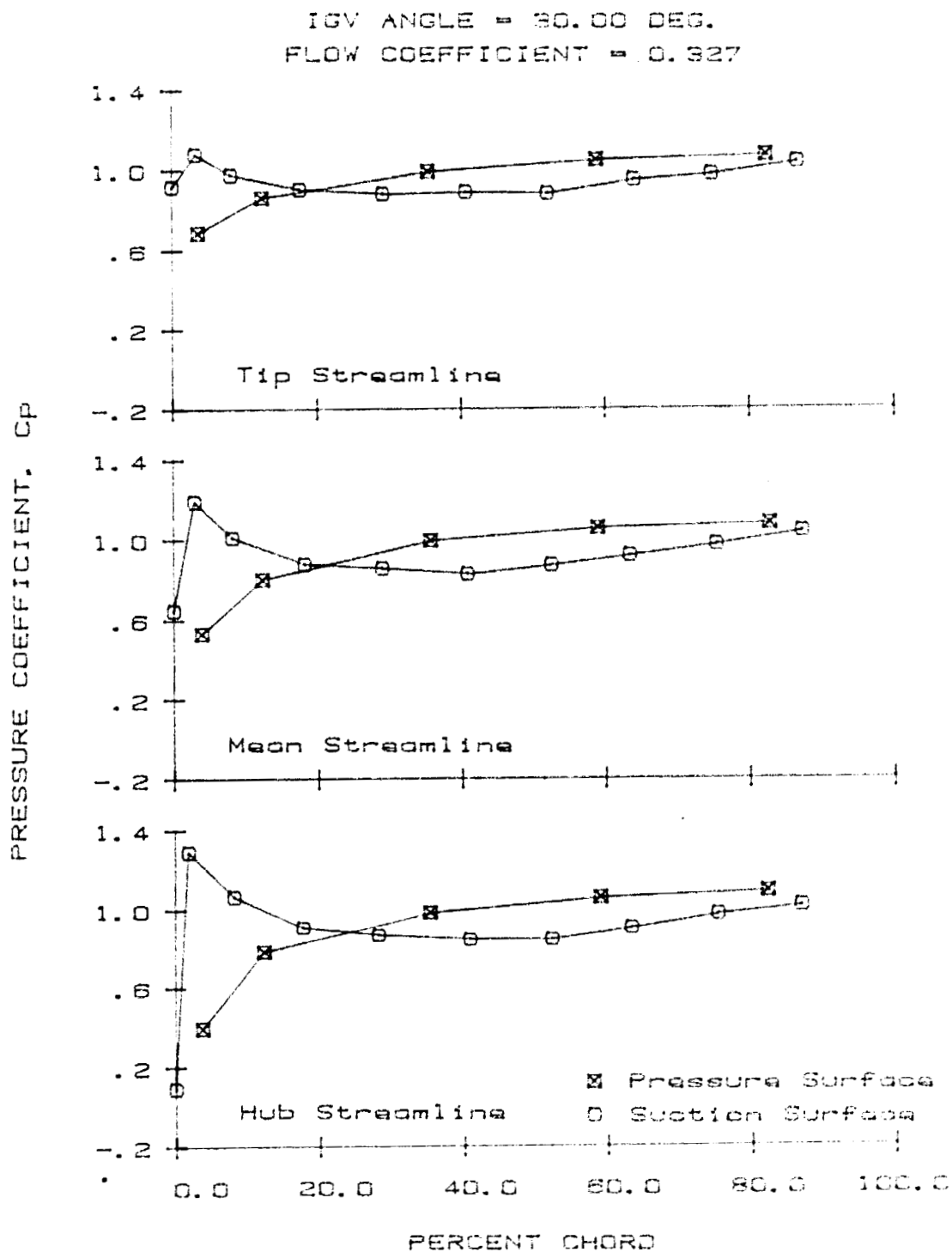


Figure 5.29 Diffuser Vane Static Pressure Distribution (IGV Angle = 30°, $\phi = 0.327$)

IGV ANGLE = 45.00 DEG.
FLOW COEFFICIENT = 0.327

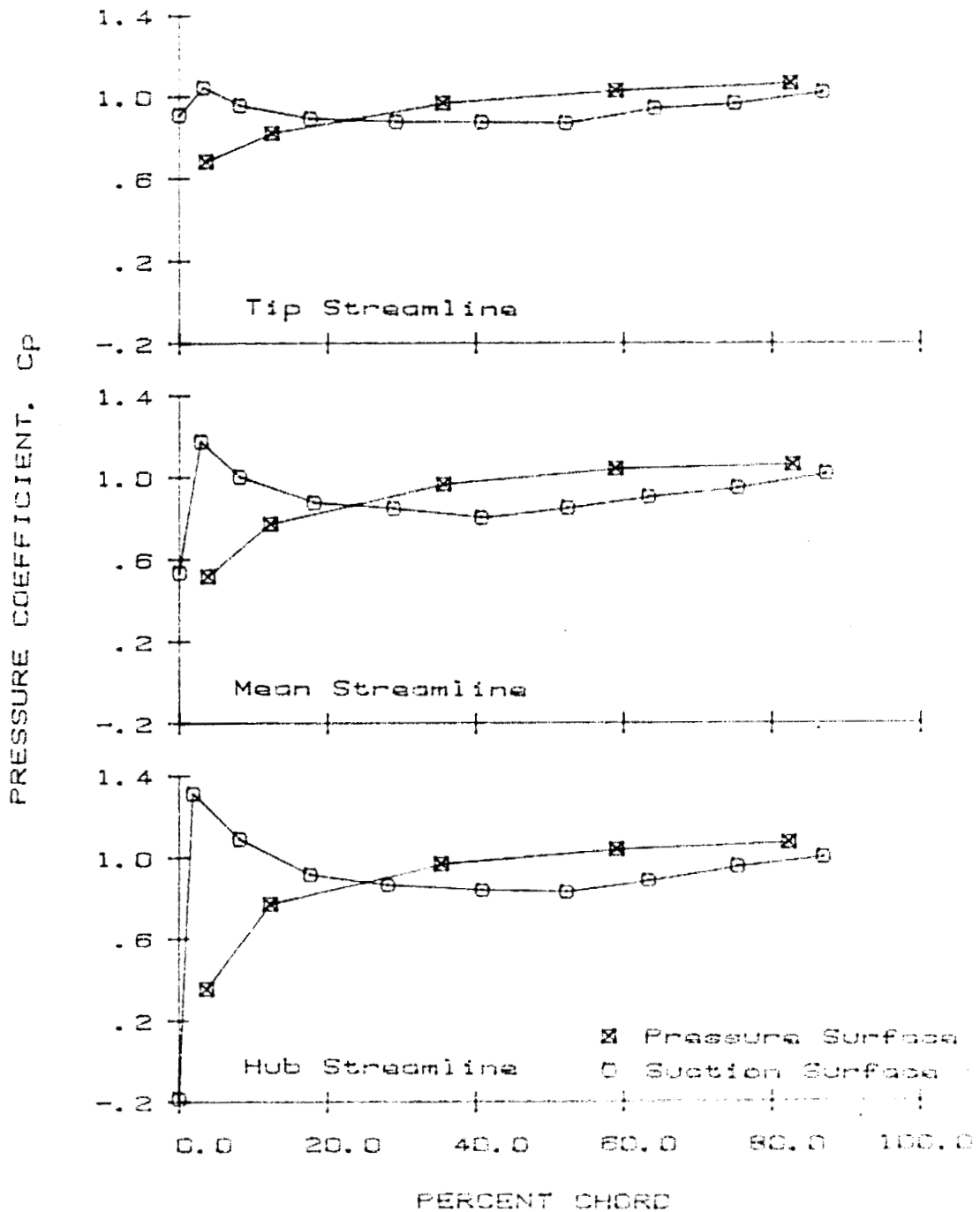


Figure 5.30 Diffuser Vane Static Pressure Distribution (IGV Angle = 45°, $\phi = 0.327$)

vaness is close to 0 or negative across the entire vane with the smallest incidence angle at the hub streamline. The first measurement on the suction surface is at the vane leading edge. This measurement shows a low pressure which indicates an acceleration around the vane. The second measurement on the suction surface shows a high pressure which indicates impingement of the flow onto the suction surface and thus a negative incidence angle. It is reasonable that the most negative incidence angle occurs at the hub since the hub exit radius of the impeller is smaller than the tip radius, and there is a smaller component of angular velocity and a more radial flow.

The magnitude of the pressure coefficients vary with inlet guide vane settings, Figures 5.26 through 5.30. However, the behavior is very similar in all cases. It was noted earlier that the impeller exit flow angle was at best weakly dependent on inlet guide vane angle and very dependent on flow rate. Since all five cases were at similar flow rates, the flow field should be similar, as is the case.

Figures 5.31 and 5.32 show the diffuser static pressure distributions for 0° inlet guide vane angle at two lower flow rates. As the flow rate decreases, the incidence angle becomes increasingly positive. This is indicated by the decreasing acceleration around the vane leading edge. For both cases, a slight acceleration around the leading edge is seen at the mean and hub streamline although the incidence angle appears to be close to the design value. Since the absolute flow angle leaving the impeller increases with decreasing flow rate, it is expected that the incidence angle will become greater as the flow rate decreases.

ORIGINAL PAGE IS
OF POOR QUALITY

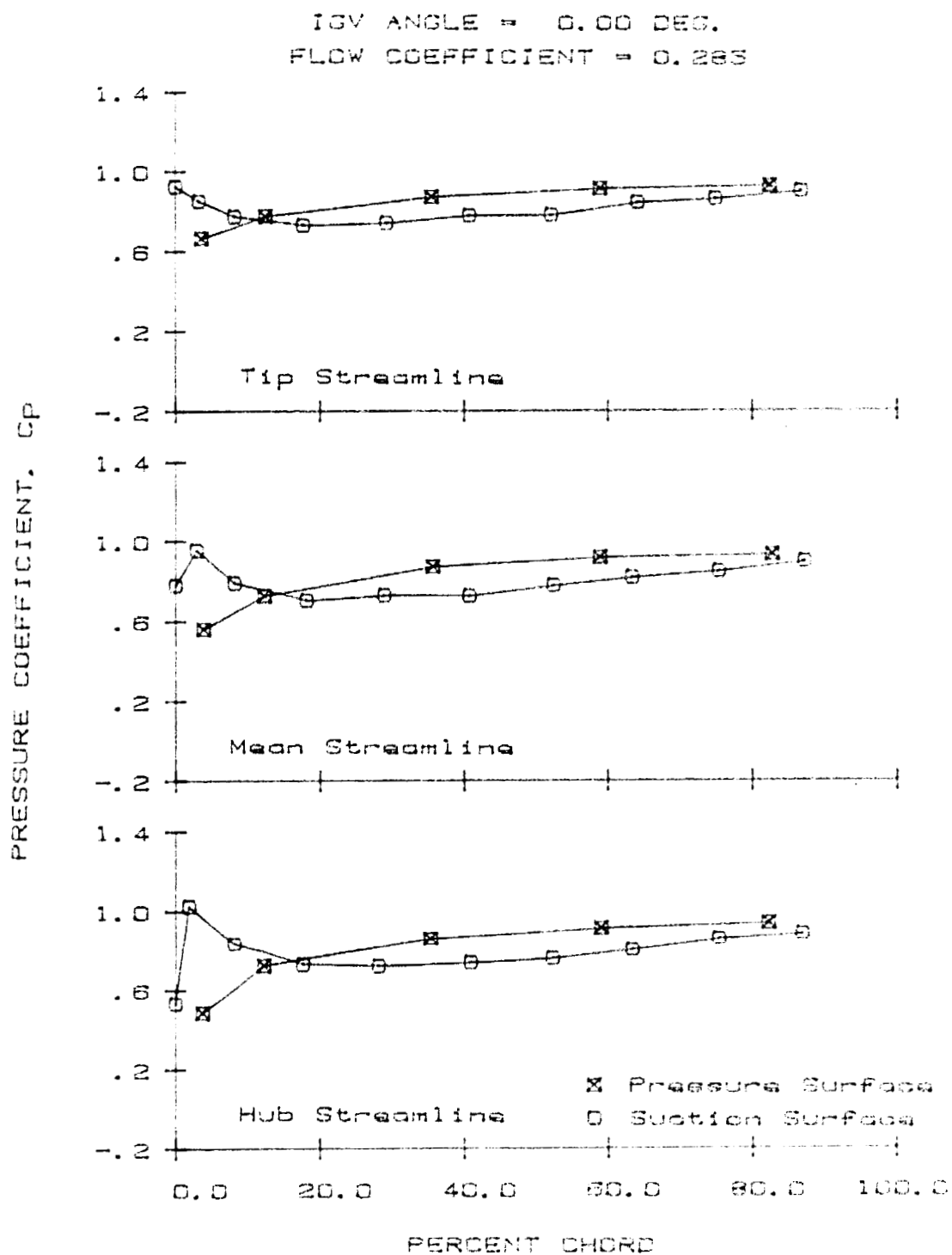


Figure 5.31 Diffuser Vane Static Pressure Distribution (IGV Angle = 0°, $\phi = 0.285$)

ORIGINAL PAGE IS
OF POOR QUALITY

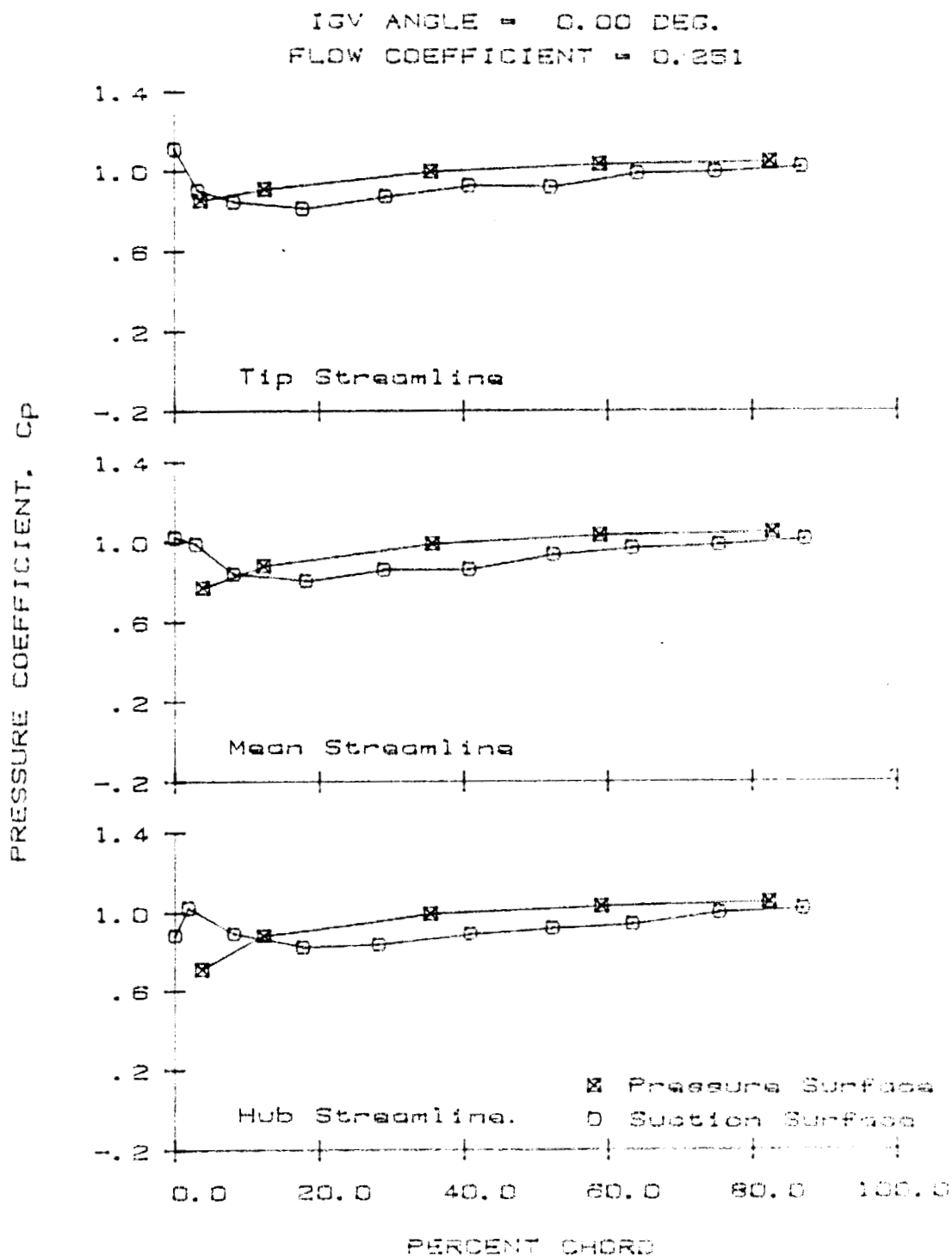


Figure 5.32 Diffuser Vane Static Pressure Distribution (IGV Angle = 0° , $\phi = 0.251$)

Figures 5.33 through 5.37 show the diffuser exit velocity for all inlet guide vane settings at a flow coefficient of approximately 0.32. The data are plotted as the ratio of diffuser exit velocity to mass averaged radial velocity versus percent vane passage at four locations across the passage. As was the case for the diffuser vane pressure distribution, the diffuser exit flow field is similar for all inlet guide vane settings at a particular flow rate. It can be seen that the wake from the diffuser vanes is at an angle across the channel, indicating a change in flow angle across the channel. This is consistent with the diffuser pressure data which showed a varying incidence angle across the vane span. In Figures 5.33 through 5.37, the vane passage increases in the direction of impeller rotation. Thus, the tip wake has rotated furthest. It was noted from the diffuser data that the circumferential velocity was greatest at the tip streamline. Thus, the velocity data concur with the velocities inferred from the diffuser pressure data. The wake at the hub shows some discrepancy from the behavior noted above. This is possibly due to the proximity of the probe and the wall and the effect of the slot through which the probe passed.

Figures 5.38 and 5.39 show the diffuser exit velocity profiles at an inlet guide vane setting of 0° for decreasing flow rates. The same behavior is noted in these figures, except that the angle of the wake across the flow channel has increased. Since a difference in angular velocity will always exist across the channel due to the varying impeller exit radius, this increase is reasonable. As noted above, the absolute angular velocity increases as between hub and tip angular velocities. Because of this, the angle of the wake across the channel has increased.

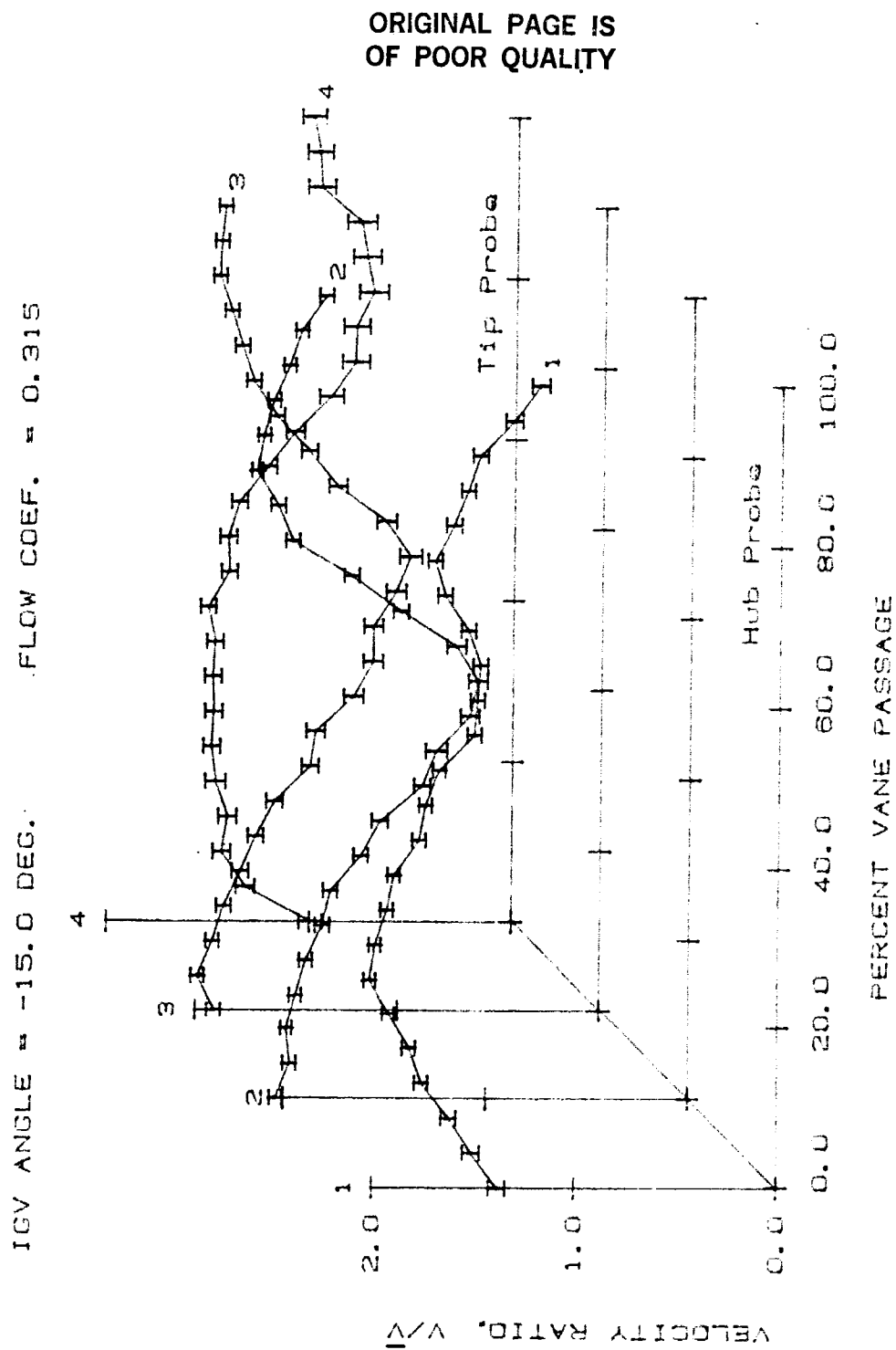


Figure 5.33 Diffuser Exit Velocity Profile (IGV Angle = -15° , $\phi = 0.315$)

ORIGINAL PAGE IS
OF POOR QUALITY

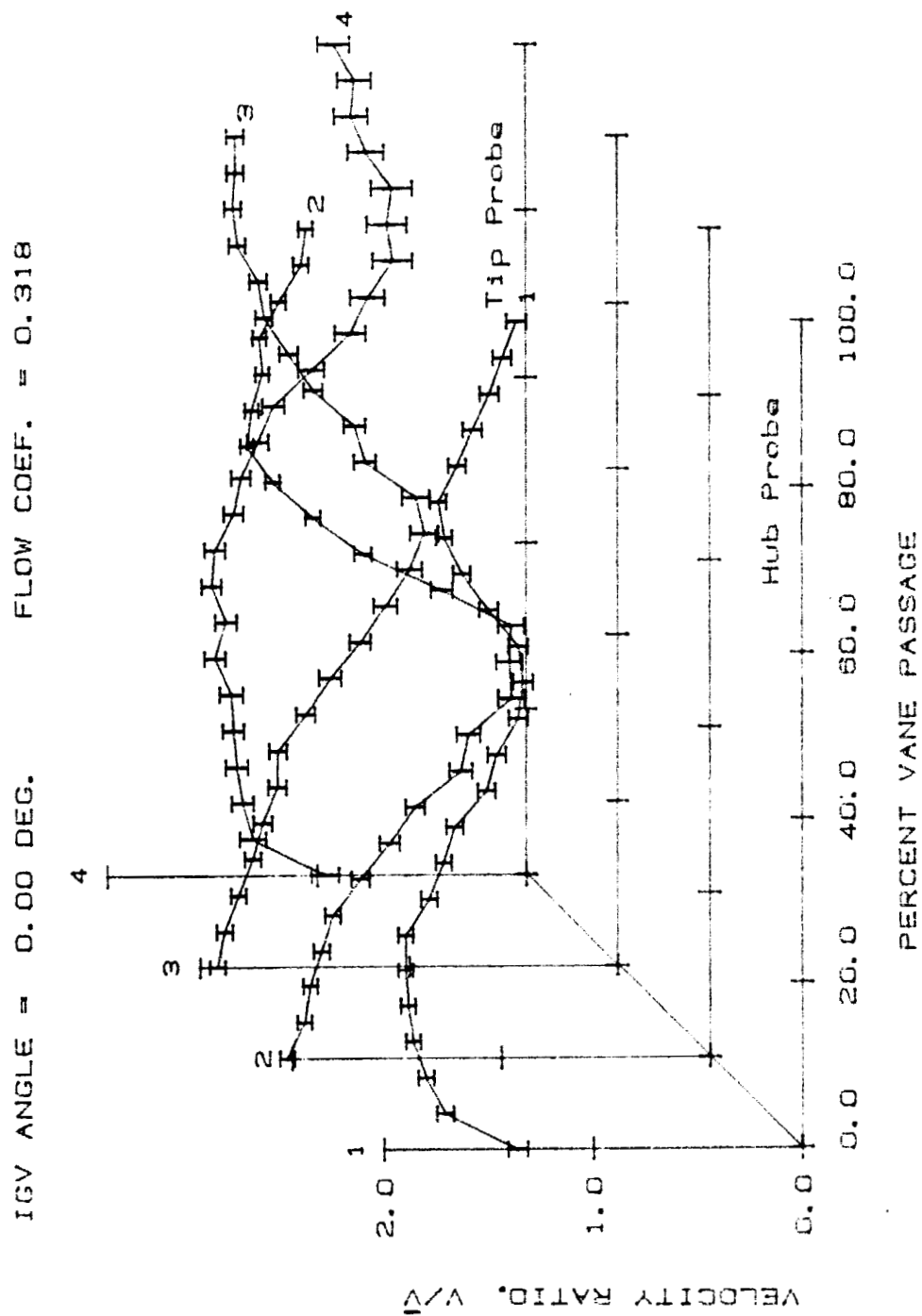


Figure 5.34 Diffuser Exit Velocity Profile (IGV Angle = 0° , $\phi = 0.318$)

ORIGINAL PAGE IS
OF POOR QUALITY

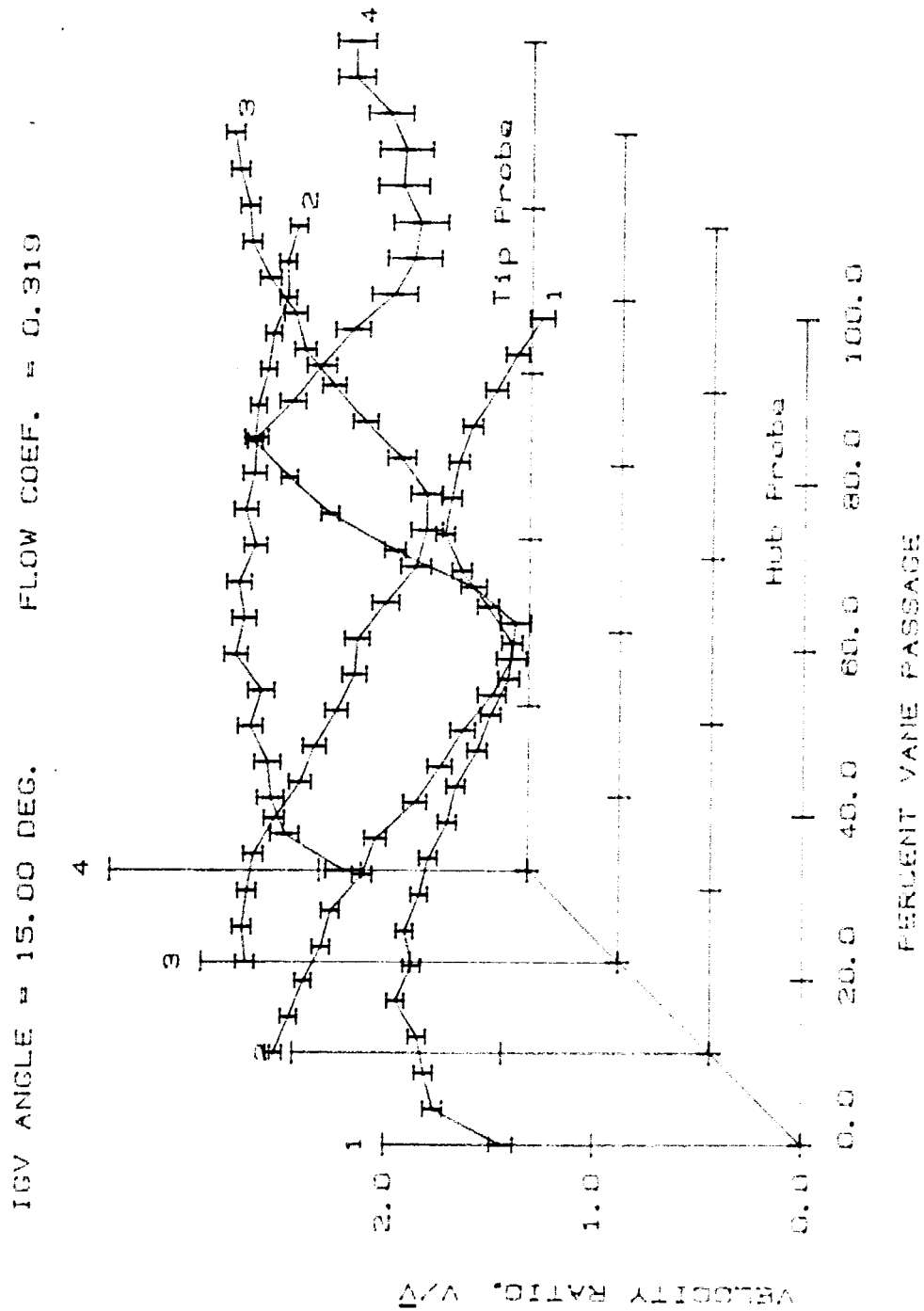


Figure 5.35 Diffuser Exit Velocity Profile (IGV Angle = 15° , $\phi = 0.319$)

ORIGINAL PAGE IS
OF POOR QUALITY

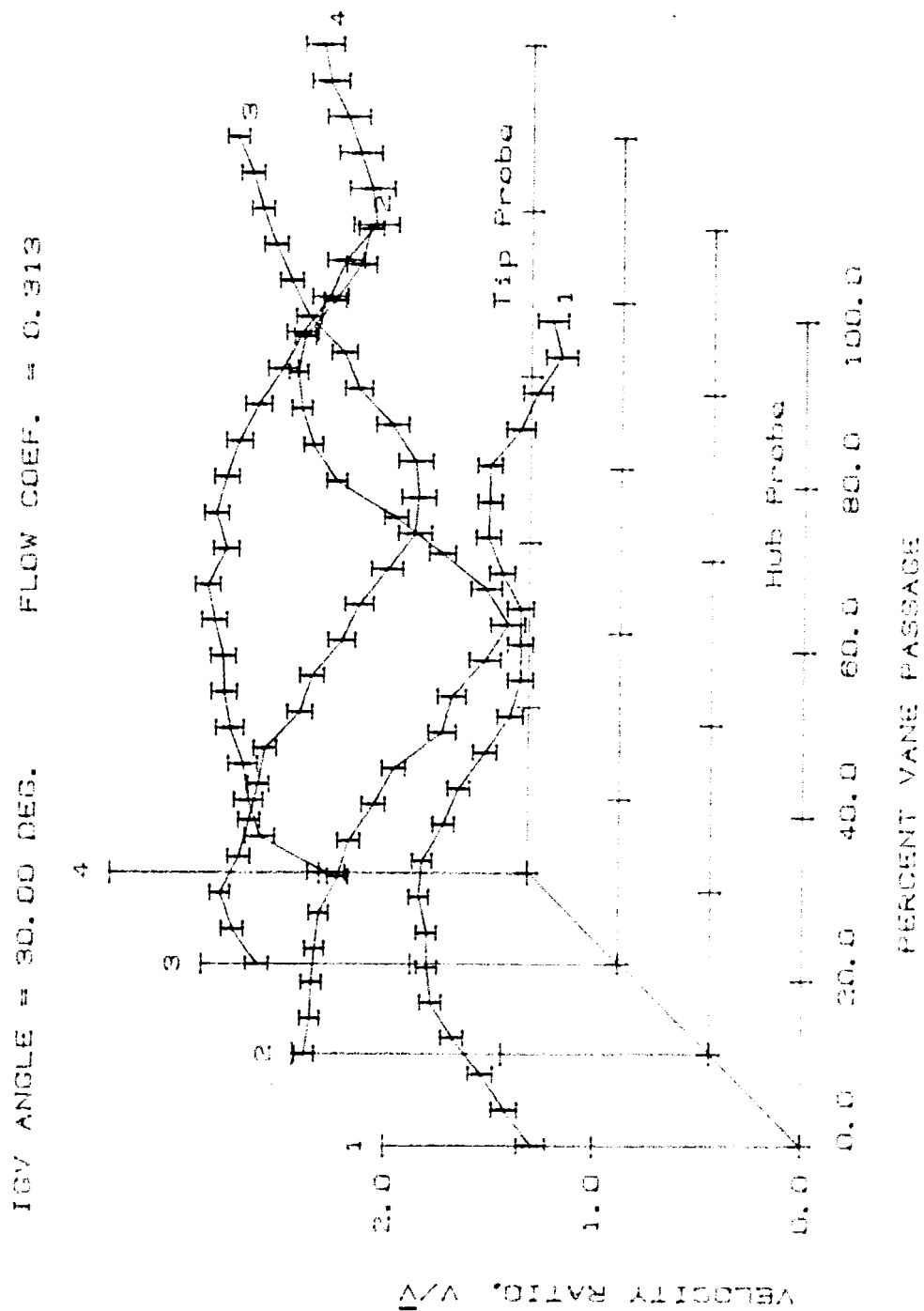


Figure 5.36 Diffuser Exit Velocity Profile (IGV Angle = 30° , $\phi = 0.313$)

ORIGINAL PAGE IS
OF POOR QUALITY

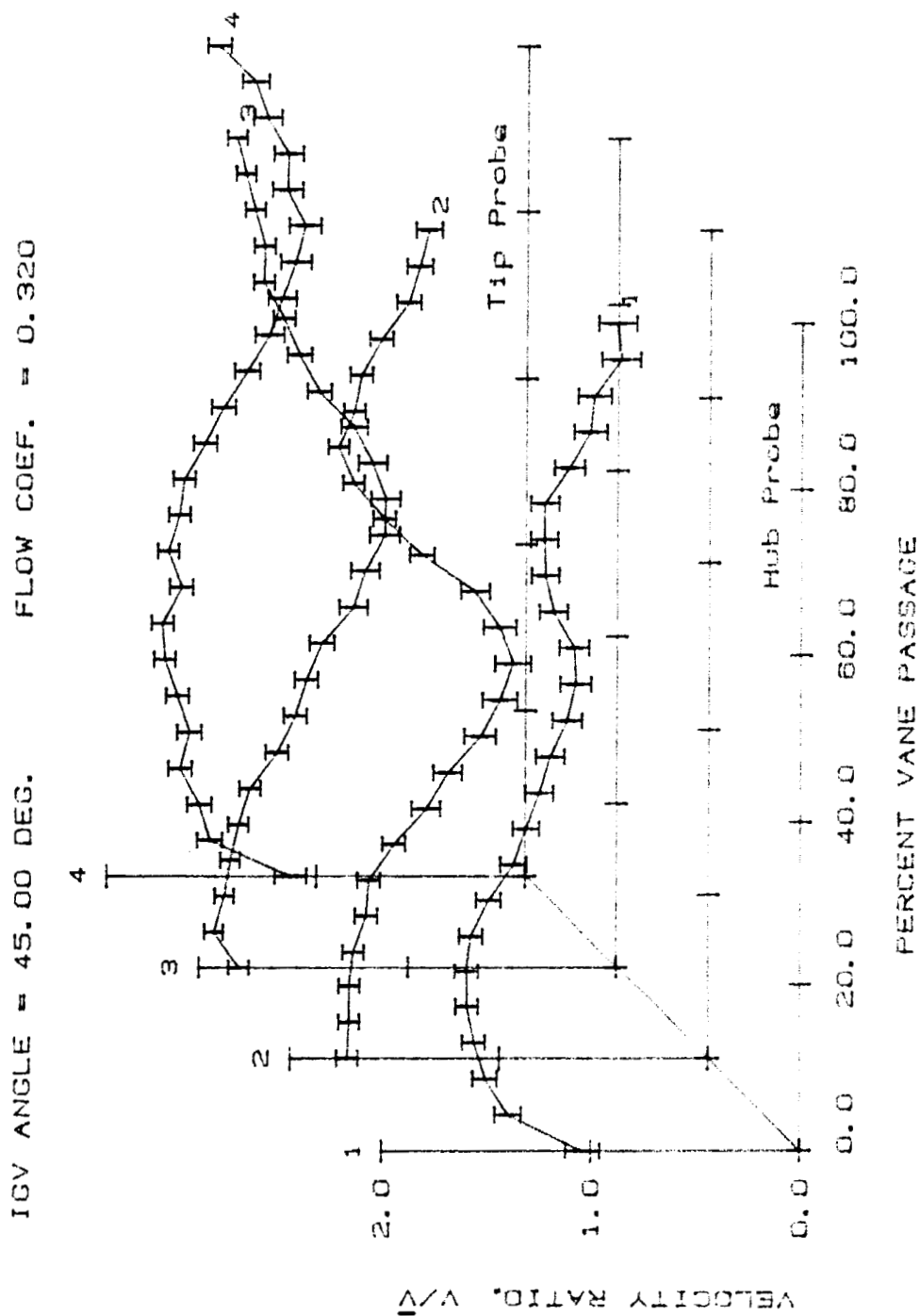


Figure 5.37 Diffuser Exit Velocity Profile (IGV Angle = 45° , $\phi = 0.320$)

ORIGINAL PAGE IS
OF POOR QUALITY

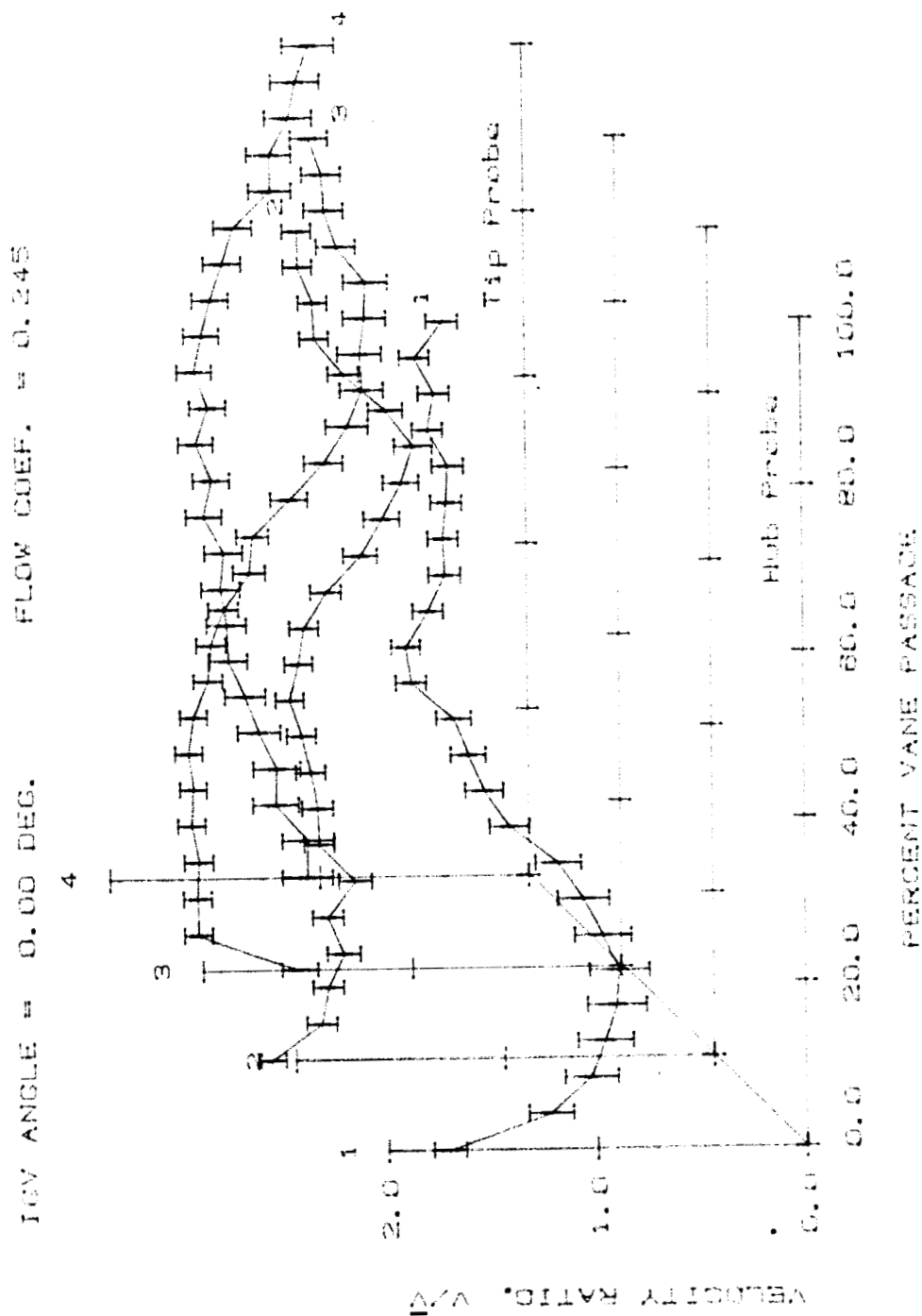


Figure 5.39 Diffuser Exit Velocity Profile (IGV Angle = 0° , $\phi = 0.245$)

Based on the above discussions, it can be seen that the inlet guide vane angle has a lesser effect on diffuser performance than does flow rate. It was seen that pressure and velocity distributions in the diffuser changed mainly with flow rate.

CHAPTER 6 - SUMMARY AND CONCLUSIONS

The Purdue Research Centrifugal Compressor Facility was constructed to investigate fundamental flow phenomena in centrifugal turbomachinery. It is a low speed, large scale machine designed to facilitate the investigation of flow properties in the inlet, impeller, and diffuser. The facility was extensively instrumented with pressure taps and probes throughout the flow channels, which enabled the rotating impeller blade, the diffuser vane, and flow channel static pressure distributions to be measured. Probes at the inlet and exit of the impeller and downstream of the exit diffuser vanes allowed measurement of total pressure, temperature, and flow angle. The facility was operated at 1795 rpm but was capable of 2400 rpm, accomplished by changing the pulley ratio.

Data acquisition and analysis was accomplished via computer which greatly reduced the time needed to acquire and reduce the data and allowed large amounts of data to be sampled. Pressures in the facility were measured with pressure transducers and rotating scanners interfaced through the computer and data acquisition system. A computer controlled butterfly valve regulated the flow rate through the facility. Much of the data was reduced in real time and the performance parameters of the facility were available immediately following the data acquisition.

In its current configuration, the facility was utilized to investigate and quantify the effect of flow rate and inlet flow field prewhirl on the overall and detailed aerodynamic performance. Detailed aerodynamic data were acquired over a range of flow rates at five inlet guide vane settings from -15° to 45° . It was found that

changes in the inlet guide vane angle significantly affected the performance. Increasing the inlet guide vane angle increased both the pressure rise and the flow rate at which the maximum pressure rise occurred. The efficiency behavior was similar to the pressure rise behavior with the maximum efficiency occurring at low flow rates for small inlet guide vane angles and higher flow rates for increased inlet guide vane angles. It was seen that for a given flow rate, significant improvements in performance could be achieved by varying the inlet guide vane angle.

The change in inlet guide vane angle affected the static pressure distribution on the impeller blades. At low flow rates, only small changes could be detected between angles. As the flow rate increased, the distributions differed significantly. At low inlet guide vane angles, the distribution in pressure coefficient at the hub changed very little with flow rate. The change was much greater at the tips, with increasing flow rate causing decreased incidence angles on the impeller blades and separation from the pressure surface. The changes in distribution of the pressure coefficient occurred more evenly over the entire blade at higher inlet guide vane angles. The incidence angle on the blades remained positive over the entire flow range, causing high accelerations of the flow around the leading edge of the impeller blades. However, no separation at high flow rates was evident.

The change in inlet guide vane angle had little effect on the velocity field and pressure distribution in the vaned exit diffuser. This conclusion is valid over a limited range of flow rates, however, and conditions of distorted flow or stall could possibly affect the diffuser data.

The incidence angle to the diffuser vanes was observed to vary across the flow channel due to a change in radius of the impeller across the flow channel. The wakes from the diffuser vanes were at an angle across the channel because of the non-constant peripheral velocity component, and this angle increased with decreasing flow rate. The flow rate was observed to have a much greater effect on the static pressure distribution and velocity field in the exit diffuser than did the inlet guide vane angle.

The investigation of the facility performance and detailed aerodynamics was an initial study to establish the Purdue Research Centrifugal Compressor Facility. Future investigations include measurement of the three-dimensional velocity field in the rotating impeller using LDV and studies of the unsteady impeller-diffuser interactions.

LIST OF REFERENCES

LIST OF REFERENCES

- [1] Dixon, S.L. *Fluid Mechanics, Thermodynamics of Turbomachinery*. Oxford: Pergamon Press, 1978.
- [2] Dean, Robert C. Jr. "The Centrifugal Compressor". Creare Technical Note TN-183, *Gas Turbine International*, March-April and May-June, 1973.
- [3] Qinghuan, Wang. "Theoretical and Experimental Investigation for Some Basic Physical Phenomena of Centrifugal Compressors". ASME Technical Report 86-GT-74, Gas Turbine Conference and Exhibit, Dusseldorf, West Germany, June, 1986.
- [4] Inoue, M. and Cumpsty, N.A. "Experimental Study of Centrifugal Impeller Discharge Flow in Vaneless and Vaned Diffusers". *Journal of Engineering for Gas Turbines and Power* Vol. 106, April 1984.
- [5] Simon, H. ; Wallmann, T. ; and Monk, T. "Improvements in Performance Characteristics of Single-Stage and Multistage Centrifugal Compressors by Simultaneous Adjustment of Inlet Guide Vanes and Diffuser Vanes". ASME Technical Report 86-GT-127, Gas Turbine Conference and Exhibit, Dusseldorf, West Germany, June, 1986.
- [6] Kyrtatos, N. and Watson, N. "Application of Aerodynamically Induced Prewhirl to a Small Turbocharger Compressor". ASME Technical Report 80-GT-23, Gas Turbine Conference and Products Show, New Orleans, La., March, 1980.
- [7] Wood, Jerry R.; Adam, Paul W.; and Buggele, Alvin E. "NASA Low-Speed Centrifugal Compressor For Fundamental Research". NASA Technical Memorandum 83398.
- [8] Vavra, M.H. and Gawain, T.H. "Compressor Test Rig For Investigation of Flow Phenomena in Turbo-Machines". Technical Report No. 12 on Project No. NR 061-058, Feb., 1955.
- [9] Bergsten, Daniel E. and Fleeter, Sanford. "The Effect of Incidence Angle on the Overall Three-Dimensional Aerodynamic Performance of a Classical Annular Airfoil Cascade". NASA CR-168127, 1983.
- [10] Bryer, D.W. and Pankhurst, R.C. *Pressure Probe Methods for Determining Wind Speed and Flow Direction*. London: Her Majesty's Stationery Office, 1971.
- [11] *Interim Supplement 19.5 on Instruments and Apparatus*. Report of ASME Research Committee on Fluid Meters, Sixth Edition, 1971.
- [12] Stauter, R. Charles and Fleeter, Sanford. "The Design and Instrumentation of the Purdue Annular Cascade Facility with Initial Data Acquisition and Analysis". NASA CR-167861, 1982.
- [13] Scanivalve Pressure Transducer Specifications, Scanivalve Corporation, San Diego, 1984.

- [14] Scheaffer, Richard L. and McClave, James T. *Statistics for Engineers*. Boston: Duxbury Press, 1982.
- [15] *Temperature Measurement Handbook and Encyclopedia*. Omega Engineering, Inc., 1984.

APPENDICES

Appendix A Coordinates of Test Facility Channels and Pressure Taps

Table A1. Impeller Coordinates

hub streamline		tip streamline	
x(cm)	r(cm)	x(cm)	r(cm)
0.0	15.16		
-1.27	15.08		
-2.54	15.04		
-3.81	15.06	-3.81	25.25
-5.08	15.14	-5.08	25.20
-6.35	15.24	-6.35	25.15
-7.62	15.39	-7.62	25.17
-8.89	15.57	-8.89	25.25
-10.16	15.85	-10.16	25.37
-11.43	16.15	-11.43	25.58
-12.70	16.54	-12.70	25.88
-13.97	16.97	-13.97	26.31
-15.24	17.48	-15.24	26.85
-16.51	18.03	-16.51	27.58
-17.78	18.69	-17.78	28.47
-19.05	19.43	-19.05	29.54
-20.32	20.27	-20.32	30.76
-21.59	21.21	-21.18	31.75
-22.86	22.25	-22.17	33.02
-24.13	23.42	-23.06	34.29
-25.40	24.71	-23.83	35.56
-25.98	25.40	-24.49	36.83
-26.97	26.67	-25.10	38.10
-27.89	27.94		
-28.68	29.21		
-29.41	30.48		
-30.07	31.75		
-30.66	33.02		
-31.17	34.29		
-31.62	35.56		

Table A2. Inlet Channel Wall Coordinates

hub streamline		tip streamline	
x(cm)	r(cm)	x(cm)	r(cm)
		20.45	57.15
		20.42	55.88
		20.42	54.61
		20.37	53.34
29.74	52.07	20.29	52.07
29.69	50.80	20.22	50.80
29.67	49.53	20.07	49.53
29.62	48.26	19.89	48.26
29.56	46.99	19.63	46.99
29.46	45.72	19.35	45.72
29.36	44.45	19.00	44.45
29.21	43.18	18.59	43.18
29.01	41.91	18.14	41.91
28.70	40.64	17.60	40.64
28.45	39.37	16.97	39.37
28.09	38.10	16.26	38.10
27.66	36.83	15.44	36.83
27.20	35.56	14.53	35.56
26.90	34.29	13.46	34.29
26.06	33.02	12.29	33.02
25.40	31.75	11.58	32.36
24.64	30.48	10.31	31.24
23.82	29.21	9.04	30.28
22.88	27.94	7.77	29.39
21.89	26.67	6.50	28.63
20.75	25.40	5.23	27.94
20.42	25.07	3.96	27.33
19.15	23.72	2.69	26.85
17.88	22.68	1.42	26.39
16.61	21.67	0.15	26.04
15.34	20.77	-1.12	25.70
14.07	19.94	-2.39	25.48
12.80	19.18	-3.66	25.35
11.53	18.52		
10.26	17.91		
8.99	17.40		
7.72	16.89		
6.45	16.46		
5.18	16.05		
3.91	15.70		
2.64	15.42		
1.37	15.19		
0.10	15.04		

Table A3. Diffuser Channel Wall Coordinates

hub streamline		tip streamline	
x(cm)	r(cm)	x(cm)	r(cm)
-32.26	38.05	-25.15	38.05
-32.54	39.37	-25.70	29.37
-32.77	40.64	-26.14	40.64
-32.92	41.91	-26.57	41.91
-33.07	43.18	-26.90	43.18
-33.17	44.45	-27.20	44.45
-33.25	45.72	-27.43	45.72
-33.32	46.99	-27.61	46.99
-33.38	48.26	-27.76	48.26
-33.40	49.53	-27.89	49.53
		-27.99	50.80
		-28.04	52.07
		-28.09	53.34
		-28.12	54.61

Table A4. Coordinates for NACA 0015 Airfoil Section

x(cm)	y(cm)
0.157	0.300
0.318	0.414
0.635	0.564
0.952	0.665
1.270	0.744
1.905	0.848
2.540	0.912
3.175	0.942
3.810	0.952
5.080	0.922
6.350	0.841
7.620	0.978
8.890	0.582
10.160	0.416
11.430	0.229
12.065	0.127
12.700	0.020 max.

Table A5. Coordinates for NACA 4312 Airfoil Section

x(cm)	y upper(cm)	y lower(cm)
0.206	0.437	0.213
0.414	0.599	0.290
0.826	0.843	0.361
1.240	1.029	0.386
1.651	1.176	0.394
2.476	1.397	0.381
3.302	1.544	0.358
4.128	1.623	0.343
4.953	1.651	0.330
6.604	1.610	0.310
8.255	1.483	0.267
9.906	1.298	0.211
11.557	1.057	0.157
13.208	0.764	0.107
14.859	0.419	0.064
15.684	0.229	0.041
16.510	0.020 max.	0.020 max.

Table A6. Inlet Hub Streamline Pressure Tap Coordinates

Tap Number	r(cm)	α (deg)
11	20.32	0.0
12	29.21	0.0
13	41.91	0.0
14	49.21	0.0
15	76.84	0.0
21	20.32	104.0
22	29.21	104.0
23	41.91	104.0
24	49.21	104.0
25	76.84	104.0

Table A7. Inlet Tip Streamline Pressure Tap Coordinates

Tap Number	r(cm)	α (deg)
11	20.32	0.0
12	29.21	0.0
13	41.91	0.0
14	49.21	0.0
15	76.84	0.0
21	20.32	104.0
22	29.21	104.0
23	41.91	104.0
24	49.21	104.0
25	76.84	104.0

Table A8. Diffuser Hub Streamline Pressure Tap Coordinates

Tap Number	r(cm)	α (deg)
11	43.82	0.0
12	53.34	21.4
13	60.81	30.0
14	63.80	32.1
15	66.98	34.2
16	70.48	36.4
21	43.82	90.0
22	53.34	90.0
23	60.81	98.6
24	63.80	100.7
25	66.98	102.9
26	70.48	105.0
31	43.82	180.0
32	53.34	158.6
33	60.81	167.1
34	63.80	169.2
35	66.98	171.4
36	70.48	173.6
41	43.82	270.0
42	53.34	244.3
43	60.81	252.9
44	63.80	255.0
45	66.98	257.1
46	70.48	259.3
52	53.34	255.0
53	60.81	261.4
54	63.80	265.7
55	66.98	267.9
56	70.48	270.0
62	53.34	265.7
63	60.81	270.0
64	63.80	276.4
65	66.98	278.6
66	70.48	280.7

Table A9. Diffuser Tip Streamline Pressure Tap Coordinates

Tap Number	r(cm)	α (deg)
11	43.82	0.0
12	53.34	21.4
13	60.81	30.0
14	63.80	32.1
15	66.98	34.2
16	70.48	36.4
21	43.82	90.0
22	53.34	90.0
23	60.81	98.6
31	43.82	180.0
32	53.34	158.6
33	60.81	167.1
34	63.80	169.2
35	66.98	171.4
36	70.48	173.6
41	43.82	270.0
42	53.34	244.3
43	60.81	252.9
44	63.80	255.0
52	53.34	255.0
53	60.81	261.4
54	63.80	265.7
62	53.34	265.7
63	60.81	270.0

Table A10. Impeller Pressure Tap Coordinates

Streamline and Normal	P or S Surface	Coordinates	
		r(cm)	x(cm)
Hub,1	P	17.234	7.582
Hub,2	P	19.558	15.215
Hub,3	P	23.457	21.679
Hub,4	P	29.248	26.035
Hub,5	P	34.519	28.753
Hub,1	S	17.158	6.960
Hub,2	S	19.228	15.088
Hub,3	S	22.974	21.793
Hub,4	S	28.372	26.340
Hub,5	S	33.592	29.515
Mean,1	P	21.095	7.353
Mean,2	P	21.996	13.640
Mean,3	P	26.213	19.215
Mean,4	P	30.582	23.787
Mean,5	P	35.331	26.512
Mean,1	S	20.955	7.023
Mean,2	S	22.123	13.411
Mean,3	S	25.286	19.291
Mean,4	S	29.858	24.206
Mean,5	S	34.595	27.140
Tip,1	P	23.432	6.909
Tip,2	P	24.587	12.700
Tip,3	P	27.635	17.475
Tip,4	P	31.801	21.920
Tip,5	P	36.170	24.689
Tip,1	S	23.780	6.769
Tip,2	S	24.663	12.687
Tip,3	S	27.254	17.729
Tip,4	S	31.674	22.047
Tip,5	S	35.649	25.324

Table A11. Diffuser Vane Pressure Tap Coordinates

P or S Surface	Streamline			y(cm)
	Hub	Mean	Tip	
	x(cm)	x(cm)	x(cm)	
S	1.12	2.64	4.17	16.51
S	1.12	2.64	4.17	16.13
S	1.12	2.64	4.17	15.24
S	1.12	2.64	4.17	13.72
S	1.12	2.64	4.17	11.81
S	1.12	2.64	4.17	9.92
S	1.12	2.64	4.17	8.00
S	1.12	2.64	4.17	6.10
S	1.12	2.64	4.17	4.19
S	1.12	2.64	4.17	2.29
P	1.12	2.64	4.17	3.05
P	1.12	2.64	4.17	6.86
P	1.12	2.64	4.17	10.67
P	1.12	2.64	4.17	14.48
P	1.12	2.64	4.17	16.00

Actual Values +/- 0.15 cm

Appendix B Research Compressor Incidence Angles

The impeller blade and diffuser vane relative incidence angles as well as the relative and absolute flow angles leaving the impeller are given in this appendix. As discussed previously, the flow angles upstream and downstream of the impeller and downstream of the exit diffuser were measured.

The absolute flow angle entering the impeller was only measured at the mean radial location. It was noted in Chapter 5 that this angle was not dependent on flow rate. Since the impeller inlet radius is not constant, it is expected that the flow angle at the impeller face is not constant as the radius is varied. Due to the smaller velocities at the walls of the inlet section, it was not possible to calculate the impeller inlet flow angles. Because of this, the impeller face absolute flow angle was assumed to be constant and equal to the mean flow angle. Therefore, the relative incidence angles given Tables B1 through B5 are only approximate.

The impeller exit relative and absolute flow angles and the diffuser vane relative incidence angles were calculated using the flow angle from the probe downstream of the impeller. As noted in Chapter 5, the flow angle leaving the impeller is not constant across the flow channel due to the variation in impeller exit radius. As in the case of the impeller inlet, the flow angle was only measured at the mean location across the flow channel. Therefore, the flow angle was assumed constant across the exit diffuser section. The angles given in Tables B6 through B10 are the approximate angles at the mean streamline at the impeller exit and the exit diffuser vanes.

Table B1. Impeller Inlet Incidence Angles ($\alpha_{igv} = -15^\circ$)

ϕ	hub angle (deg)	mean angle (deg)	tip angle (deg)
0.120	22.5	26.0	28.7
0.137	19.8	23.8	27.1
0.155	17.1	21.2	24.6
0.173	14.2	18.8	22.6
0.190	11.4	16.5	20.7
0.207	9.1	14.5	19.1
0.225	6.4	12.1	17.2
0.243	3.8	9.9	15.3
0.261	1.2	7.6	13.3
0.279	-1.3	5.5	11.6
0.296	-4.2	2.8	9.3
0.316	-6.1	1.1	7.8

Table B2. Impeller Inlet Incidence Angles ($\alpha_{igv} = 0^\circ$)

ϕ	hub angle (deg)	mean angle (deg)	tip angle (deg)
0.122	23.4	26.6	31.1
0.146	20.3	23.7	26.7
0.159	18.7	22.0	24.9
0.176	16.6	20.3	23.4
0.196	14.3	18.2	21.7
0.211	12.5	16.6	20.3
0.227	10.8	15.1	18.9
0.245	8.9	13.5	17.4
0.264	7.1	11.8	16.0
0.281	5.3	10.2	14.6
0.301	3.5	8.5	13.1
0.314	2.3	7.4	12.0
0.333	0.7	5.8	10.6

Table B3. Impeller Inlet Incidence Angles ($\alpha_{igv} = 15^\circ$)

ϕ	hub angle (deg)	mean angle (deg)	tip angle (deg)
0.124	25.4	28.3	31.3
0.141	23.7	26.3	28.2
0.159	22.0	24.5	26.8
0.177	20.3	23.0	25.5
0.195	18.9	21.8	24.4
0.213	17.5	20.5	23.2
0.231	15.9	18.9	21.9
0.246	14.8	18.0	21.0
0.266	13.4	16.7	19.8
0.284	12.2	15.6	18.8
0.300	11.1	14.6	17.8
0.321	9.8	13.3	16.7
0.335	9.1	12.5	16.0
0.353	7.8	11.4	14.9

Table B4. Impeller Inlet Incidence Angles ($\alpha_{igv} = 30^\circ$)

ϕ	hub angle (deg)	mean angle (deg)	tip angle (deg)
0.121	28.3	30.5	33.6
0.137	27.1	29.0	30.5
0.159	25.6	27.6	29.3
0.173	24.7	26.7	28.5
0.193	23.5	25.6	27.5
0.206	21.7	24.0	26.1
0.220	21.0	23.3	25.4
0.240	19.9	22.3	24.5
0.257	19.0	21.4	23.7
0.273	18.1	20.6	23.0
0.294	17.2	19.7	22.1
0.311	16.4	18.9	21.4
0.326	15.8	18.3	20.8
0.362	14.4	17.0	19.5
0.379	13.8	16.4	18.9
0.345	15.0	17.6	20.0

Table B5. Impeller Inlet Incidence Angles ($\alpha_{igv} = 45^\circ$)

ϕ	hub angle (deg)	mean angle (deg)	tip angle (deg)
0.126	29.9	31.4	32.7
0.150	28.7	30.2	31.4
0.162	28.0	29.6	30.9
0.180	27.3	28.8	30.2
0.198	26.3	27.9	29.4
0.216	25.6	27.2	28.7
0.233	25.0	26.7	28.2
0.248	24.5	26.1	27.6
0.266	23.8	25.5	27.0
0.283	23.3	25.0	26.5
0.300	22.8	24.4	26.0
0.319	22.3	24.0	25.6
0.336	21.8	23.5	25.1
0.355	21.4	23.1	24.7
0.371	20.9	22.6	24.2
0.389	20.6	22.3	23.9

Table B6. Diffuser Incidence Angles ($\alpha_{igv} = -15^\circ$)

ϕ	β_2 (deg)	α_2 (deg)	Diffuser Incidence (deg)
0.120	78.1	75.0	18.5
0.137	76.5	72.8	15.6
0.155	74.2	71.8	14.3
0.173	71.6	70.7	12.9
0.190	64.3	72.9	15.7
0.207	61.8	71.9	14.4
0.225	60.4	70.0	12.0
0.243	58.6	68.4	10.1
0.261	57.1	66.7	8.0
0.279	56.3	64.8	5.7
0.296	55.8	62.7	3.3
0.316	55.7	59.9	0.0

Table B7. Diffuser Incidence Angles ($\alpha_{igv} = 0^\circ$)

ϕ	β_2 (deg)	α_2 (deg)	Diffuser Incidence (deg)
0.122	77.9	74.6	18.0
0.146	75.4	72.3	15.0
0.159	73.6	71.6	14.0
0.176	68.4	72.8	15.6
0.196	62.6	72.8	15.7
0.211	60.5	71.9	14.4
0.227	59.7	70.1	12.1
0.245	58.2	68.4	10.1
0.264	56.9	66.6	7.9
0.281	56.3	64.6	5.5
0.301	55.0	62.7	3.2
0.314	54.8	60.8	1.1
0.333	54.8	58.2	-1.9

Table B8. Diffuser Incidence Angles ($\alpha_{igv} = 15^\circ$)

ϕ	β_2 (deg)	α_2 (deg)	Diffuser Incidence (deg)
0.124	77.8	74.2	17.4
0.141	76.5	71.8	14.3
0.159	73.1	72.0	14.6
0.177	68.1	72.8	15.7
0.195	64.3	72.4	15.1
0.213	59.1	72.1	14.8
0.231	58.9	69.9	12.0
0.246	58.7	68.1	9.6
0.266	57.4	66.2	7.3
0.284	56.3	64.2	5.0
0.300	55.5	62.4	2.9
0.321	54.6	60.1	0.3
0.335	54.3	58.4	-1.7
0.353	53.6	56.1	-4.1

Table B9. Diffuser Incidence Angles ($\alpha_{igv} = 30^\circ$)

ϕ	β_2 (deg)	α_2 (deg)	Diffuser Incidence (deg)
0.121	78.6	73.7	16.8
0.137	76.9	72.0	14.6
0.159	73.2	71.8	14.4
0.173	68.4	73.3	16.2
0.193	65.2	72.1	14.8
0.206	63.6	71.0	13.3
0.220	58.5	71.4	13.8
0.240	57.4	69.4	11.3
0.257	57.2	67.3	8.7
0.273	56.7	65.4	6.4
0.294	56.5	62.7	3.2
0.311	56.1	60.4	0.6
0.326	55.3	58.8	-1.2
0.362	54.0	54.7	-5.6
0.379	53.5	52.7	-7.8
0.345	54.8	56.5	-3.7

Table B10. Diffuser Incidence Angles ($\alpha_{igv} = 45^\circ$)

ϕ	β_2 (deg)	α_2 (deg)	Diffuser Incidence (deg)
0.126	78.1	73.1	16.0
0.150	73.1	73.9	17.1
0.162	70.2	74.1	17.2
0.180	67.4	72.9	15.7
0.198	65.6	71.0	13.3
0.216	61.7	70.6	12.8
0.233	57.8	70.1	12.2
0.248	58.1	67.9	9.4
0.266	57.4	65.9	7.0
0.283	57.3	63.6	4.3
0.300	56.9	61.4	1.8
0.319	56.7	58.8	-1.2
0.336	56.5	56.2	-4.0
0.355	55.9	53.9	-6.5
0.371	55.6	51.3	-9.2
0.389	54.9	49.4	-11.1